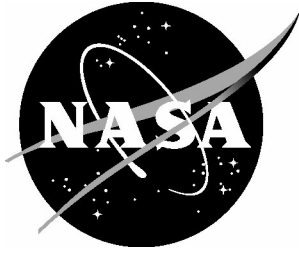NASA/TM–20205007879

# Comparison of Computational Predictions of the Mach 0.80 Transonic Truss-Braced Wing Configuration with Experimental Data

*Sally A. Viken, Craig A. Hunter, S. Naomi McMillin, and Gregory M. Gatlin*
*Langley Research Center, Hampton, Virginia*

*Daniel Maldonado, Jeffrey A. Housman, Jared C. Duensing,*
*James C. Jensen, and Cetin C. Kiris*
*Ames Research Center, Moffett Field, California*

June 2022

# NASA STI Program Report Series

Since its founding, NASA has been dedicated to the advancement of aeronautics and space science. The NASA scientific and technical information (STI) program plays a key part in helping NASA maintain this important role.

The NASA STI program operates under the auspices of the Agency Chief Information Officer. It collects, organizes, provides for archiving, and disseminates NASA's STI. The NASA STI program provides access to the NTRS Registered and its public interface, the NASA Technical Reports Server, thus providing one of the largest collections of aeronautical and space science STI in the world. Results are published in both non-NASA channels and by NASA in the NASA STI Report Series, which includes the following report types:

- TECHNICAL PUBLICATION. Reports of completed research or a major significant phase of research that present the results of NASA Programs and include extensive data or theoretical analysis. Includes compilations of significant scientific and technical data and information deemed to be of continuing reference value. NASA counterpart of peer-reviewed formal professional papers but has less stringent limitations on manuscript length and extent of graphic presentations.

- TECHNICAL MEMORANDUM. Scientific and technical findings that are preliminary or of specialized interest, e.g., quick release reports, working papers, and bibliographies that contain minimal annotation. Does not contain extensive analysis.

- CONTRACTOR REPORT. Scientific and technical findings by NASA-sponsored contractors and grantees.

- CONFERENCE PUBLICATION. Collected papers from scientific and technical conferences, symposia, seminars, or other meetings sponsored or co-sponsored by NASA.

- SPECIAL PUBLICATION. Scientific, technical, or historical information from NASA programs, projects, and missions, often concerned with subjects having substantial public interest.

- TECHNICAL TRANSLATION. English-language translations of foreign scientific and technical material pertinent to NASA's mission.

Specialized services also include organizing and publishing research results, distributing specialized research announcements and feeds, providing information desk and personal search support, and enabling data exchange services.

For more information about the NASA STI program, see the following:

- Access the NASA STI program home page at http://www.sti.nasa.gov

- Help desk contact information:

https://www.sti.nasa.gov/sti-contact-form/ and select the "General" help request type.

NASA/TM–20205007879
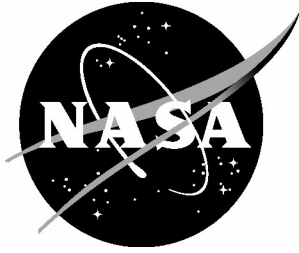
# Comparison of Computational Predictions of the Mach 0.80 Transonic Truss-Braced Wing Configuration with Experimental Data

*Sally A. Viken, Craig A. Hunter, S. Naomi McMillin, and Gregory M. Gatlin*
*Langley Research Center, Hampton, Virginia*

*Daniel Maldonado, Jeffrey A. Housman, Jared C. Duensing,*
*James C. Jensen, and Cetin C. Kiris*
*Ames Research Center, Moffett Field, California*

June 2022

## Acknowledgements

Available from:

NASA STI Program / Mail Stop 148
NASA Langley Research Center
Hampton, VA  23681-2199
Fax: 757-864-6500

## Abstract

The NASA Langley and Ames Research Centers have teamed together for comparisons of computational predictions of the Boeing Mach 0.80 Transonic Truss-Braced Wing (TTBW) configuration with a high-speed experimental dataset. The Mach 0.80 TTBW vehicle is a high wing, high aspect ratio configuration, designed for a high lift-to-drag ratio. System studies have predicted significant fuel burn and emissions benefits with the TTBW technology moving toward meeting NASA Subsonic Transport Systems-Level-Metrics. A 4.5% scale Mach 0.80 design TTBW model was recently tested at the NASA Ames Research Center 11- by 11-Foot Transonic Wind Tunnel (11-Ft TWT), providing a valuable dataset to validate computational tools and investigate best practices as risk reduction efforts continue for the development of the advanced TTBW vehicle. The NASA Computational Fluid Dynamics (CFD) team has computed free-air flow solutions on the Mach 0.80 design flight configuration and two wind tunnel configuration variants using the USM3D and LAVA flow solvers. Accurate modeling of the configuration tested in the wind tunnel environment is critical to validating the CFD tools, thus the team has included the internal cavity region and sting in their modeling of the configuration, similar to that tested in the 11-Ft TWT. Overall, the CFD simulations compared well and show similar trends as the corrected experimental data for lift and drag polars. The CFD predicted lift curve is shifted in angle of attack from what was observed in the experiment. The shift in lift also was seen in the pitching moment comparison plots. CFD solutions were computed at constant $C_L$ test point values and showed overall very good agreement when comparing constant spanwise cuts of pressure coefficient data on the wing and strut with experimental data. CFD cavity corrections were also investigated using the 11-Ft TWT cavity correction method, similar to that used to correct the wind tunnel data. Results showed some improvement in pitching moment coefficient predictions, and an increase in drag, shifting the data to the right in drag polars, further from the experimental data at lower lift conditions, good agreement near the design $C_L$, and slight improvement at the higher lift conditions.

Table of Contents

## List of Tables

# List of Figures

## Nomenclature

| | | |
|---|---|---|
| $c$ | = | mean aerodynamic chord |
| $C_D$ | = | drag coefficient |
| $C_L$ | = | lift coefficient |
| $C_m$ | = | pitching moment coefficient |
| $C_P$ | = | pressure coefficient |
| $M$ | = | Mach number |
| N | = | Number of grid cells or nodes; degrees of freedom |
| $Re$ | = | unit Reynolds number, per foot |
| $Re_c$ | = | Reynolds number based on mean aerodynamic chord |
| $X_{cp}$ | = | X-location of the center of pressure, inches |
| $X_{mrc}$ | = | X-location of the model reference center, inches |
| $y^+$ | = | dimensionless distance from the wall measured in terms of viscous lengths |

### *Symbols*

| | | |
|---|---|---|
| α | = | angle of attack, degrees |
| ß | = | angle of sideslip, degrees |
| Δ | = | difference or increment |
| η | = | y-location nondimensionalized by semispan |
| ∞ | = | freestream |

### *Acronyms*

| | | |
|---|---|---|
| AR | = | Aspect Ratio |
| ARC | = | Ames Research Center |
| CAD | = | Computer Aided Design |
| CFD | = | Computational Fluid Dynamics |
| CFL | = | Courant-Friederichs-Lewy number |
| LaRC | = | Langley Research Center |
| LAVA | = | Launch Ascent and Vehicle Aerodynamics |
| *L/D* | = | Lift-to-drag ratio |
| mrc | = | model reference center |
| OML | = | Outer Mold Line |
| MDM | = | Model Deformation Measurement |
| RANS | = | Reynolds-averaged Navier-Stokes |
| SA | = | Spalart-Allmaras one equation turbulence model |
| SA-QCR | = | SA turbulence model with the mean stress-strain Quadratic Constitutive Relationship (SA-QCR2000) |
| SA-RC-QCR | = | SA turbulence model with the Rotation/Curvature Correction and Quadratic Constitutive Relationship (SARC-QCR2000) |
| SST | = | Menter Shear-Stress Transport two equation turbulence model |
| SST-QCR | = | SST turbulence model with Quadratic Constitutive Relationship |
| SUGAR | = | Subsonic Ultra-Green Aircraft Research |
| TTBW | = | Transonic Truss-Braced Wing |
| TWT | = | Transonic Wind Tunnel |
| USM3D | = | Unstructured Mesh 3D RANS solver |
| WBSV | = | Wing and Wing Fairing/Fuselage Body & Sponson/Wing Supporting Strut/Vertical Tail |
| WBSNFV | = | Wing and Wing Fairing/Fuselage Body & Sponson/Wing Supporting Strut/Nacelle & Pylon/Flap Hinge Fairings/Vertical Tail |
| WBSNFVJ | = | Wing and Wing Fairing/Fuselage Body & Sponson/Wing Supporting Strut/Nacelle & Pylon/Flap Hinge Fairings/Vertical Tail/Jury |
| WT | = | Wind Tunnel |

# I.  Introduction

In 2008, the NASA/Boeing Subsonic Ultra-Green Aircraft Research (SUGAR) effort was initiated with industry and academia partners, for the selection of advanced commercial subsonic transport concepts and technologies for detailed studies to meet NASA defined systems-level metrics and goals for 2030-35 entry into service.  NASA has defined the subsonic transport system-level metrics (measure of success) in terms of key technology benefits (reduced noise, emissions, and energy/fuel consumption) for near-, mid-, and far-term technology generations to provide an overall increase in efficiency, environmental compatibility, and economic impact. The most recent version of these metrics from 2016 is shown in Table 1.  During the SUGAR study, systems studies had identified the Transonic Truss-Braced Wing (TTBW) SUGAR High vehicle as a technology with promising fuel burn benefits [1,2] toward meeting the NASA goal of 60% fuel burn reduction compared to the 2005 best-in-class baseline single-aisle-sized commercial transport, the 737-800 vehicle (a conventional cantilever (nonstrut-braced) wing). The TTBW SUGAR High is a high wing, high aspect ratio configuration incorporating a wing truss and designed for a high lift-to-drag ratio [3]. The wing aspect ratio (AR ~ 19.55) has an approximate 100% increase compared to the baseline cantilever vehicle, with potential for providing a significant decrease in vehicle induced drag. The high wing also allows for more efficient integration of larger bypass ratio engines, thus providing additional fuel burn benefits.  An artist rendering of the TTBW concept is shown in Figure 1, courtesy of Boeing.

With this new TTBW concept, the truss interference effects are not well understood and can add uncertainty to the benefits gained. However, the uncertainty in performance estimates can be greatly reduced through detailed design using computational methods and wind tunnel testing.  The TTBW vehicle has continued to mature over the last 10+ years, with Boeing under contract with NASA.  The concept has developed through four Phases of research: Phase 1 – the conceptual design study [2]; Phase 2 – the reduction of structural wing weight uncertainty estimates through verification of aeroelastic modes and nonlinear behavior, and validation of the high-fidelity finite element model [4,5]; Phase 3 – the refinement of the high-speed design at $M_\infty = 0.745$, and performance wind tunnel test [6]; and Phase 4 – the most recently completed research phase with the new higher speed ($M_\infty = 0.80$) design, high-lift system design, and high-speed and low-speed performance tests [7-9].  A Phase V effort has recently been awarded that will include a second low-speed test and a buffet wind tunnel test.  The Transonic Truss-Braced Wing technology maturation roadmap is shown in Figure 2.  The predicted performance benefit by Boeing for the Mach 0.80 TTBW design concept shows the TTBW technology offers a 9% reduction in fuel consumption (per seat) for a 3500nm mission with full passenger payload compared to an aspect ratio 13 conventional cantilever-wing configuration of equivalent technology [7].  Confidence in performance estimates continues to increase through detailed aerodynamic and structural design, and integration work.

The focus of this paper is on the Phase IV Mach 0.80 TTBW high-speed design configuration and the data obtained from the Phase IV high-speed wind tunnel test.  NASA and Boeing completed a high-speed performance test on a 4.5% scale model of the Mach 0.80 TTBW configuration in the NASA Ames Research Center (ARC) 11- by 11-Foot Transonic Wind Tunnel (11-Ft TWT).  Comparisons between two independent NASA CFD solvers, USM3D and LAVA, at transonic conditions are being conducted on the design flight configuration and two wind tunnel model buildup configurations to validate and continue to enhance the computational prediction tools and improve best practices for this new class of configurations.  These computational studies build on previous studies conducted on the Mach 0.745 TTBW configuration [10].

# II.  Experimental Testing of the Mach 0.80 TTBW Configuration

## A.  Wind Tunnel Test and Objectives

The Mach 0.80 TTBW high-speed wind tunnel test was conducted at the NASA Ames Research Center Unitary Plan Wind tunnel (UPWT) 11- by 11-Foot Transonic Wind Tunnel (11-Ft TWT) Facility July 15 – August 2, 2019. The 11-Ft TWT is a closed-return, variable-density facility, with a fixed-geometry, ventilated test section and a flexible wall nozzle [11], that can operate from Mach 0.2 to 1.4 and unit Reynolds numbers of 0.30 to 9.6 x $10^6$/ft.

The TTBW model tested was a fullspan, 4.5% scale representation of the high-speed TTBW design configuration, which was designed for a cruise Mach number of 0.80 and Reynolds number of 14.03 x$10^6$ based on the mean aerodynamic chord (Figure 3).  The Mach 0.80 TTBW design full scale configuration and 4.5% scale wind tunnel model reference parameters are provided in Table 2.

The objectives of the wind tunnel test were to:
1.  Acquire a transonic test database to validate the aerodynamic and stability/control methods and characteristics.
    a.  Obtain component buildup

b.  Characterize drag rise
c.  Evaluate pitch and sideslip stability
d.  Investigate horizontal tail trim, downwash, and wing wake effects
2.  Quantify wing twist aeroelastics (Model Deformation Measurements)

The data acquired during the Mach 0.80 TTBW test included: force and moment, surface static pressure, model deformation, and oil flow visualization data. Data were obtained at unit Reynolds numbers ranging from 2 to 8 million per foot ($Re_c$ = 0.83 x$10^6$ to 3.31 x $10^6$) and Mach numbers ranging from 0.2 to 0.92.

The configuration had 144 static pressures along 14 wing spanwise stations and 82 static pressures along 6 strut spanwise stations, as well as 4 static pressures for each nacelle. The left wing and strut were instrumented on the lower surface, while the right wing and strut were instrumented on the upper surface, due to the small thickness of the wing and strut components.

## B.  Wind Tunnel Data Corrections

Cavity, buoyancy, and wall corrections using the Transonic Wall Interference Correction System (TWICS) were applied to the wind tunnel test data. Internal cavity axial corrections were produced using 2 pressure ports located at the sting/balance interface. Normal force corrections and pitching moment corrections were produced using the 21 sting cavity pressures (14 on the upper surface internal cavity and 7 on the lower surface internal cavity). No base corrections were applied to the test data.

## C.  Model Wing and Strut Twist Corrections

A Model Deformation Measurement (MDM) system was used during the test to measure the wing and strut deflections. Model deformation measurement data were taken with a focus on $Re_c$ = 2.17 x $10^6$, as the dynamic pressure at this chord Reynolds number was used to determine the model's aeroelastic wing and strut jig twist corrections [9]. The MDM corrections can be applied to the computational models to account for the actual model wing and strut twist during testing to more accurately predict the model performance in the wind tunnel environment. However, the results presented in this paper do not include the model twist corrections.

# III.  Computational Flow Solvers

## A.  USM3D

USM3D is a cell-centered, finite-volume, Reynolds-averaged Navier-Stokes (RANS) flow solver that is part of the TetrUSS (Tetrahedral Unstructured Software System) package [12-14] developed at the NASA Langley Research Center (LaRC). Two versions of USM3D were used for the flight configuration and wind tunnel configuration studies. The legacy USM3D production code [12,13] utilizes an unstructured tetrahedral mesh, and fully turbulent solutions were computed with the standard Spalart-Allmaras (SA) turbulence model [15]. A more recent version of USM3D, which can handle mixed-element grids [14], was also utilized due to its improvements to robustness and speed. This "Mixed-Element USM3D" solver uses a new solution methodology known as the Hierarchical Adaptive Nonlinear Iteration Method (HANIM). HANIM is a strong nonlinear solver that improves the robustness, efficiency, and automation of RANS solutions. HANIM makes use of a matrix-free linear solver for the exact linearization of RANS equations and a nonlinear control method for solution update. Together, these enhance the iterative scheme with a mechanism for automatic adaption of the operational pseudotime step, to increase convergence rates and overcome transitional instabilities and limit cycles. Further enhancements come from a line-implicit preconditioner that simultaneously updates a preconditioner solution at all cells of a grid line based on local grid connectivity. Mixed-Element USM3D has been parallelized in a fashion that maximizes CFD solution throughput, with careful and efficient interpartition communication. This results in excellent scalability across the full range of grid partition size and number of partitions. Mixed-Element USM3D has demonstrated reductions in time to solution by 70X on benchmark 3D RANS problems, and 5X-20X on complex real-world aerodynamics simulations. For the TTBW cases analyzed in this study, Mixed-Element USM3D demonstrated reductions in time to solution of 7X-10X compared to the legacy USM3D flow solver. Mixed-element meshes have prismatic cells in the boundary layer, tetrahedral cells in the outer grid, and pyramidal cells in the transition between the two regions. Fully turbulent solutions were computed with the SA negative turbulence model [16] and the Spalart-Allmaras negative turbulence model with the mean stress-strain Quadratic Constitutive Relationship (SA-QCR2000) [17]. The SA-QCR2000 model will be referred to as SA-QCR in this paper.

**B. LAVA**

The Launch Ascent and Vehicle Aerodynamics (LAVA) framework [18] contains CFD flow solvers developed with the intent of simulating complex geometry and flowfields, using the flexible meshing options. The framework supports Cartesian, structured overset, and unstructured arbitrary polyhedral mesh paradigms. In this study, the structured overset grid methodology is applied, in which overlapping, body-fitted meshes are constructed on the geometry to serve as the computational domain.

The compressible RANS equations are solved using a finite-difference formulation applied to the nonorthogonal curvilinear transformed system of equations in strong conservation law form [19]. The Spalart-Allmaras [15] turbulence model with Rotation/Curvature Correction (RC) [20] and Quadratic Constitutive Relationship (QCR2000) [17] is used to close the Reynolds-averaged system and will be referred to as SA-RC-QCR in this paper. A second-order accurate convective flux discretization is used in the TTBW analysis. A modified Roe scheme [21,22] with third-order left/right state reconstruction, Koren limiter, and upwind/central blending are used to reduce the amount of artificial dissipation inherent in the upwind scheme.

The discrete nonlinear system of equations is embedded in a psuedotime process and marched to a steady-state. The nonlinear system of equations is linearized at each pseudotime step and an alternating line-Jacobi relaxation procedure is applied. Local pseudotime stepping is used to accelerate convergence with a pseudotime CFL = 50. Domain decomposition and the Message Passing Interface (MPI) are used to enable a scalable parallel algorithm.

## IV.  TTBW Geometry Variants Investigated

Computational simulations were conducted on the design flight configuration and two wind tunnel configurations. For these simulations, the horizontal tail was not included, as trim conditions were not known. The two wind tunnel (WT) configurations investigated are: (1) wing and wing fairing, fuselage body and sponson, wing supporting strut, and vertical tail, referenced as WBSV; and (2) wing and wing fairing, fuselage body and sponson, wing supporting strut, nacelle and pylon, flap hinge fairings, and vertical tail, referenced as WBSNFV. The difference between the flight configuration and the wind tunnel configurations analyzed were: (1) a modification of the aft portion of the fuselage and vertical tail that allowed the mounting of the test article to the support system (sting with 5° primary adapter to model roll mechanism), and (2) the jury strut, which was only included in the flight configuration simulations, as this component was not included during the testing of the 4.5% scale model in the 11-Ft TWT. The flight configuration was referred to as WBSNFVJ, which included the jury strut. All other vehicle external components were identical between the flight and wind tunnel configurations. The wind tunnel configuration simulations did also model the internal cavity region and sting, similar to that tested in the 11-Ft TWT. The wind tunnel data are being used to validate the computational predictions and tools, therefore, providing more confidence in the computational flight configuration predictions as risk reduction efforts continue for the development of the advanced TTBW vehicle. CAD representation of the TTBW design flight configuration, along with the three configurations [flight WBSNFVJ, WT WBSV, and WT WBSNFV] computationally investigated are presented in Figure 4. Front and aft oblique views of the flight WBSNFVJ configuration and the WT WBSNFV configuration are presented in Figures 5 and 6, respectively (USM3D semispan grids).

## V.  Flow Conditions Investigated

For the flight vehicle configuration simulations, all solutions were computed at an altitude of 40,000 feet with a freestream Mach number of 0.80, Reynolds number of 14.03 x $10^6$ based on the mean aerodynamic chord, angle-of-attack range of -2° ≤ α ≤ 4°, and β = 0°. Boeing's cruise design $C_L$ for the Mach 0.80 TTBW flight vehicle is 0.695. For the wind tunnel configuration simulations, all solutions were computed with a freestream Mach number of 0.80, $Re_c$ = 2.17 x $10^6$ and $Re_c$ = 3.31 x $10^6$, with an angle-of-attack range of -2° ≤ α < 5°, and β = 0°. Table 3 shows a summary of the configurations computationally investigated with test conditions. However, for the pretest CFD grid sensitivity studies that will be discussed in Section VI on the WT WBSNFV configuration, the static temperature specified was 500 °R.

Only free-air simulations are presented in this paper to validate with the corrected experimental data. Both free-air and tunnel installation effects were investigated on the Mach 0.745 TTBW wind tunnel configurations [10], where free-air simulations were determined to be a better option in terms of CFD efficiency (less computational resources and fairly accurate when compared with corrected experimental data).

# VI.  Grid Generation and Studies

## A.  LaRC Grid Generation and Studies

For the Mach 0.80 TTBW flight and wind tunnel model configurations, tetrahedral and mixed-element grid generation were conducted with HeldenMesh [23] using the IGES CAD definition of the Mach 0.80 TTBW configuration.  Boundary layers were resolved using approximately 32 layers growing at an expansion rate (layer to layer height growth in the wall normal direction) of 12-15%, with first layer heights of $y^+ = 2.0$ for the tetrahedral meshes and $y^+ = 1.0$ for the mixed-element meshes. This resulted in a first cell centroid at approximately $y^+ = 0.5$ for the tetrahedral and mixed-element meshes.  To adequately model the boundary layer flow, $y^+$ solution values of 1 or less are recommended.  The grids were semispan, since all calculations were computed at $0°$ angle of sideslip.  In all cases, the computational domain extended roughly 10 body lengths (including the tunnel support sting for the WT cases) from the modeled geometry in all directions.

The outer boundaries of the computational domain were treated as characteristic inflow/outflow surfaces with freestream conditions specified by Mach number, Reynolds number, flow angle, and static temperature. A reflection boundary condition was used at the symmetry plane of the semispan geometry. All other aircraft and model support system surfaces were treated as no-slip viscous boundaries.

Prior to finalizing grid specifications, grid sensitivity studies of lift, drag, and pitching moment were conducted on a flight vehicle configuration variant, WBSNFV (not presented in this report), and the wind tunnel WBSNFV configuration.  Mesh refinement and coarsening were performed with HeldenMesh, to scale all the grid sources by 0.5 (XFINE), 0.7 (FINE), 1.0 (MEDIUM), and 2.0 (COARSE) resulting in global surface and volume mesh scaling required to generate the xfine, fine, medium, and coarse meshes, however, the $y^+$ values at the first node off the surface did not change for mesh levels.   The boundary layer spacing was not changed, as the $y^+$ values were similar for all four meshes.  Results from the wind tunnel configuration grid study for WBSNFV at $M_\infty = 0.80$, $Re_c = $ 3.31 x $10^6$, and $\alpha = 2.0°$, with the tetrahedral and mixed-element grids, are shown in Figure 7, where the longitudinal force and moment coefficients are plotted against the square of representative grid spacing ($N^{(-2/3)}$, where N is the total number of cells) with data points approximated by a linear fit.  The $C_L$ and $C_m$ show a very mild slope toward asymptotic convergence with respect to grid spacing for the coarse, medium, fine, and xfine meshes, while the $C_D$ shows a steeper slope toward asymptotic convergence. Computational data for the grid study are also provided in Tables 4, 5, and 6 for the tetrahedral grids (SA model) and mixed-element grids (SA and SA-QCR models), respectively.  Contour plots (without scales) of the surface $C_P$ and $\Delta C_P$ (using Tecplot 360™ [24] inverse-distance interpolation) were also analyzed to assess differences between the grid levels, with the mixed-element grids using the SA-QCR model shown in Figure 8.  Very subtle differences are seen between the surface $C_P$ contour plots (Figure 8a) between grid levels.  However, the $\Delta C_P$ contour plots between grid levels (Figure 8b) highlight mild changes in shock location on the wing and strut at the transonic conditions.  Also, some mild differences in $\Delta C_P$ can be seen near the nose of the fuselage, the nacelle, and trailing edge of the wing between grid levels.  For the flight and wind tunnel model configurations, the medium grid levels were selected for use in the remaining studies, as they should be a sufficiently fine representation of the system.

For the USM3D production code using the tetrahedral grids, all solutions typically decreased ~ 5 orders of magnitude for mean solution residual.  For the USM3D mixed-element code, all solutions typically decreased 4.5 or more orders of magnitude for the mean flow and turbulence model residual.  Table 7 shows the USM3D medium level grid sizes (tetrahedral and mixed-element) for the configurations investigated.

## B.  LAVA Grid Generation and Studies

Resuming the analysis completed for the Mach 0.745 configuration [10] of the TTBW, the LAVA group generated structured overset meshes for the Mach 0.80 TTBW.  The CAD representation of the geometry was decomposed into patches using ANSA® software [25]. This served to clean up the portions of the geometry that would cause issues or difficulties when generating the structured mesh. This also facilitated separating the mesh into components and generating the surfaces that would later be used to blank portions of the overset grid on which the RANS equations would not be solved. The surfaces were further decomposed in Pointwise® [26] where quad patches with sufficient overlap for a coarse mesh were generated. The surface meshes were then grown to volumes using a hyperbolic extrusion method available within Chimera Grid Tools [27]. The growth of the surface grids was controlled using the initial wall spacing, the growth ratio, and max spacing. In this case, the initial and coarsest grid level has a $y^+$ of 1.0 and a max growth ratio of 1.25. As the grid is refined consistently, the $y^+$ scales inversely proportional to the refinement level. The refinement factor is a measure of the percentage increase in vertices per dimension. The starting grid is at

a refinement factor of 1, while refinement factors of 1.5 and 2.0 will increase the vertices on each edge by 50% and 100%, respectively.

$$Refinement\ Factor = 1 + \frac{\%\ Increase\ in\ Vertices\ per\ Dimension}{100}$$

The necessary spacing to achieve a desired $y^+$ is calculated for the coarsest grid based on the flow condition. Afterward this spacing is divided by the refinement factor. The growth rate values have an inverse exponential relationship with refinement factor.

$$Growth\ Rate = 1.25^{\frac{1}{Refinement\ Factor}}$$

To determine the appropriate grid resolution to use for validation cases, a grid refinement study was performed at wind tunnel test conditions, $M_\infty = 0.80$ and $Re_c = 3.31 \times 10^6$. The mesh was generated with refinement factors of 1.4 (medium), 1.8 (fine), and 2.0 (extra fine). The meshes can be seen in Figure 9. Table 8 lists the $y^+$ values at the first node height off the surface, growth rates, vertex counts, and number of cores used during computation for each grid level. The grid with refinement factor of 1 was found to be too coarse during the flight configuration grid refinement study (not shown in the paper) and was not used for the wind tunnel configuration studies.

The study was done using two different angles of attack ($\alpha = 0.695°$ and $2.0°$) to gain some insight on the sensitivity to angle of attack. The longitudinal force and moment coefficients were plotted against the square of representative grid spacing computed from the number of vertices or degrees of freedom (N). The plots for $\alpha = 2.0°$ can be seen in Figure 10. The solution is said to be asymptotically converging if the data points can be well approximated by a linear fit. All of the data appear to be converging with a slight deviation in the $C_L$ for this higher angle of attack. The method used for determining whether a grid is sufficiently resolved involves checking that the drag for said grid is within 10 drag counts of the asymptotic value. For both angles of attack, the fine grid met this criterion, while all refinement level results demonstrated asymptotic convergence. Computational data for the grid refinement study are provided in Table 9.

Contour plots of surface $C_P$ and $\Delta C_P$ (using a tri-linear interpolation tool) shown in Figure 11 were also analyzed to assess differences between grid levels. In Figure 11a, the fine and extra fine grids are nearly indistinguishable aside from a few regions, reaffirming the conclusion that the fine grid is sufficient. Meanwhile, the medium grid appears to lack some resolution as there are noticeable differences in $C_P$ distribution when compared to the other grid levels. The $\Delta C_P$ contour plots between grid levels highlight the mild changes in shock location, as presented in Figure 11b.

Additionally, a component buildup was run on the wind-tunnel configurations (not shown). This started with the fuselage body, sponson, and sting and increased in complexity with the most complex model also including the wing, strut, nacelle/pylon, and flap hinge fairings. As different components were added to the model, a grid refinement study would be run. This tested the asymptotic convergence of each component as well as determining which component would result in a residual reduction. It was found that once the strut was included, the flow residual reduction dropped from 6 to 5 orders, and the turbulence residual reduction dropped from 7 to 6.5 orders.

## VII. Comparison of Computational Predictions

### A. Computational Predictions on the Flight Configuration

Computational simulations of the Mach 0.80 flight configuration, WBSNFVJ, (see Figures 4 and 5) were conducted with the NASA USM3D and LAVA flow solvers at flight design conditions, $M_\infty = 0.80$, $Re_c = 14.03 \times 10^6$, $-2° \le \alpha \le 4°$, and $\beta = 0°$, to compare the computational methods. As noted earlier, Boeing's cruise design $C_L$ for the Mach 0.80 TTBW flight vehicle is 0.695. Computational results presented in Figure 12 are from the USM3D production code (tetrahedral grid) with SA turbulence model, the USM3D mixed-element code with the SA-QCR turbulence model, and the LAVA code with the SA-RC-QCR turbulence model. Similar trends are seen for lift, drag polar and lift-to-drag ratio between the NASA USM3D and LAVA codes, with the USM3D production code solutions (tetrahedral grid) showing slightly higher lift. Also, at the higher angles of attack, $\alpha > 2.0°$, differences between USM3D and LAVA become apparent. Noticeable differences in the pitching-moment characteristics are seen with all three flow solutions.

## B. Computational Predictions on the Wind Tunnel Configurations with Experimental Data

### 1. Experimental Data Repeatability

During the Mach 0.80 high-speed wind tunnel test, repeat run series of configurations and test conditions were conducted to confirm data repeatability. Experimental data run-to-run repeatability plots of $C_L$, $C_D$, and $C_m$ vs. $\alpha$, and drag polars are provided in the following figures: Figure 13 - WT WBSV configuration at $M_\infty = 0.80$, $Re_c = 2.17$ x $10^6$ ($Re = 5.25$ x $10^6$/ft) and $Re_c = 3.31$ x $10^6$ ($Re = 8.00$ x $10^6$/ft), $-2.0° \leq \alpha < 5°$, and $\beta = 0°$; Figure 14 - WT WBSNFV configuration at $M_\infty = 0.80$, $Re_c = 2.17$ x $10^6$ ($Re = 5.25$ x $10^6$/ft), $-2.0° \leq \alpha < 5°$, and $\beta = 0°$; and Figure 15 - WT WBSNFV configuration at $M_\infty = 0.80$, $Re_c = 3.31$ x $10^6$ ($Re = 8.00$ x $10^6$/ft), $-2.0° < \alpha < 5°$, and $\beta = 0°$. Trip dots were applied to the wind tunnel model to force boundary layer transition and provide for improved data repeatability [9]. For the wind tunnel data presented in this paper, the trip dot height used for the forward trip location on the wing and strut was closer to the minimum required for $Re_c = 2.17$ x $10^6$ [9]. The data repeatability for lift and drag are quite good for both configurations at these two chord Reynolds number conditions investigated with some variation in data repeatability observed for the pitching moment. The experimental runs shown in Table 10 were selected for the CFD investigations.

### 2. Comparison of Computational Predictions and Experimental Data

Computational results from the NASA USM3D and LAVA flow solvers are compared with fully corrected experimental data (corrections include cavity, buoyancy, and tunnel walls). For the USM3D mixed-element code solutions, SA and SA-QCR turbulence model data are provided. For the USM3D production code solutions with tetrahedral meshes, the SA turbulence model data are provided only for the $Re_c = 3.31$ x $10^6$ cases investigated. All LAVA solutions utilize the SA-RC-QCR turbulence model. When comparing CFD simulations of the wind tunnel configurations with the corrected wind tunnel data, only the TTBW model outer mold line (OML) surfaces are used in the force and moment integration, unless otherwise noted. No trip dot drag was accounted for in the NASA CFD data presented, however, Boeing's internal method estimates the trip dots to create ~ 8 counts of drag at the design Mach of 0.80, based on trip dot height, number of dots, and local pressure where dots were applied [9].

Computational predictions with the corrected experimental data are presented in Figures 16 through 19 for $C_L$ vs. $\alpha$, $C_L$ vs. $C_D$, $L/D$ vs. $\alpha$, $L/D$ vs. $C_L$, $C_m$ vs. $C_L$, and $(X_{cp} - X_{mrc})/c$ vs. $\alpha$. The X-location for the center of pressure, $X_{cp}$, is determined by

$$X_{cp} = X_{mrc} + C_{m,mrc}/C_L * c$$

where $X_{mrc}$, the X-location for the model reference center, is at 37.03 inches, model scale. The nose of the fuselage is located at 5.85 inches, model scale. The aerodynamic force of the model acts through the center of pressure, and $(X_{cp} - X_{mrc})$ represents the X-distance that the center of pressure is from the model reference center. As $C_L$ approaches 0, the $X_{cp}$ calculation can grow to very large values. Therefore, for the $(X_{cp} - X_{mrc})/c$ vs. $\alpha$ plots presented, data are not shown for $|C_L| < 0.10$.

In Figure 16, which is the WT WBSV configuration at $M_\infty = 0.80$, $Re_c = 2.17$ x $10^6$, $-2° \leq \alpha < 5°$, and $\beta = 0°$, there is an angle-of-attack shift in the computational $C_L$ values compared to the experimental data, with more variation at the higher angles of attack above $\alpha = 2.3°$. The shift in angle of attack is ~ $0.2°$ at the lowest $C_L$ and ~ $0.3°$ near the design $C_L$ of 0.695. The USM3D mixed-element code drag polars with SA and SA-QCR turbulence models overall compare well for $C_L$ values < 0.84, with a slight increase in drag seen with the LAVA solver near the $C_{Dmin}$ region. The USM3D drag polars compare well with experimental data for $C_L$ below 0.66, again with a slight increase in drag seen with the LAVA solver near the $C_{Dmin}$ region. The drag polars show more variation between the codes and the experimental data at the higher lift values. The experimental drag polar appears to have a slight rotation compared to the CFD polars. Boeing did compare the final twist of the model in the tunnel compared to the 1G design twist distribution at the design Mach and lift coefficient, with the final 'as tested' shape matching the 1G design very well [9]. For off-design conditions, such as at higher angles of attack where there is more loading on the wing, the model wingtip region tends to washout, resulting in a less elliptic spanloading and net increase in drag for a given lift coefficient as compared to the CFD [9]. The lift-to-drag ratio exhibits the same characteristics as mentioned above for the lift, i.e., below $2.3°$ angle of attack, the CFD values are higher than the experimental values and above $2.3°$, all the curves collapse. When the lift-to-drag ratio is plotted versus the lift coefficient, the curves collapse in the linear lift region ($C_L < 0.66$). At higher lift conditions, the CFD values don't match as well between code results and are higher than the experimental values. CFD predicts more nose-down pitching moment than was measured in the wind

tunnel test.  However, the CFD predictions for $(X_{cp} - X_{mrc})/c$ compare well with the experimental data.

For the WT WBSV configuration at $M_\infty = 0.80$, $Re_c = 3.31 \times 10^6$, $-2° \le \alpha < 5°$, and $\beta = 0°$, presented in Figure 17, similar trends are seen between the CFD predictions and the experimental data, but they are more pronounced at this higher chord Reynolds number condition.  The shift in angle of attack is $\sim 0.3°$ at the lowest $C_L$ and $\sim 0.5°$ near the design $C_L$ of 0.695.  The USM3D mixed-element code drag polars with SA and SA-QCR turbulence models and the LAVA simulations overall compare well for $C_L$ values $\le 0.88$, with a slight variation at $C_{Dmin}$.  A slight decrease in drag is seen with the USM3D production code (tetrahedral grid) as compared to the other CFD simulations.  The USM3D mixed-element code and LAVA drag polars overall compare well with experimental data for $C_L$ below 0.66.  At the higher $C_L$ values, the drag polars show more variation between the codes and the experimental data.  The predicted $L/D$ values are higher than the experimental values up to $\alpha \sim 2.0°$.  At $\alpha > 2.5°$, past experimental $L/D_{max}$, the experimental values are slightly higher than the CFD code predictions.  For $L/D$ vs. $C_L$, the USM3D mixed-element and LAVA code $L/D$ predictions compare well with experimental data for $C_L < 0.66$.  At the higher $C_L$ values, past experimental $L/D_{max}$, all CFD code $L/D$ predictions are higher than the experimental values.  As was seen in Figure 16, the CFD codes all predict more nose-down pitching moment than was measured experimentally.  At this higher chord Reynolds number condition, a little more variance is seen with the CFD predictions for $(X_{cp} - X_{mrc})/c$ compared with the experimental data.

In Figure 18 for the WT WBSNFV configuration at $M_\infty = 0.80$, $Re_c = 2.17 \times 10^6$, $-2° \le \alpha < 5°$, and $\beta = 0°$, there is an angle-of-attack shift in the CFD $C_L$ values compared to the experimental data with more variation at the higher angles of attack above $\alpha = 2.0°$.  The shift in angle of attack is $\sim 0.2°$ near the lowest $C_L$ and $\sim 0.3°$ near the design $C_L$ of 0.695.  The USM3D mixed-element code with the SA and SA-QCR turbulence models and the LAVA code drag polars overall compare well for $C_L$ values $< 0.86$, with slightly more drag seen with the USM3D mixed-element code (SA model) near the $C_{Dmin}$ region.  The USM3D mixed-element code with SA-QCR turbulence model, the LAVA code, and the experimental data drag polars compare well for $C_L$ between 0.26 and 0.72.  The drag polars were observed to have more variation between the codes and the experimental data at the lower and higher $C_L$ value regions.  The CFD codes predict higher $L/D$ values than the experimental data up to $\alpha \sim 2.2°$.  At the higher angles of attack past experimental $L/D_{max}$, the CFD predictions compare well with the experimental data.  The CFD predicted $L/D$ values compare well with experimental data for $C_L < 0.70$.  At the higher $C_L$ values, past experimental $L/D_{max}$, the CFD code $L/D$ predictions are higher than the experimental values.  None of the CFD predictions for $C_m$ compare well with the experimental data, with more nose-down (negative) pitching moment coefficient predicted by the codes for $C_L > 0$.  However, the CFD predictions for $(X_{cp} - X_{mrc})/c$ compare well with the experimental data.  As presented in Ref. [9], Boeing CFD OVERFLOW results with the SA-RC-QCR model (with corrections for trip dot drag, installation effects, and cavity corrections) for the same configuration and test conditions showed a fairly similar angle-of-attack shift in their CFD $C_L$ values compared to the experimental data (corrected for sting cavity effects only), with a shift in $\alpha$ of $\sim 0.2°$.  Boeing also investigated using the Menter Shear-Stress Transport turbulence model with Quadratic Constitutive Relation (SST-QCR), in which their CFD $C_L$ - $\alpha$ curves, and $C_m$ compared well with the experimental data (not shown) [9].  For the drag polar, the Boeing data show some differences between the two turbulence models, which bracket the experimental data, with the SA-RC-QCR model results in better agreement at the lower lift coefficients (particularly near design $C_L = 0.695$), and the SST-QCR model results in better agreement at the higher lift coefficients (not shown) [9].  The SST model is currently implemented in the USM3D production code, however, not in the mixed-element USM3D code or the LAVA code.  Thus, NASA results with the SST model are not presented in this paper.

For the WT WBSNFV configuration at $M_\infty = 0.80$, $Re_c = 3.31 \times 10^6$, $-2° \le \alpha < 5°$, and $\beta = 0°$, presented in Figure 19, there are similar trends once again, but differences between the CFD predictions and experimental data are more pronounced at this higher chord Reynolds number condition.  The shift in angle of attack is $\sim 0.3°$ near $C_L$ of 0.0 and $\sim 0.5°$ near the design $C_L$ of 0.695.  The USM3D mixed-element code with SA and SA-QCR turbulence models and the LAVA code drag polars overall compare well for $C_L$ values $< 0.86$, with slightly more drag seen with the USM3D mixed-element code (SA model) near $C_{Dmin}$.  The USM3D production code (tetrahedral grid) predicted slightly lower drag values than the other codes.  The computational and experimental drag polars compare well near a $C_L$ of 0.5 with more variation at lower and higher $C_L$ values.  For $L/D$ vs. $\alpha$, the CFD codes predict higher $L/D$ than shown with the experimental data up to $\alpha$ of $\sim 2.0°$.  At $\alpha > 2.5°$, past experimental $L/D_{max}$, the experimental $L/D$ is slightly higher than the CFD code predictions.   For $L/D$ vs. $C_L$, the USM3D mixed-element and LAVA $L/D$ predictions compare well with experimental data for $C_L \le 0.64$.  At the higher $C_L$ values, all CFD code $L/D$ predictions are higher than the

experimental $L/D$. All of the CFD predictions for $C_m$ do not compare well with the experimental data, with more negative pitching moment coefficient predicted by the codes. At this higher chord Reynolds number condition, a little more variance is seen with the CFD predictions for $(X_{cp} - X_{mrc})/c$ compared with the experimental data.

*3. Spanwise Pressure Coefficient Comparisons at Constant $C_L$*

CFD solutions were computed near three wind tunnel test point lift conditions at $M_\infty = 0.80$ and $Re_c = 2.17 \times 10^6$, for both the WT WBSV and WBSNFV configurations, to compare constant spanwise cuts of pressure coefficient data on the wing and strut with experimental data. This chord Reynolds number condition was chosen for this investigation because as stated earlier, the dynamic pressure at this chord Reynolds number was used to determine the model's aeroelastic wing and strut jig twist corrections [9].

The test point $C_L$ values at $M_\infty = 0.80$ and $Re_c = 2.17 \times 10^6$ selected to investigate were 1) low $C_L$, near $C_{Dmin}$; 2) $C_L$ near TTBW design $C_L$; and 3) high $C_L$. Table 11 shows the configurations, experimental runs, and test point $C_L$ values investigated.

Figures 20-25 present comparisons of the CFD constant spanwise cuts of pressure coefficient data with the experimental data at 7 wing spanwise stations and 3 strut spanwise stations. The experimental data for the left and right wing and strut are presented, along with the USM3D mixed-element code solutions and LAVA solutions.

For the WBSV configuration at $C_L = 0.176$ and $C_L = 0.719$, presented in Figures 20 and 21, respectively, overall very good agreement of the wing $C_P$ values is seen between the CFD predictions and experimental data for all spanwise stations. At the $\eta = 49.6\%$ station, inboard of the wing/strut intersection, a stronger shock is seen with the experimental data on the wing lower surface. However, during the model vendor quality assurance inspection of the sectional incidence variation for the wing and strut, one measured station was identified that exceeded the design tolerance for angular measurements of +/- 0.1°. The left-hand strut at $\eta = \sim 43.6\%$ span station was out of alignment by 0.198° (trailing edge down) [9]. Also, at the $\eta = 55.4\%$ station near the wing/strut intersection, some mild differences on the wing lower surface back to the start of the pressure recovery region are noted between CFD and experimental data. Very good agreement is seen for the strut spanwise station cuts, comparing CFD with experimental data. At $C_L = 0.849$ presented in Figure 22, overall good comparisons of the wing $C_P$ values are seen between the CFD predictions and experimental data for all spanwise stations. At the $\eta = 49.6\%$ station inboard of the wing/strut intersection, a stronger shock is seen with the experimental data on the wing lower surface. For stations $\eta = 37.3\%$ and $\eta = 55.4\%$, there are small differences with the wing lower surface pressure coefficients between the CFD and experimental data. Good agreement is seen for the strut spanwise station cuts, with the strength of the CFD-predicted flow acceleration being slightly lower on the strut upper surface for $\eta = 11.0\%$ and $\eta = 24.0\%$ stations.

For the WBSNFV configuration at $C_L = 0.168$, presented in Figure 23, overall good agreement of the wing $C_P$ values is seen between the CFD predictions and experimental data for the spanwise stations. For the $\eta = 24.0\%$ spanwise station, the USM3D solution with the SA model predicted a lower pressure on the wing lower surface. For the $\eta = 73.1\%$ spanwise station, CFD predicts a slightly stronger lower surface flow acceleration at the leading-edge region (pressure coefficients lower) than seen with the experimental data. Good agreement is seen for the strut spanwise stations, comparing CFD with experimental data. At $C_L = 0.707$, presented in Figure 24, a good comparison of the wing $C_P$ values is seen between the CFD predictions and experimental data overall for the spanwise stations, with some small variation on the wing lower surface for the spanwise cut stations inboard and near the wing/strut intersection, $\eta = 49.6\%$ and $\eta = 55.4\%$, respectively. The CFD predicts the wing upper surface shock location to be slightly aft of the experimental data for the $\eta = 37.3\%$ station and outboard. Good agreement is seen for the strut spanwise station cuts, with the strength of the CFD-predicted flow acceleration being slightly lower (pressure coefficients aren't as low) on the strut upper surface for the $\eta = 11.0\%$ station. At $C_L = 0.848$, presented in Figure 25, a good comparison of the wing $C_P$ values is seen between the CFD predictions and experimental data for all spanwise stations, with some mild differences on the wing lower surface for the spanwise stations inboard and near the wing/strut intersection ($\eta = 37.3\%$, $\eta = 49.6\%$, and $\eta = 55.4\%$). The CFD predicts the upper surface shock location to be slightly aft of the experimental data for the $\eta = 37.3\%$, $\eta = 55.4\%$, and $\eta = 73.1\%$ stations. Good agreement is seen for the strut spanwise stations, comparing CFD with experimental data.

*4. Cavity Corrections Investigation*

The CFD data presented thus far did not include the internal body cavity surfaces in the force and moment integration, only the external OML of the TTBW model. However, following discussions with Boeing, the NASA teams did investigate including the internal cavity surfaces and applying cavity corrections similar to that implemented on the

wind tunnel data (ARC 11-Ft TWT cavity correction method). An image of a symmetry plane cut through the TTBW wind tunnel model is provided in Figure 26 that shows an outline of the CFD model and sting with cavity region. Knowing the cavity pressure tap locations and the defined reference areas provided for each pressure tap region, the axial force, normal force, and pitching moment cavity corrections could be calculated, along with lift and drag corrections, similar to that applied to the wind tunnel data. As discussed in Section II.B., the wind tunnel model cavity axial corrections were produced using 2 pressure ports located at the sting/balance interface. Normal force corrections and pitching moment corrections were produced using the 21 sting cavity pressures (14 on the upper surface internal cavity and 7 on the lower surface internal cavity). For the CFD, a similar approach was used when calculating the normal force and pitching moment corrections. However, for the cavity axial force corrections, pressures at the midpoint of each vertical face of the cavity interior wall on the symmetry plane were used since the CFD cavity was not modeled all the way forward to the sting/balance interface.

For the test runs investigated and presented in this paper (runs 378, 413, 433, and 461) for the WT WBSV and WBSNFV configurations at $M_\infty = 0.80$, $Re_c = 2.17 \times 10^6$ and $Re_c = 3.31 \times 10^6$, $-2.0° \le \alpha < 5°$, and $\beta = 0°$, the experimental data cavity increment ranges were as follows: $0.0050 < \Delta C_n < 0.0064$; $-0.0020 < \Delta C_a < -0.0016$; and $-0.0395 < \Delta C_m < -0.0318$. The integrated force and moment cavity increments were extracted from the CFD solutions for these cases investigated and the cavity increment ranges were as follows: $0.0037 < \Delta C_n < 0.0043$; $-0.0010 < \Delta C_a < -0.0007$; and $-0.0259 < \Delta C_m < -0.0232$. When calculating the CFD cavity increments using the ARC 11-Ft TWT cavity correction method explained above, the cavity increment ranges were as follows: $0.0051 < \Delta C_n < 0.0056$; $-0.0020 < \Delta C_a < -0.0015$; and $-0.0349 < \Delta C_m < -0.0323$. Data are presented in Figures 27-30 ($\Delta C_n$ vs. $\alpha$, $\Delta C_n$ vs. $\Delta C_a$, and $\Delta C_m$ vs. $\Delta C_n$) for these cases investigated, showing the comparison of the integrated force and moment flow solution cavity increments from the CFD solutions compared to CFD cavity increments calculated using the ARC 11-Ft TWT cavity correction method (similar to that applied to the wind tunnel data), along with the experimental data cavity increments. The CFD cavity increments calculated based on the ARC 11-Ft TWT cavity correction method do provide better comparisons with the experimental data cavity increments, however, differences still exist.

In Figures 31-34, CFD data (no internal cavity surfaces in integration), corrected experimental data, and CFD including internal cavity surfaces with the 11-Ft TWT cavity correction method applied are presented. When using the 11-Ft TWT cavity correction method, the CFD predicted pitching moment values were closer to experimental values. The CFD predicted drag values increased with this method shifting the data to the right in drag polars and in general further from the experimental data at lower lift conditions, good agreement near the design $C_L$, and slight improvement at the higher lift conditions. The CFD predicted lift-to-drag ratio were reduced in magnitude due to the slight loss in lift and the increase in drag.

## VIII.  Summary

Free-air computational simulations have been conducted on the Boeing Mach 0.80 TTBW flight configuration, WBSNFVJ, at flight conditions $M_\infty = 0.80$ and $Re_c = 14.03 \times 10^6$, along with two wind tunnel model buildup configurations, WBSV and WBSNFV, at $M_\infty = 0.80$, and $Re_c = 2.17 \times 10^6$ and $Re_c = 3.31 \times 10^6$. The wind tunnel computational predictions were compared with corrected experimental data obtained from a 4.5% scale Mach 0.80 TTBW design model recently tested at the NASA Ames Research Center Unitary Plan Wind Tunnel 11- by 11-Foot Transonic Wind Tunnel.

Two versions of the USM3D flow solver (the legacy production code with SA turbulence model and the newer mixed-element code with SA and SA-QCR turbulence models) and the LAVA flow solver (with SA-RC-QCR turbulence model) were investigated for these studies. Grid convergence studies were conducted for both the flight and wind tunnel configurations, with the wind tunnel studies presented in this paper showing asymptotic convergence with respect to grid spacing.

For the flight configuration simulations, similar trends were seen for the lift curve ($C_L$ vs $\alpha$), the drag polars ($C_L$ vs $C_D$), and the lift-to-drag characteristics ($L/D$ vs $\alpha$ and $L/D$ vs $C_L$) between the NASA USM3D and LAVA codes, with the USM3D production code solutions showing slightly higher lift. Also, at the higher angles of attack, $\alpha > 2.0°$, differences between USM3D mixed-element code and LAVA become apparent. Notable differences were observed for the pitching moment characteristics ($C_m$ vs $C_L$) for all three flow solutions primarily due to small differences in the predicted normal shock location.

The wind tunnel computational simulations for USM3D mixed-element code and LAVA overall compared well with each other for $C_L$ values at $\alpha < 2.0°$, with more variation at the higher angles of attack. The USM3D production code solutions predicted slightly higher lift. The drag characteristics for the WT WBSV configuration showed that

the USM3D mixed-element solutions with SA and SA-QCR turbulence models compared well for $C_L$ values < 0.84 at $Re_c$ = 2.17 x $10^6$, and $C_L$ values ≤ 0.88 at $Re_c$ = 3.31 x $10^6$, with slightly more drag observed with the LAVA simulations near $C_{Dmin}$. For the WT WBSNFV configuration, USM3D mixed-element SA-QCR solutions and LAVA (SA-RC-QCR) solutions compared the best for $C_L$ values < 0.86, with slightly more drag seen with the USM3D mixed-element code (SA model) near $C_{Dmin}$. A slight decrease in drag is seen with the USM3D production code (tetrahedral grid) as compared to the other CFD simulations. Notable differences were observed for the pitching moment characteristics ($C_m$ vs $C_L$) for all the flow solutions primarily due to small differences in the predicted normal shock location and due to the swept cavity at the base of the model.

The CFD data showed similar trends as the corrected experimental data, however, the following were observed: 1) an angle-of-attack shift in the CFD $C_L$ values compared to the experimental data (e.g., for the WT WBSNFV configuration at $M_\infty$ = 0.80 and $Re_c$ = 2.17 x $10^6$, an angle-of-attack shift ~ 0.2° was observed near the lowest $C_L$ values investigated and ~ 0.3° near the design $C_L$ of 0.695), and 2) a large variation in pitching moment at most $C_L$ values. From Boeing OVERFLOW studies [9] for the same configuration and test conditions, an angle-of-attack shift, ~ 0.2°, was observed when using the SA-RC-QCR turbulence model. However, when Boeing implemented the SST model with QCR for this configuration and conditions, their CFD-predicted lift and pitching moment characteristics compared well with the experimental data. The SST model should also be investigated by the NASA team to see if improvements between CFD predictions and experimental data can be obtained.

CFD solutions were computed at constant $C_L$ test point values and showed overall good agreement when comparing constant spanwise cuts of pressure coefficient data on the wing and strut with experimental data. Some differences were noted in the wing/strut channel along with some slight shifting of the shock location at some of the span stations. CFD cavity corrections were also investigated using the ARC 11-Ft TWT cavity correction method, similar to that used to correct the wind tunnel data. Applying the 11-Ft TWT cavity correction method to the CFD resulted in some improvement in the pitching moment coefficient predictions and an increase in drag, shifting the data to the right in drag polars, further from the experimental data at lower lift conditions, good agreement near the design $C_L$, and slight improvement at the higher lift conditions.

The wind tunnel data have been highly valuable for computational tool validation and improving best practices for this new class of configurations, as risk reduction efforts continue for the development of the advanced TTBW vehicle. Boeing has predicted significant fuel burn and emissions benefits with the TTBW technology. The TTBW technology is potentially applicable to multiple vehicle classes: single-aisle, twin-aisle, and regional jets.

## References

[1] Droney, C., Harrison, N., Gatlin, G., "Subsonic Ultra-Green Aircraft Research: Transonic Truss-Braced Wing Technical Maturation", 31st Congress of the International Council of the Aeronautical Sciences, Belo Horizonte, Brazil, September 9-14, 2018.
[2] Bradley, M. K., and Droney, C. K., "NASA/CR-2011-216847, Subsonic Ultra Green Aircraft Research" Phase I Final Report", Boeing Research and Technology, Huntington Beach, CA, April 2011.
[3] https://www.boeing.com/features/innovation-quarterly/aug2017/feature-technical-sugar.page
[4] Bradley, M., Droney, C. and Allen, T. NASA/CR-2015-218704/Volume I, Subsonic Ultra Green Aircraft Research Phase II: Volume I - Truss Braced Wing Design Exploration", Boeing Research and Technology, Huntington Beach, CA, April 2015.
[5] Bradley, M. K., Allen, T. J., and Droney, C. K., "NASA/CR-2015-218704/Volume III, Subsonic Ultra Green Aircraft Research: Phase II – Volume III – Transonic Truss Braced Wing Aeroelastic Test", Boeing Research and Technology, Huntington Beach, CA, April 2014.
[6] Droney, C. K., Sclafani, A. J., Harrison, N. A., Grasch, A. D., Beyar, M. D., "NASA/CR-20205005698, Subsonic Ultra Green Aircraft Research: Phase III – Mach 0.75 Transonic Truss-Braced Wing Design", Boeing Research and Technology, Huntington Beach, CA, September 2020.
[7] Harrison, N. A., and Droney, C. K., "NASA/CR-20xx-xxxx, Subsonic Ultra Green Aircraft Research: Phase IV, Volume I - Mach 0.80 Transonic Truss-Braced Wing High-Speed Design", Boeing Research and Technology, Huntington Beach, CA, Publication Date TBD.
[8] Harrison, N. A., Beyar, M. D., Dickey, E. D., Hoffman, K., Gatlin, G. M., Viken, S. A., Development of an Efficient Mach=0.80 Transonic Truss-Braced Wing Aircraft, AIAA SciTech 2020 Forum, AIAA-2020-0011, Orlando, FL, January 6-10, 2020.
[9] Harrison, N. A., Sclafani, A. J., Beyar, M. D., Dickey, E. D., Intravartolo, N. M., "NASA/CR-20xx- xxxx, Subsonic Ultra Green Aircraft Research: Phase IV Final Report, Volume II - Transonic Truss-Braced Wing High-Speed Test Report", Boeing Research and Technology, Huntington Beach, CA, Publication Date TBD.

[10] Maldonado, D., Housman, J. A., Duensing, J. C., Jensen, J. C., Kiris, C. C., Viken, S. A., Hunter, C. A., Frink, N. T., McMillin, S. N.: Computational Simulations of a Mach 0.745 Transonic Truss-Braced Wing Design. AIAA SciTech 2020 Forum, AIAA-2020-1649, Orlando, FL, January 6-10, 2020.

[11] https://www.nasa.gov/centers/ames/orgs/aeronautics/windtunnels/11x11-wind-tunnel.html

[12] Frink, N. T.: "Tetrahedral Unstructured Navier-Stokes Method for Turbulent Flow," AIAA Journal, Vol. 36, No. 11, Nov. 1998, pp. 1975-1982.

[13] Frink, N. T., Pirzadeh, S. Z., Parikh, P. C., Pandya, M. J., and Bhat, M. K.: "The NASA Tetrahedral Unstructured Software System," The Aeronautical Journal, Vol. 104, No. 1040, October 2000, pp. 491-499.

[14] Pandya, M. J., Jespersen, D. C., Diskin, B., Thomas, J. L., Frink, N. T.: Accuracy, Scalability, and Efficiency of Mixed-Element USM3D for Benchmark Three-Dimensional Flows, AIAA SciTech 2019 Forum, AIAA 2019-2333, San Diego, CA, January 7-11, 2019.

[15] Spalart, P. R.; and Allmaras, S. R.: A One-Equation Turbulence Model for Aerodynamic Flows. 30th Aerospace Sciences Meeting and Exhibit, Reno, NV, 1992. AIAA-92-0439.

[16] Allmaras, S. R., Johnson, F. T., and Spalart, P. R., "Modifications and Clarifications for the Implementation of the Spalart-Allmaras Turbulence Model," ICCFD7-1902, 7th International Conference on Computational Fluid Dynamics, Big Island, Hawaii, 9-13 July 2012.

[17] Spalart, P. R.: "Strategies for Turbulence Modeling and Simulation," International Journal of Heat and Fluid Flow, Vol. 21, 2000, pp. 252-263.

[18] Kiris, C., Housman, J., Barad, M., Brehm, C., Sozer, E., and Moini-Yekta, S., "Computational Framework for Launch, Ascent, and Vehicle Aerodynamics (LAVA)," Aerospace Science and Technology, Vol. 55, 2016, pp. 189–219.

[19] Vinokur, M., "Conservation Equations of Gasdynamics in Curvilinear Coordinate Systems," Journal of Computational Physics, Vol. 14, 1974, pp. 105–125.

[20] Shur, M. L., Strelets, M. K., Travin, A. K., Spalart, P. R.: "Turbulence Modeling in Rotating and Curved Channels: Assessing the Spalart-Shur Correction," AIAA Journal Vol. 38, No. 5, 2000, pp. 784-792.

[21] Housman, J., Kiris, C., and Hafez, M., "Time-Derivative Preconditioning Methods for Multicomponent Flows - Part I: Riemann Problems," Journal of Applied Mechanics, Vol. 76, No. 2, 2009.

[22] Housman, J., Kiris, C., and Hafez, M., "Time-Derivative Preconditioning Methods for Multicomponent Flows - Part II: Two-Dimensional Applications," Journal of Applied Mechanics, Vol. 76, No. 3, 2009.

[23] Wick, A., Hooker, R., Agelastos, A., "HeldenMesh User's Manual Version 3.05", Helden Aerospace Corporation, June 2018.

[24] https://www.tecplot.com/products/tecplot-360/

[25] BETA-CAE, "ANSA Pre-processor, The Advanced CAE Pre-processing Software for Complete Model Build-up", http://www.beta-cae.com/ansa.htm, 2019.

[26] https://www.pointwise.com

[27] Chan, W., "Developments in Strategies and Software Tools for Overset Structured Grid Generation and Connectivity", 20th AIAA Computational Fluid Dynamics Conference, Honolulu, Hawaii, June 2011, AIAA-2011-3051.

**Table 1. NASA Subsonic Transport System-Level Metrics (Measures of Success) (v2016.1).**

| TECHNOLOGY BENEFITS | TECHNOLOGY GENERATIONS (Technology Readiness Level = 5-6) | | |
|---|---|---|---|
| | Near Term 2015-2025 | Mid Term 2025-2035 | Far Term beyond 2035 |
| Noise Reduction (cum below Stage 4) | 22 – 32 dB | 32 – 42 dB | 42 – 52 dB |
| LTO No$_x$ Emissions Reduction (below CAEP 6) | 70 – 75% | 80% | >80% |
| Cruise No$_x$ Emissions Reduction (rel. to 2005 best in class) | 65 – 70% | 80% | >80% |
| Fuel/Energy Consumption Reduction (rel. to 2005 best in class) | 40 – 50% | 50 – 60% | 60 – 80% |



**Figure 1. Artist rendering of the Transonic Truss-Braced Wing Concept (courtesy of Boeing).**
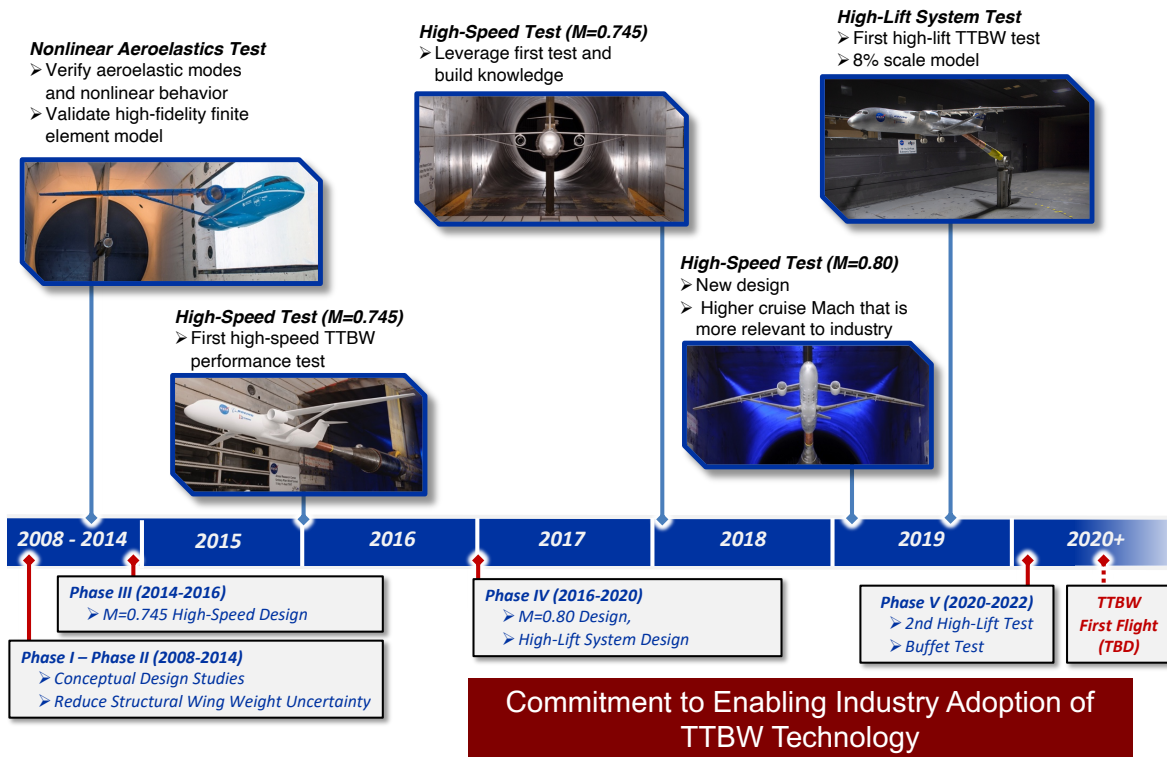


**Figure 2. Transonic Truss-Braced Wing technology maturation roadmap (original image, courtesy of Boeing, was modified and includes updates in the technology maturation).**
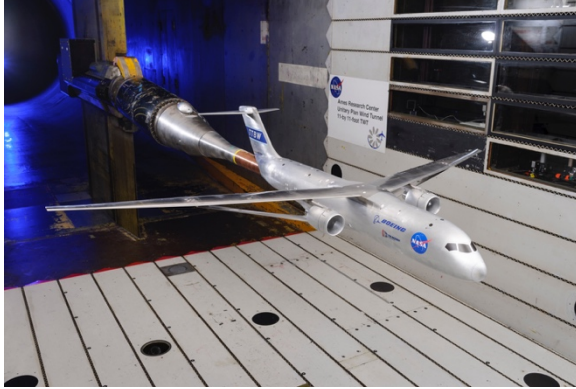
(a) Front oblique view.  (b) View from under side of model.

**Figure 3.  4.5% scale, Mach 0.80 TTBW model installed in the NASA ARC 11-Ft TWT.**

**Table 2.  Mach 0.80 TTBW design full scale configuration and 4.5% scale model reference parameters.**

| Full scale reference parameters* | | 4.5% scale model reference parameters | |
|---|---|---|---|
| Reference Area | 212,703.80 in$^2$ | Reference Area | 430.7256 in$^2$ |
| Mean Aerodynamic Chord | 110.2859 in | Mean Aerodynamic Chord | 4.963 in |
| Span Length | 2039.30 in | Span Length | 91.769 in |
| Aspect Ratio | 19.55 | Aspect Ratio | 19.55 |

*These values used when conducting CFD with the design full scale configuration.



| Flight WBSNFVJ | WT WBSV | WT WBSNFV |
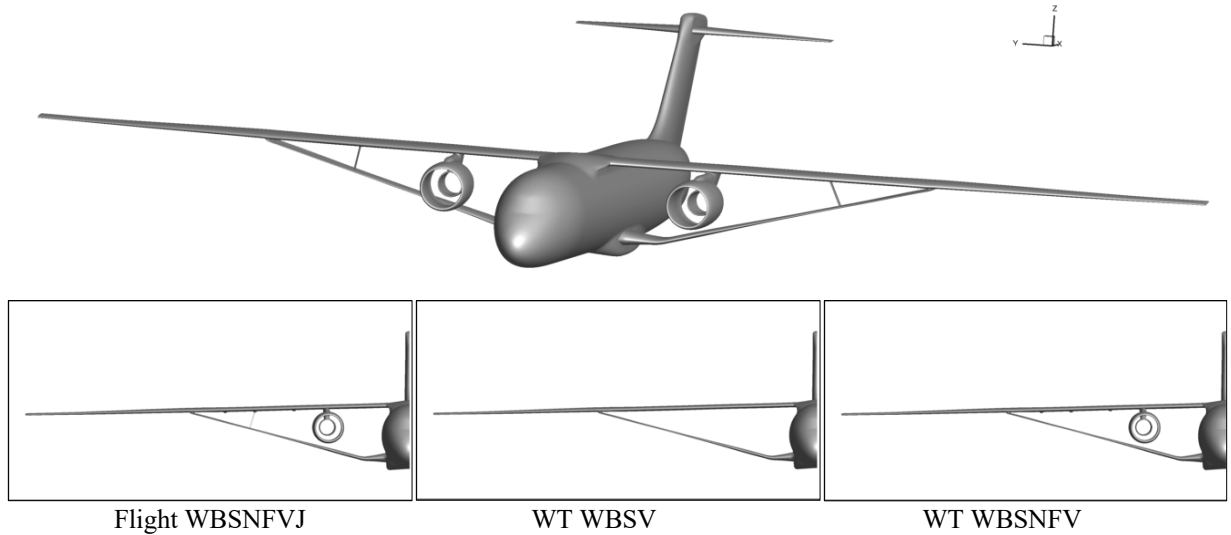
**Figure 4.  CAD representation of the TTBW design flight configuration (top) with front views of each configuration computationally investigated (horizontal tail not included in simulations).**

(a)  Front oblique view.          (b)  Aft oblique view.
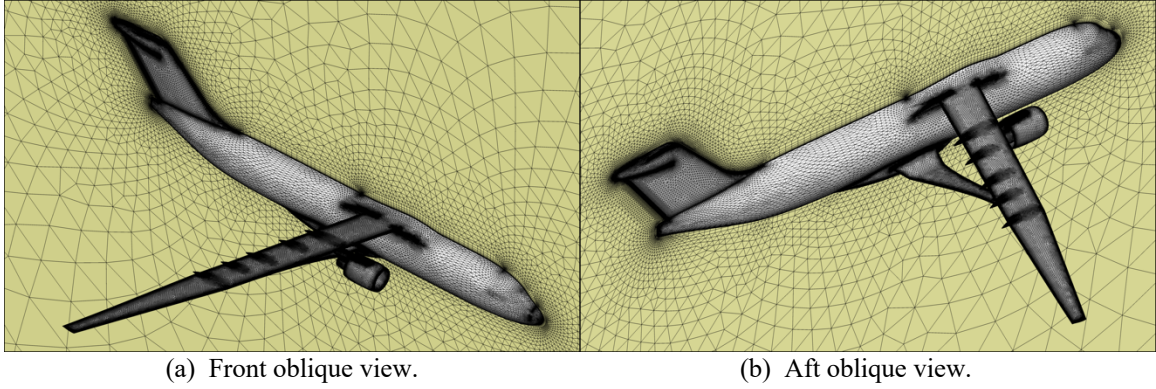
**Figure 5.  Unstructured surface meshes of the TTBW flight WBSNFVJ configuration (HeldenMesh).**



(a)  Front oblique view.          (b)  Aft oblique view.

(c)  Front oblique view, entire model.     (d)  Aft oblique view where sting enters empennage.
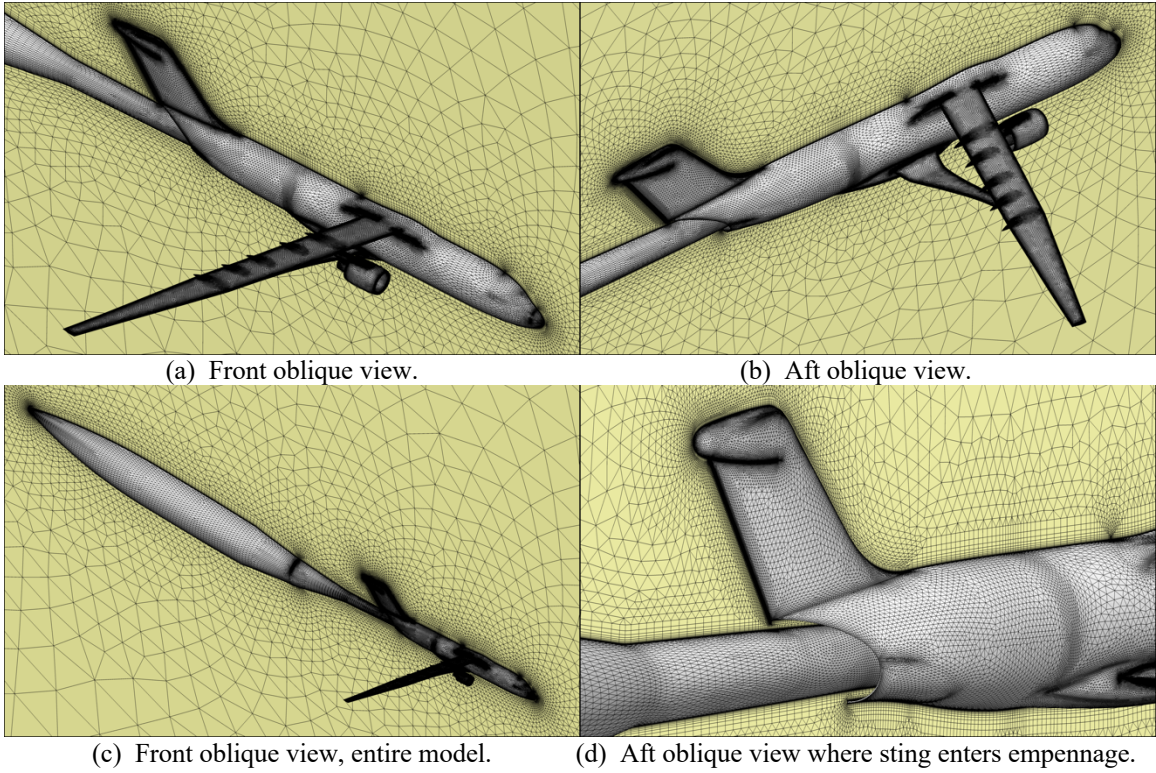
**Figure 6.  Unstructured surface meshes of the TTBW WT WBSNFV configuration (HeldenMesh).**

**Table 3.  Summary of configurations investigated and test conditions.**

| Configuration | $M_\infty$ | Chord Reynolds Number (x $10^6$) | Static Temperature (°R) |
|---|---|---|---|
| Flight WBSNFVJ | 0.80 | 14.03 | 389.97 |
| WT WBSV | 0.80 | 2.17 | 482.16 |
| WT WBSV | 0.80 | 3.31 | 489.15 |
| WT WBSNFV | 0.80 | 2.17 | 480.78 |
| WT WBSNFV | 0.80 | 3.31 | 493.03 |
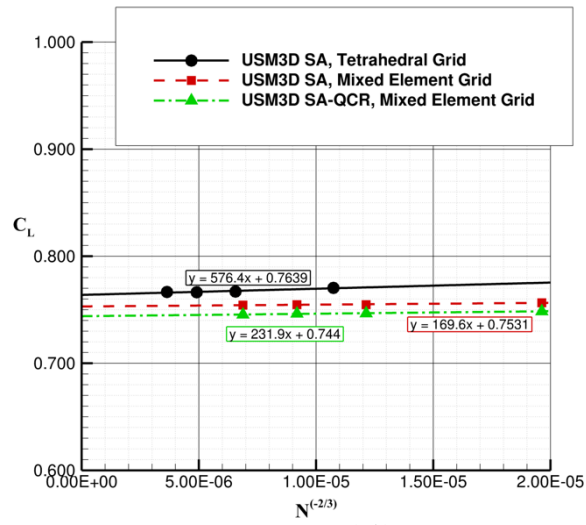
(a) $C_L$ vs. $N^{(-2/3)}$.
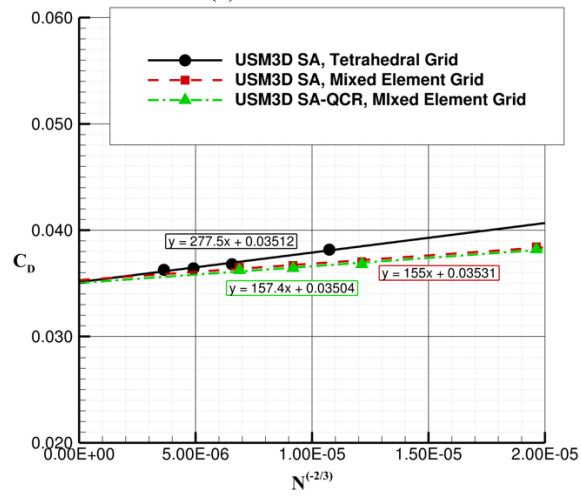


(b) $C_D$ vs. $N^{(-2/3)}$.
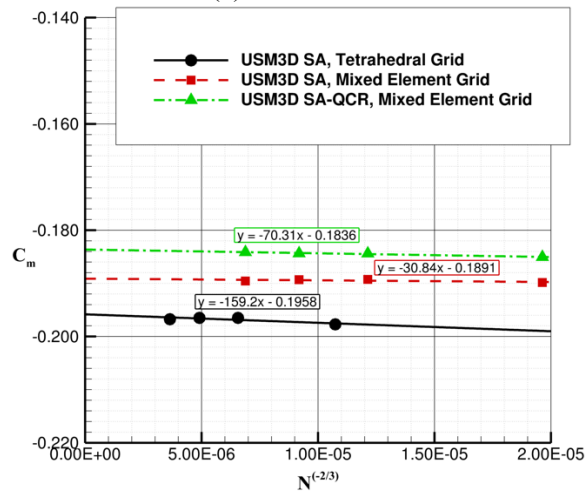


(c) $C_m$ vs. $N^{(-2/3)}$.

**Figure 7. USM3D grid convergence study for the WT WBSNFV configuration at $M_\infty = 0.80$, $Re_c = 3.31 \times 10^6$, $\alpha = 2.0°$, and $\beta = 0°$ (USM3D tetrahedral and mixed-element grids).**

21

**Table 4.  USM3D tetrahedral grid refinement study of the WT WBSNFV configuration at $M_\infty = 0.80$, $Re_c = 3.31$ x $10^6$, $\alpha = 2.0°$, and $\beta = 0°$ (SA turbulence model).**

| Refinement Level | Cells (million) | $C_L$ | $C_D$ | $C_m$ |
|---|---|---|---|---|
| Coarse | 28.41 | 0.7704 | 0.03817 | -0.1977 |
| Medium | 59.46 | 0.7670 | 0.03681 | -0.1965 |
| Fine | 92.03 | 0.7663 | 0.03641 | -0.1965 |
| XFine | 144.02 | 0.7667 | 0.03628 | -0.1967 |
| Asymptotic | - | 0.7639 | 0.03512 | -0.1958 |

**Table 5.  USM3D mixed-element grid refinement study of the WT WBSNFV configuration at $M_\infty = 0.80$, $Re_c = 3.31$ x $10^6$, $\alpha = 2.0°$, and $\beta = 0°$ (SA turbulence model).**

| Refinement Level | Cells (million) | $C_L$ | $C_D$ | $C_m$ |
|---|---|---|---|---|
| Coarse | 11.49 | 0.7565 | 0.03842 | -0.1899 |
| Medium | 23.65 | 0.7547 | 0.03703 | -0.1893 |
| Fine | 35.94 | 0.7547 | 0.03668 | -0.1893 |
| XFine | 55.39 | 0.7544 | 0.03651 | -0.1896 |
| Asymptotic | - | 0.7531 | 0.03531 | -0.1891 |

**Table 6.  USM3D mixed-element grid refinement study of the WT WBSNFV configuration at $M_\infty = 0.80$, $Re_c = 3.31$ x $10^6$, $\alpha = 2.0°$, and $\beta = 0°$ (SA-QCR turbulence model).**

| Refinement Level | Cells (million) | $C_L$ | $C_D$ | $C_m$ |
|---|---|---|---|---|
| Coarse | 11.49 | 0.7486 | 0.03820 | -0.1851 |
| Medium | 23.65 | 0.7466 | 0.03680 | -0.1844 |
| Fine | 35.94 | 0.7464 | 0.03643 | -0.1844 |
| XFine | 55.39 | 0.7455 | 0.03625 | -0.1841 |
| Asymptotic | - | 0.744 | 0.03504 | -0.1836 |
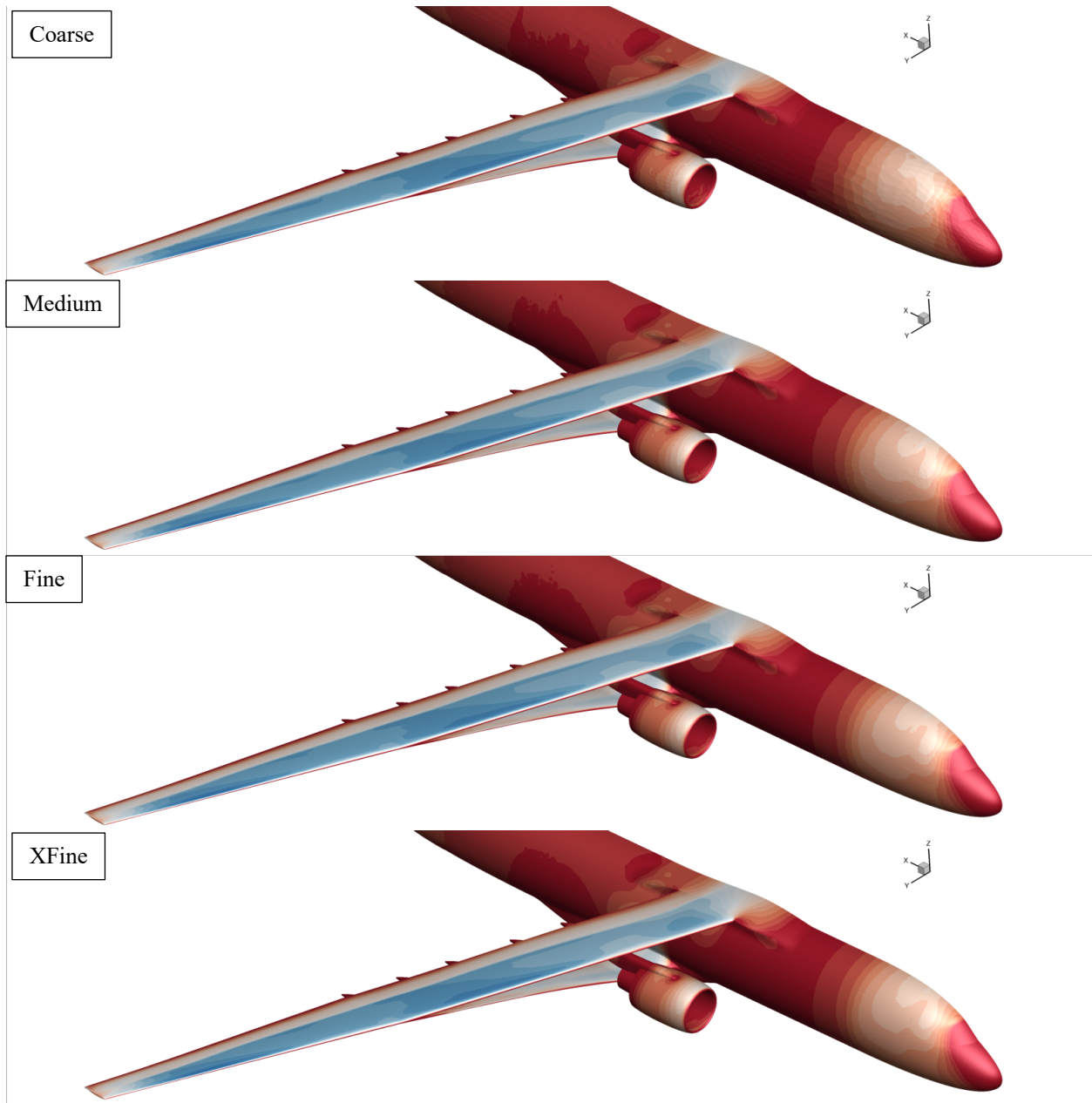
(a)  *$C_P$* Contour Plots for each Grid Level.

**Figure 8.  USM3D *$C_P$* contour plots (a) and $\Delta C_P$ contour plots between grid levels (b) for grid convergence study of WT WBSNFV configuration at *$M_\infty$* = 0.80,  *$Re_c$* = 3.31 x 10⁶, α = 2.0°, and β = 0° (mixed-element grid, SA-QCR turbulence model).**

Medium - Coarse

Fine - Medium

XFine - Fine

(b)  $\Delta C_P$ Contour Plots Between Grid Levels (mapped to XFine surface grid).

**Figure 8 continued.  USM3D $C_P$ contour plots (a) and $\Delta C_P$ contour plots between grid levels (b) for grid convergence study of WT WBSNFV configuration at $M_\infty = 0.80$,  $Re_c = 3.31$ x $10^6$, $\alpha = 2.0°$, and $\beta = 0°$ (mixed-element grid, SA-QCR turbulence model).**

**Table 7.  USM3D medium level grid sizes for configurations investigated.**

| Configuration | Tetrahedral Cells (million) | Mixed-Element Cells (million) |
|---|---|---|
| Flight WBSNFVJ | 55.38 | 23.21 |
| WT WBSV | 41.48 | 16.87 |
| WT WBSNFV | 59.46 | 23.65 |
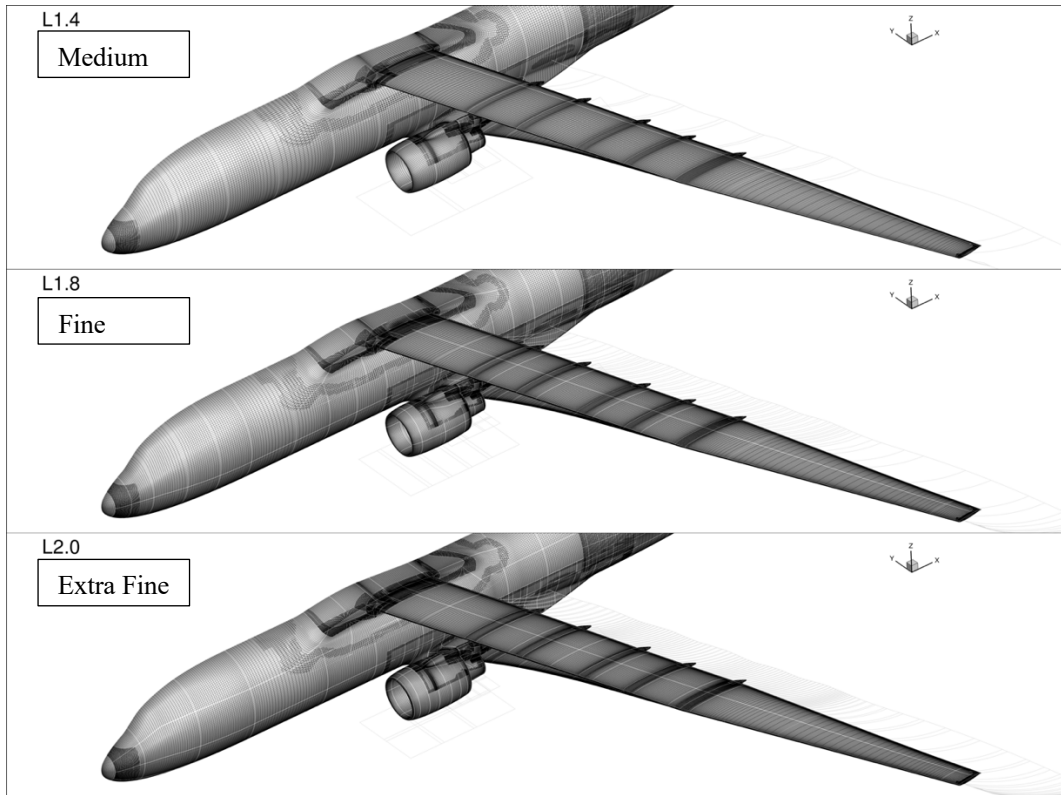
**Figure 9. LAVA grids for grid refinement study of the WT WBSNFV configuration at $M_\infty = 0.80$ and $Re_c = 3.31 \times 10^6$.**

**Table 8. LAVA grid refinement study parameters of the WT WBSNFV configuration at $M_\infty = 0.80$ and $Re_c = 3.31 \times 10^6$.**

| Refinement Factor | $y^+$ | Growth Rate | Vertices (million) | Cores |
|---|---|---|---|---|
| L1.4 | 0.1869 | 1.173 | 54.58 | 320 |
| L1.8 | 0.1456 | 1.132 | 111. 33 | 920 |
| L2.0 | 0.1309 | 1.118 | 150.60 | 1060 |
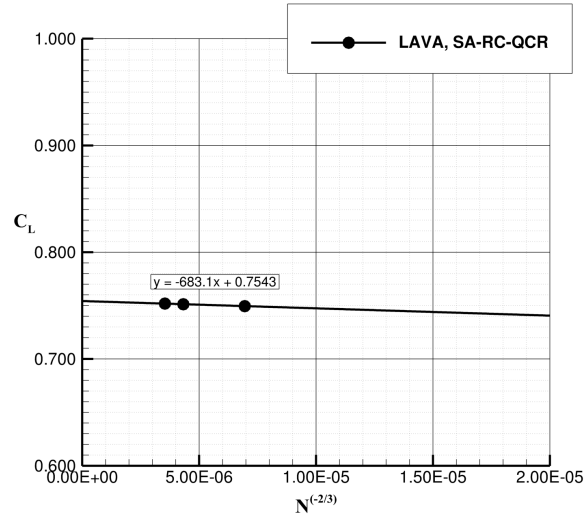
(a) $C_L$ vs. $N^{(-2/3)}$.
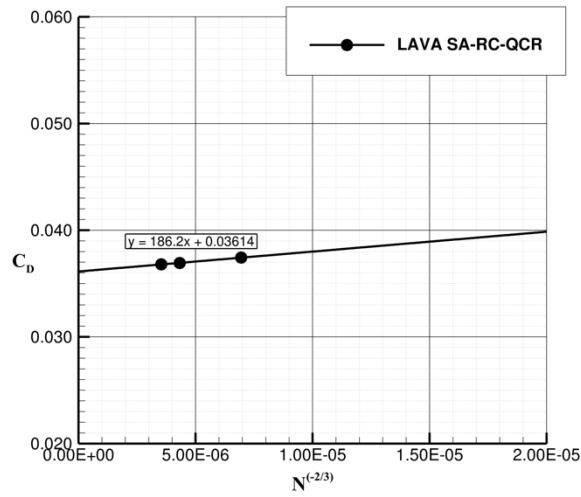


(b) $C_D$ vs. $N^{(-2/3)}$.
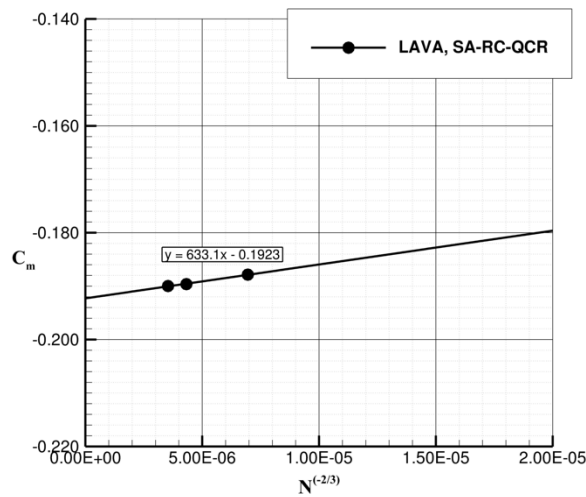


(c) $C_m$ vs. $N^{(-2/3)}$.

**Figure 10. LAVA grid convergence study for WT WBSNFV configuration at $M_\infty = 0.80$, $Re_c = 3.31 \times 10^6$, $\alpha = 2.0°$, and $\beta = 0°$ (LAVA structured overset grids).**

**Table 9. LAVA grid refinement study of the WT WBSNFV configuration at $M_\infty = 0.80$, $Re_c = 3.31 \times 10^6$, $\alpha = 2.0°$, and $\beta = 0°$ (SA-RC-QCR turbulence model).**

| Refinement Level | Vertices (million) | $C_L$ | $C_D$ | $C_m$ |
|---|---|---|---|---|
| L1.4 | 54.58 | 0.7495 | 0.03743 | -0.1879 |
| L1.8 | 111.33 | 0.7513 | 0.03692 | -0.1896 |
| L2.0 | 150.60 | 0.7518 | 0.03680 | -0.1900 |
| Asymptotic | - | 0.7543 | 0.03614 | -0.1923 |
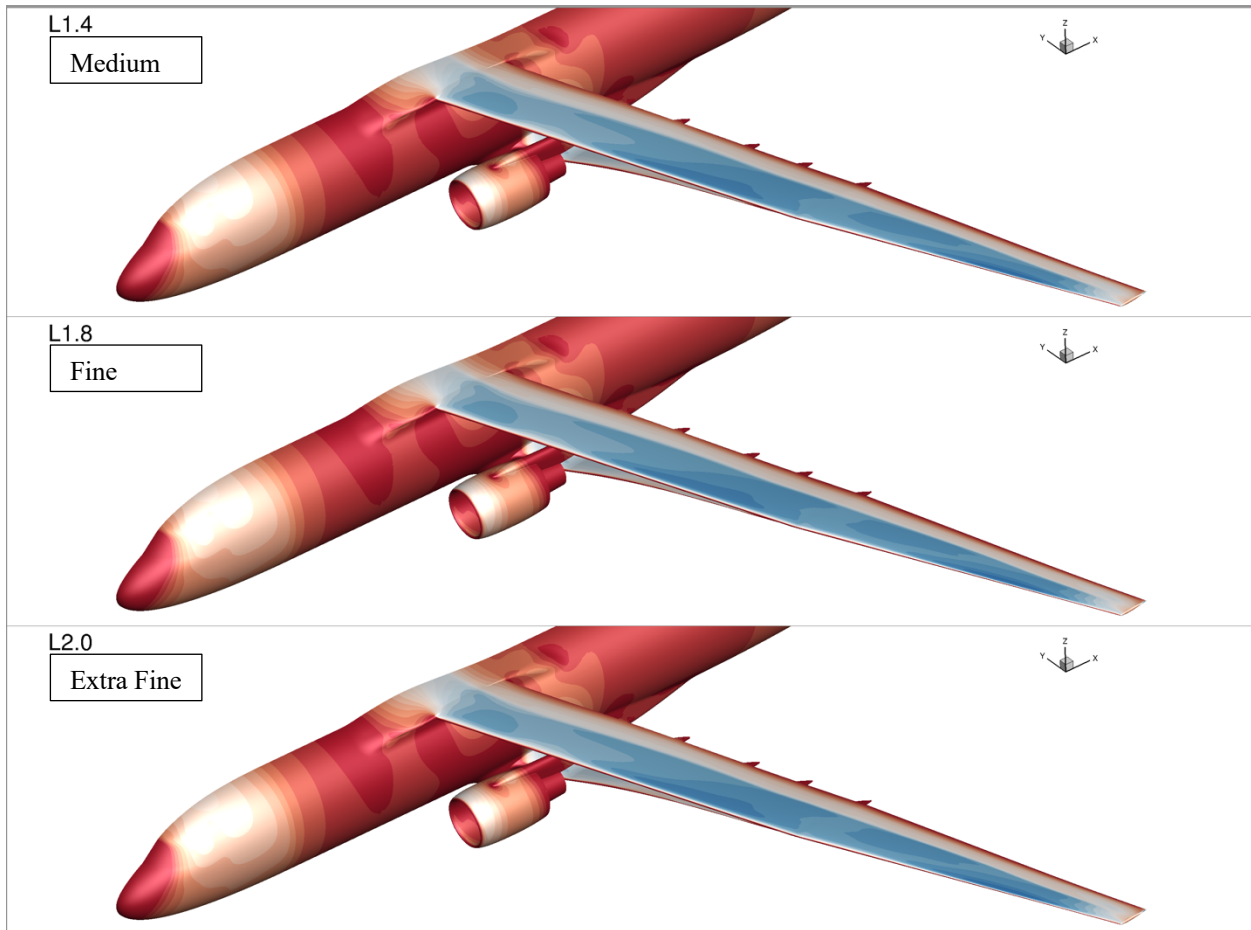


(a) $C_P$ Contour Plots for each Grid Level.

**Figure 11. LAVA grid refinement study $C_P$ contour plots (a) and $\Delta C_P$ contour plots between grid levels (b) for WT WBSNFV configuration at $M_\infty = 0.80$, $Re_c = 3.31 \times 10^6$, $\alpha = 2.0°$, and $\beta = 0°$.**

Fine - Medium
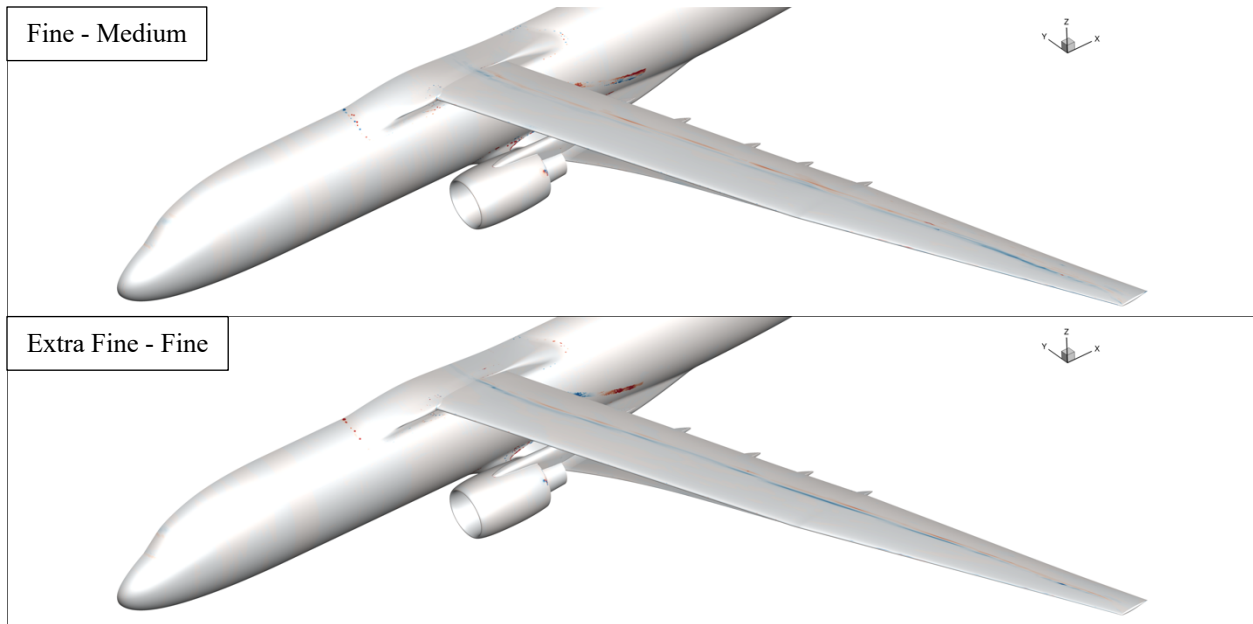
Extra Fine - Fine

(b) $\Delta C_P$ Contour Plots Between Grid Levels (mapped to Extra Fine surface grid).

**Figure 11 continued. LAVA grid refinement study $C_P$ contour plots (a) and $\Delta C_P$ contour plots between grid levels (b) for WT WBSNFV configuration at $M_\infty = 0.80$, $Re_c = 3.31 \times 10^6$, $\alpha = 2.0°$, and $\beta = 0°$.**
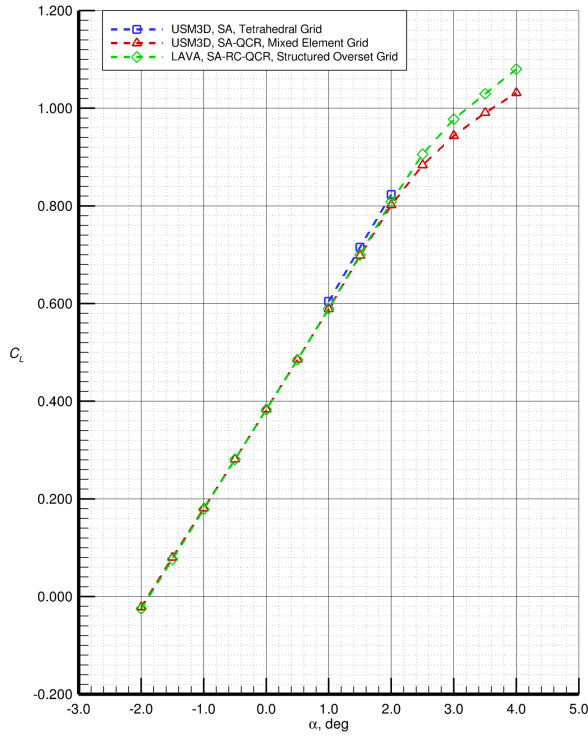
(a) $C_L$ vs $\alpha$.
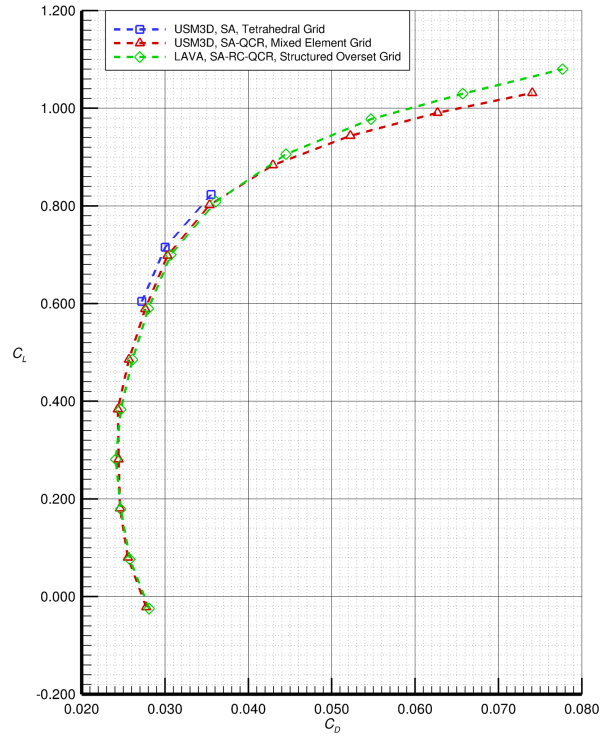
(b) $C_L$ vs $C_D$.
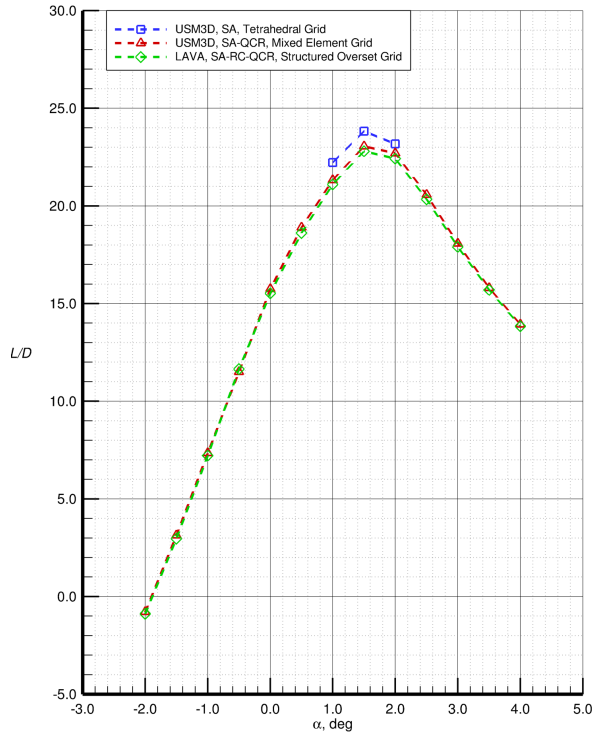
(c) $L/D$ vs $\alpha$.
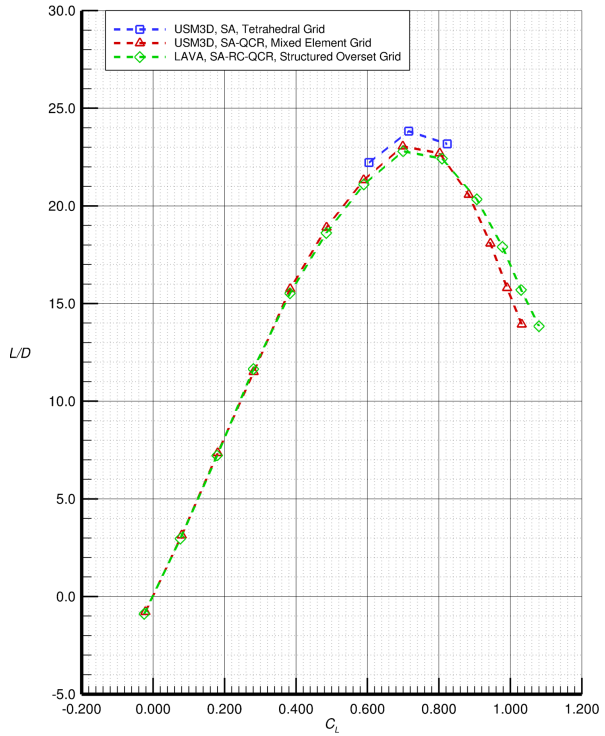
(d) $L/D$ vs $C_L$.

**Figure 12. CFD code-to-code comparison for the flight WBSNFVJ configuration at $M_\infty = 0.80$, $Re_c = 14.03$ x $10^6$, $-2° \le \alpha \le 4°$, and $\beta = 0°$.**
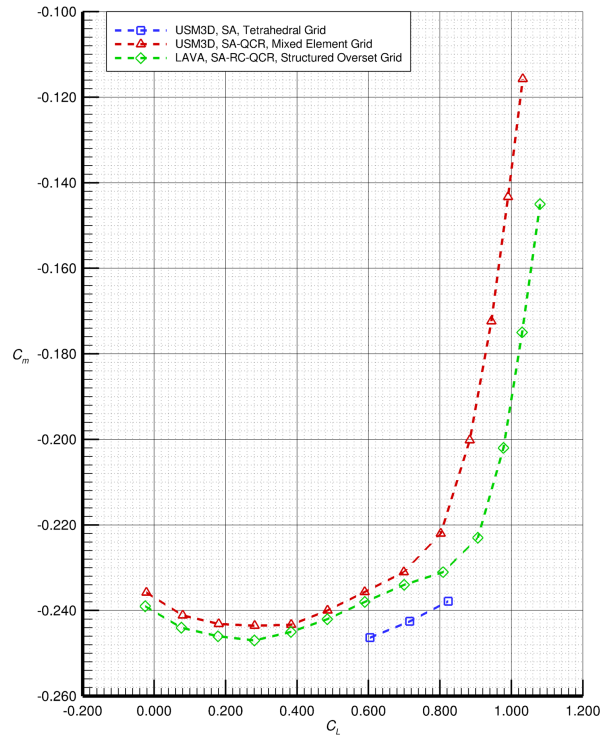
(e) $C_m$ vs $C_L$.

**Figure 12 continued.  CFD code-to-code comparison for the flight WBSNFVJ configuration at $M_\infty$ = 0.80, $Re_c$ = 14.03 x 10^6, -2° ≤ α ≤ 4°, and β = 0°.**
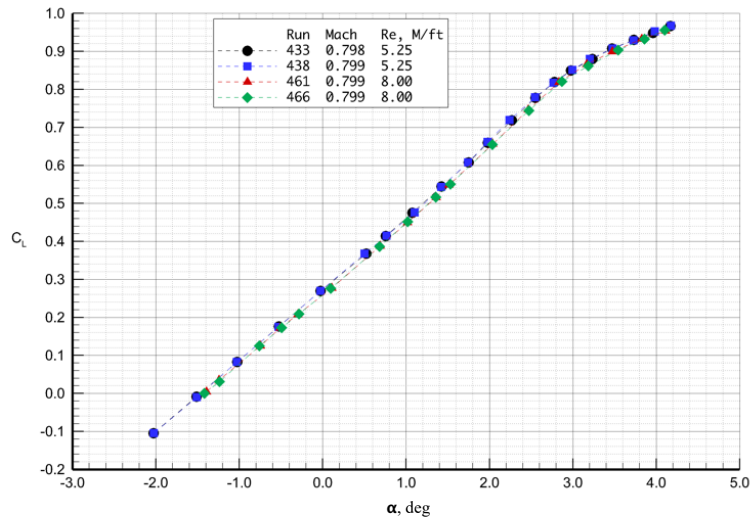
(a) $C_L$ vs $\alpha$.
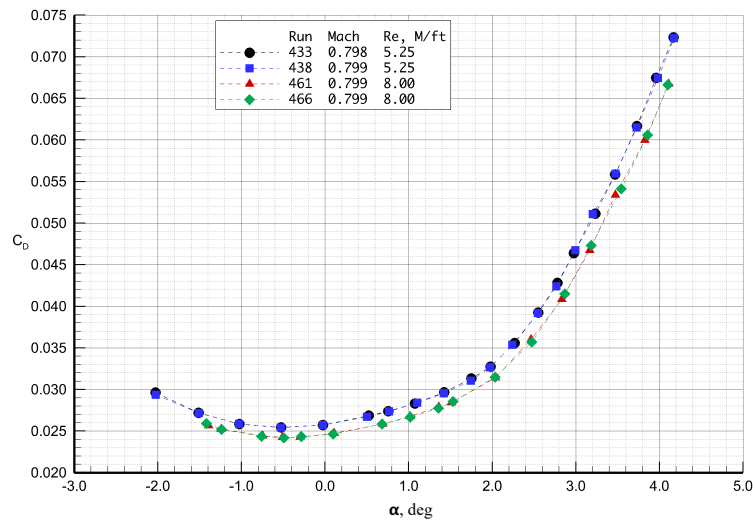


(b) $C_D$ vs $\alpha$.

**Figure 13.  Run-to-run data repeatability for WT WBSV configuration at $M_\infty = 0.80$, $Re_c = 2.17$ x $10^6$ ($Re = 5.25$ x $10^6$/ft) and $Re_c = 3.31$ x $10^6$ ($Re = 8.00$ x $10^6$/ft), $-2° \leq \alpha < 5°$, and $\beta = 0°$.**

(c) $C_m$ vs $\alpha$.



(d) $C_L$ vs $C_D$.

**Figure 13 continued.  Run-to-run data repeatability for WT WBSV configuration at $M_\infty = 0.80$, $Re_c = 2.17 \times 10^6$ ($Re = 5.25 \times 10^6$/ft ) and $Re_c = 3.31 \times 10^6$ ($Re = 8.00 \times 10^6$/ft), $-2^\circ \leq \alpha < 5^\circ$, and $\beta = 0^\circ$.**
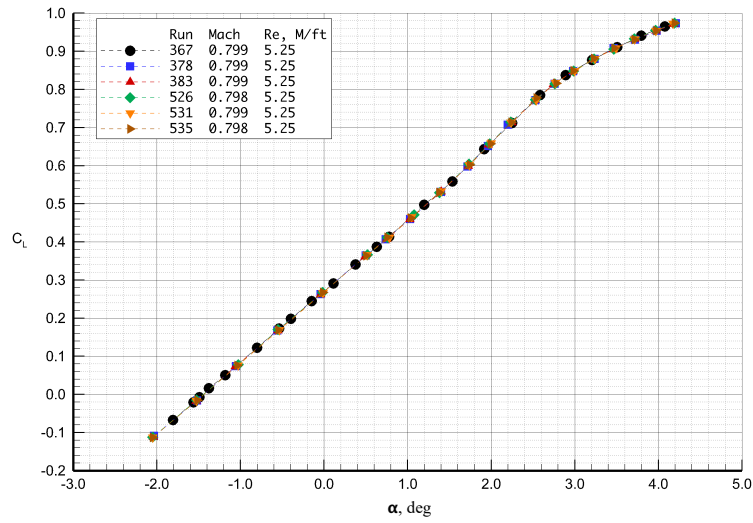
(a) $C_L$ vs $\alpha$.
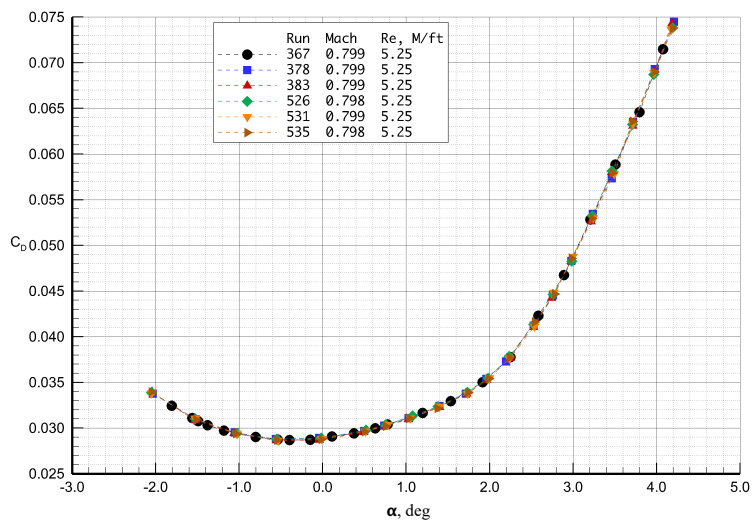


(b) $C_D$ vs $\alpha$.

**Figure 14. Run-to-run data repeatability for WT WBSNFV configuration at $M_\infty = 0.80$ and $Re_c = 2.17 \times 10^6$ ($Re = 5.25 \times 10^6$/ft), $-2° \leq \alpha < 5°$, and $\beta = 0°$.**
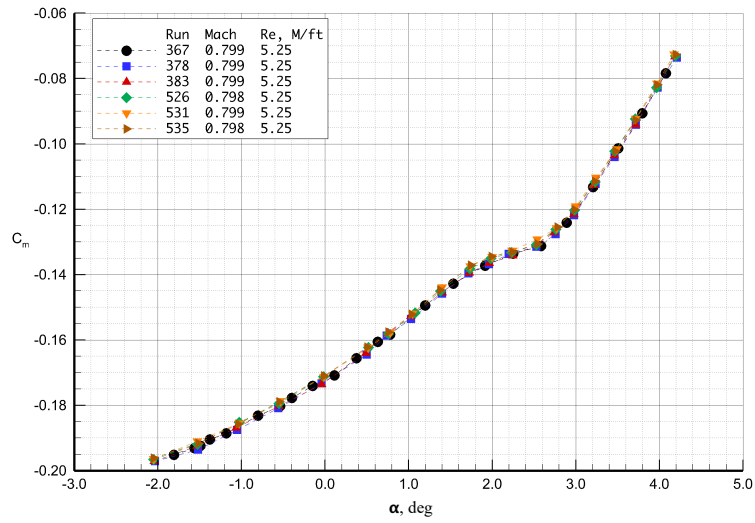
(c) $C_m$ vs $\alpha$.
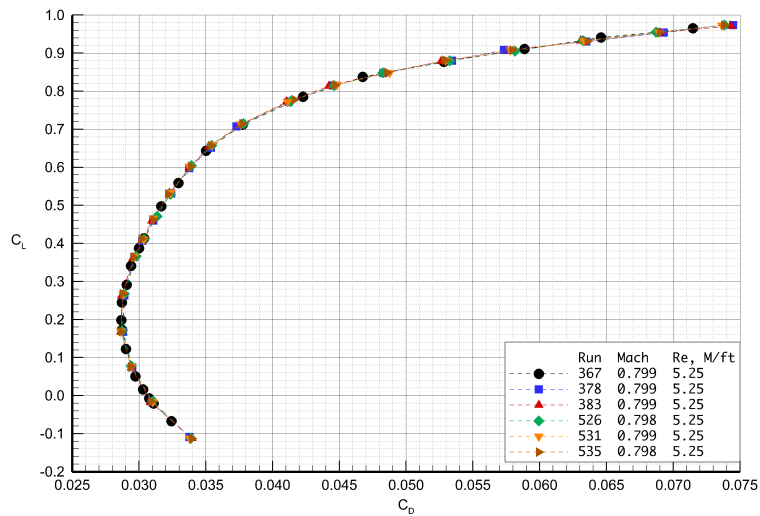


(d) $C_L$ vs $C_D$.

**Figure 14 continued.  Run-to-run data repeatability for WT WBSNFV configuration at $M_\infty = 0.80$ and $Re_c = 2.17 \times 10^6$ ($Re = 5.25 \times 10^6$/ft), $-2° \leq \alpha < 5°$, and $\beta = 0°$.**
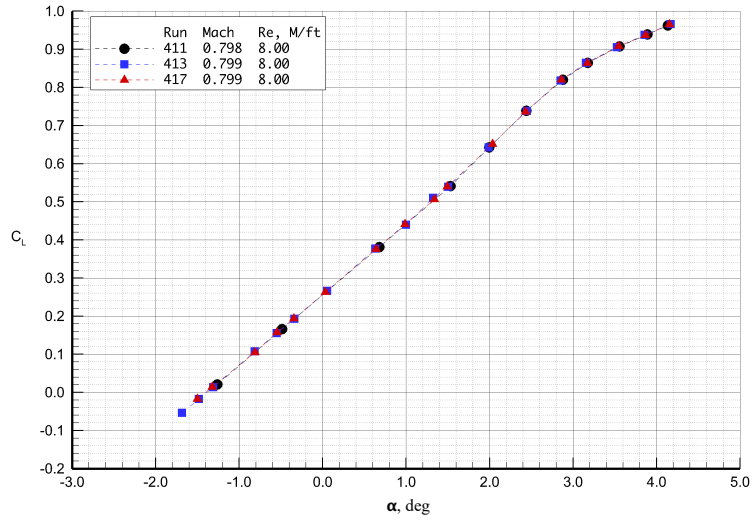
(a) $C_L$ vs $\alpha$.
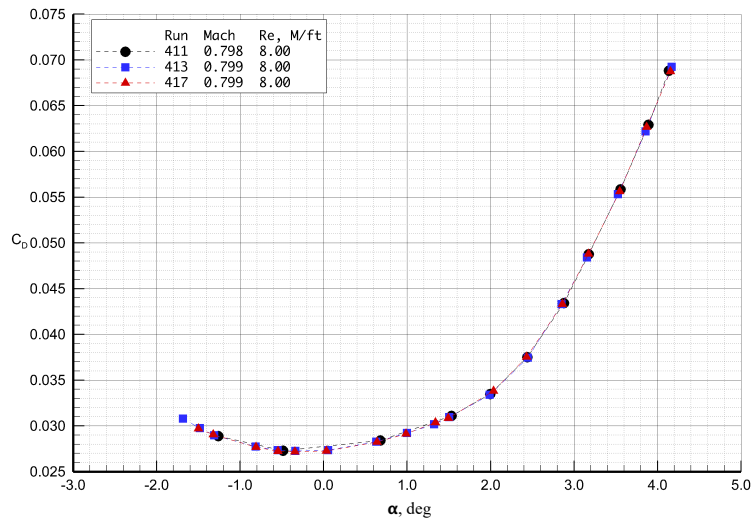


(b) $C_D$ vs $\alpha$.

**Figure 15. Run-to-run data repeatability for WT WBSNFV configuration at $M_\infty = 0.80$ and $Re_c = 3.31 \times 10^6$ ($Re = 8.0 \times 10^6$/ft), $-2° < \alpha < 5°$, and $\beta = 0°$.**
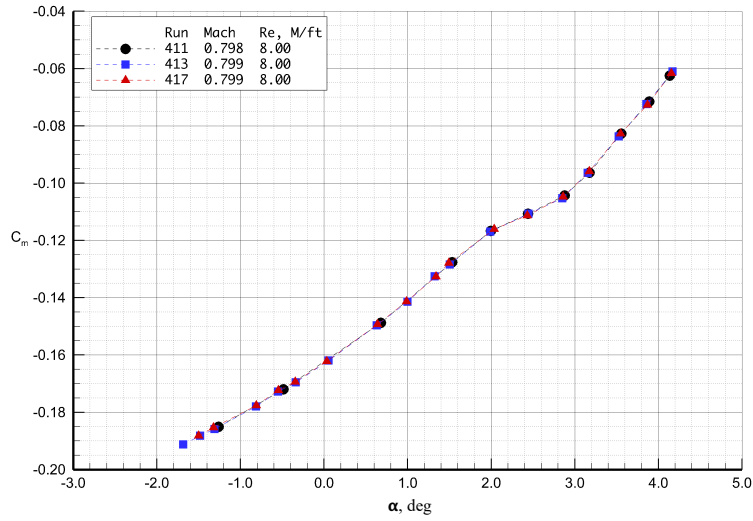
(c) $C_m$ vs $\alpha$.
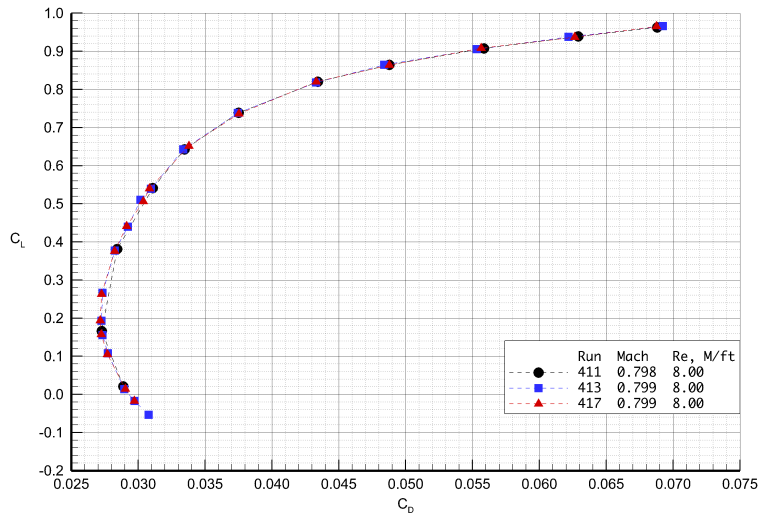


(d) $C_L$ vs $C_D$.

**Figure 15 continued. Run-to-run data repeatability for WT WBSNFV configuration at $M_\infty = 0.80$ and $Re_c =$ 3.31 x $10^6$ ($Re$ = 8.00 x $10^6$/ft), $-2° < \alpha < 5°$, and $\beta = 0°$.**

**Table 10. Experimental runs selected for the WT configuration computational studies at $M_\infty = 0.80$.**

| Configuration | Chord Reynolds Number (x $10^6$) | Experimental Run |
|---|---|---|
| WT WBSV | 2.17 | 433 |
| WT WBSV | 3.31 | 461 |
| WT WBSNFV | 2.17 | 378 |
| WT WBSNFV | 3.31 | 413 |
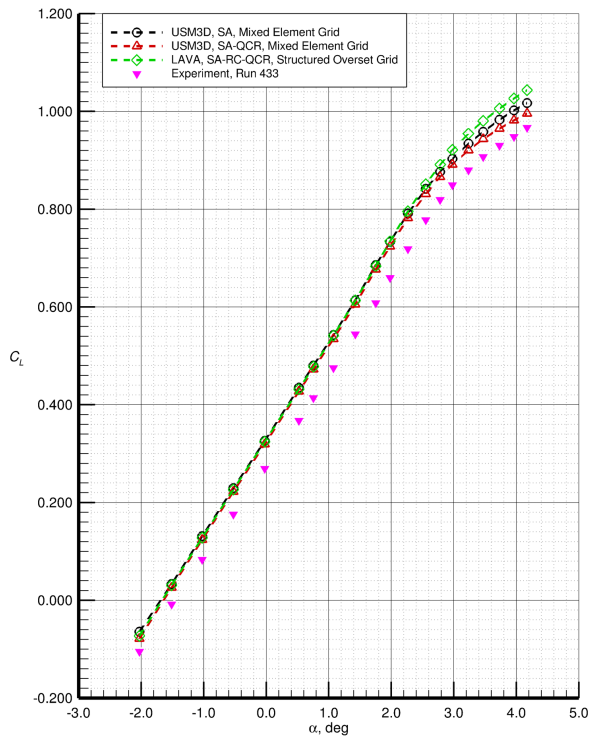
(a)  $C_L$ vs $\alpha$.
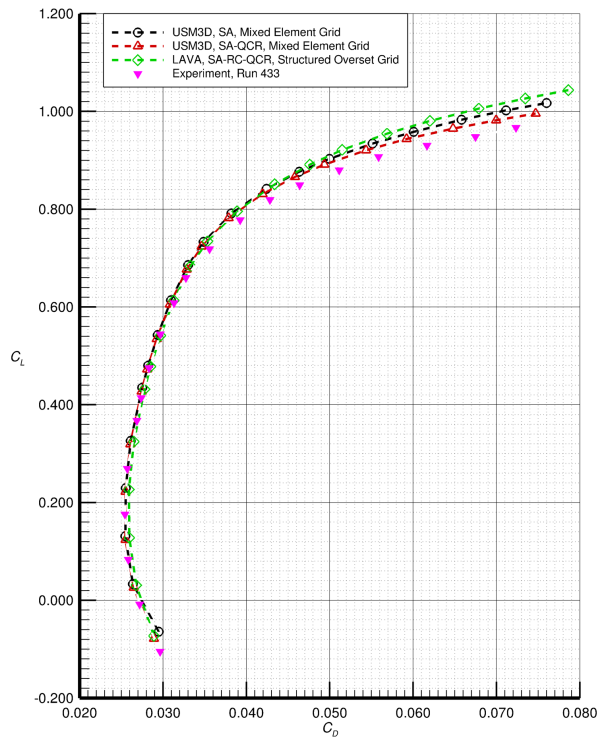
(b)  $C_L$ vs $C_D$.
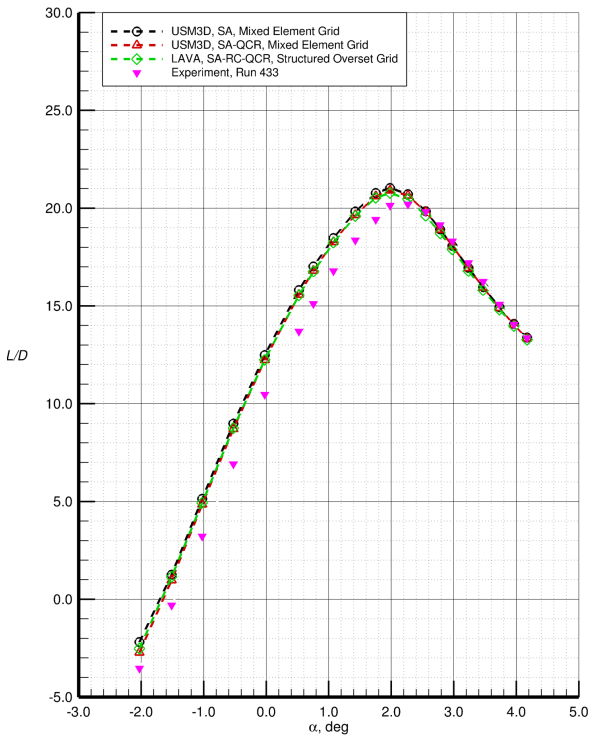
(c)  $L/D$ vs $\alpha$.
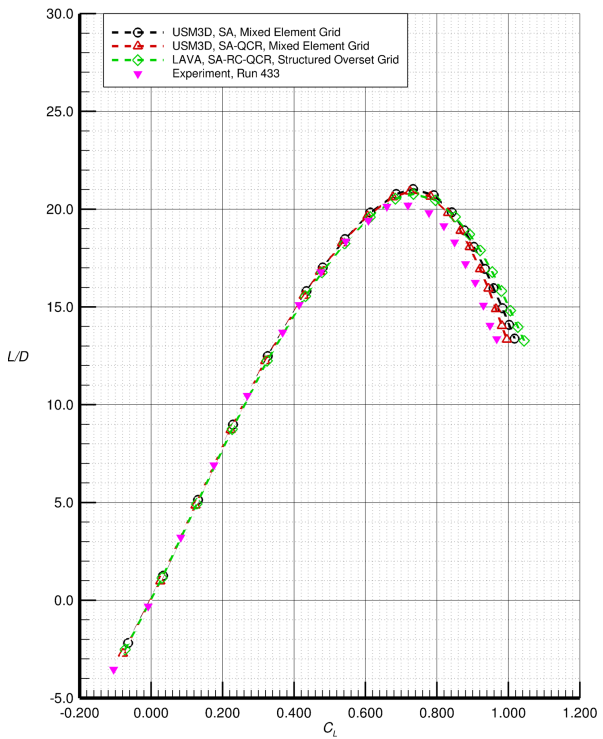
(d)  $L/D$ vs $C_L$.

**Figure 16.  Comparison of CFD and wind-tunnel data for the WT WBSV configuration at $M_\infty = 0.80$, $Re_c = 2.17$ x $10^6$, and $\beta = 0°$ ( $X_{mrc} = 37.03$ in, model scale).**
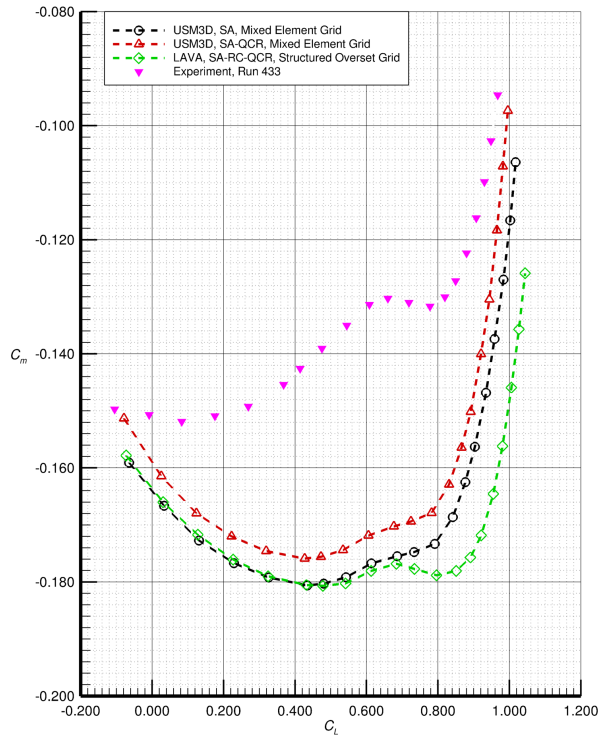
(e)  $C_m$ vs $C_L$.
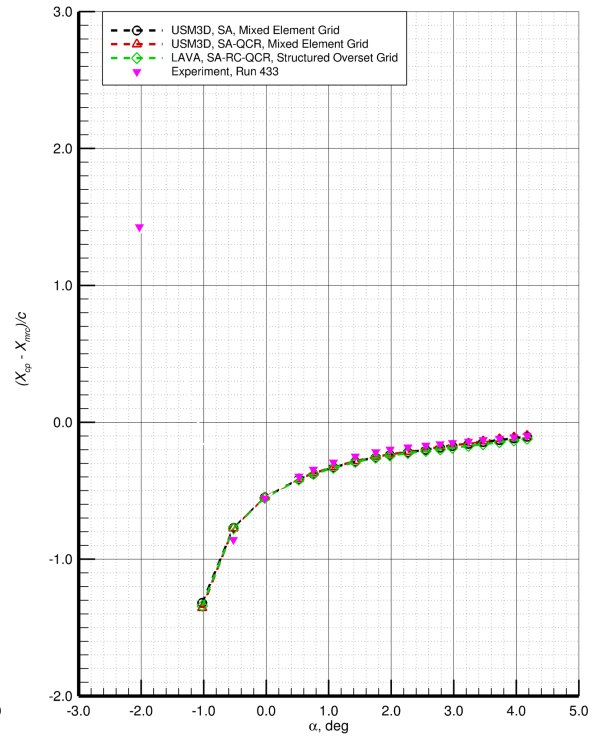
(f)  $(X_{cp} - X_{mrc})/c$ vs $\alpha$.

**Figure 16 continued. Comparison of CFD and wind-tunnel data for the WT WBSV configuration at $M_\infty = 0.80$, $Re_c = 2.17 \times 10^6$, and $\beta = 0^\circ$ ($X_{mrc} = 37.03$ in, model scale).**
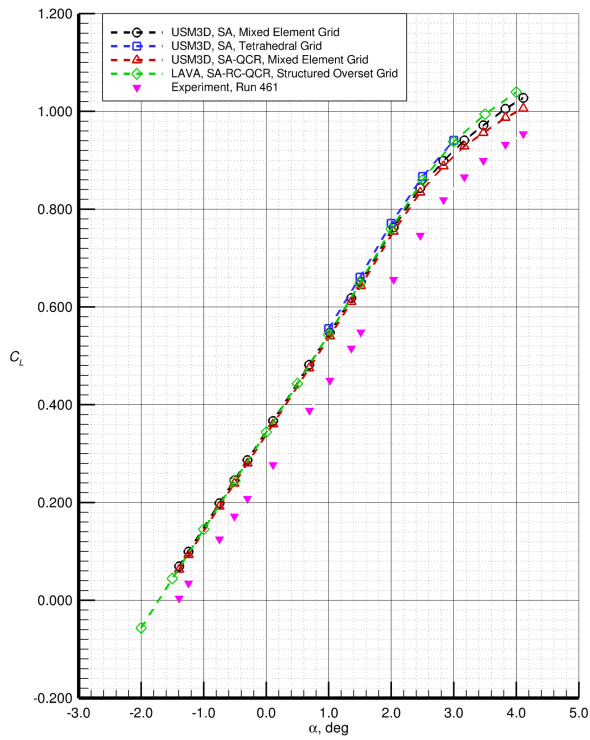
(a) $C_L$ vs $\alpha$.
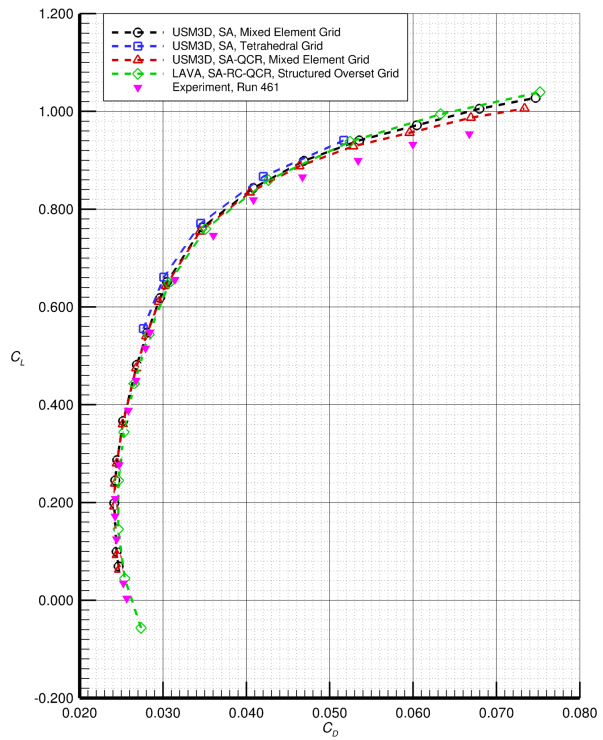
(b) $C_L$ vs $C_D$.
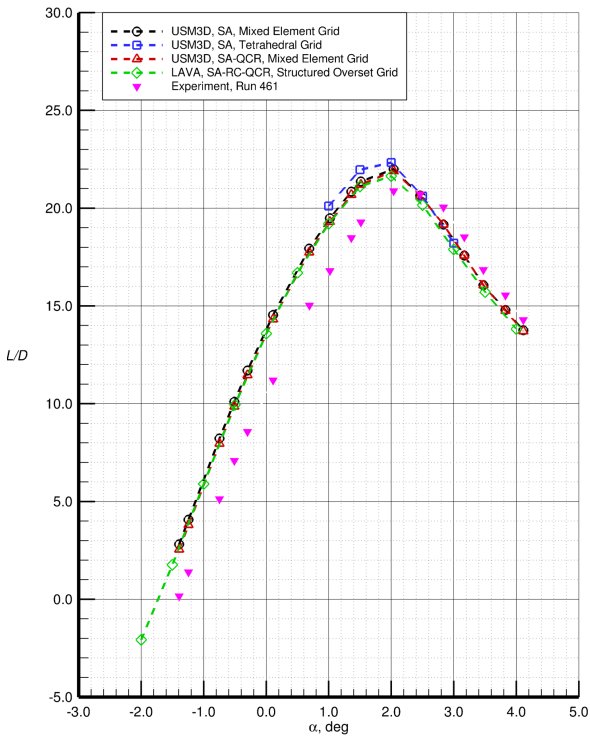
(c) $L/D$ vs $\alpha$.
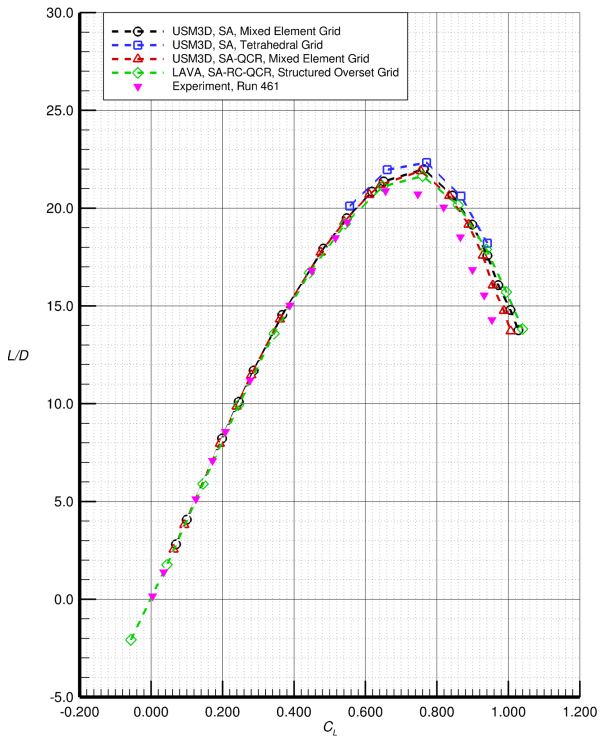
(d) $L/D$ vs $C_L$.

**Figure 17. Comparison of CFD and wind-tunnel data for the WT WBSV configuration at $M_\infty = 0.80$, $Re_c = 3.31$ x $10^6$, and $\beta = 0°$ ( $X_{mrc} = 37.03$ in, model scale).**
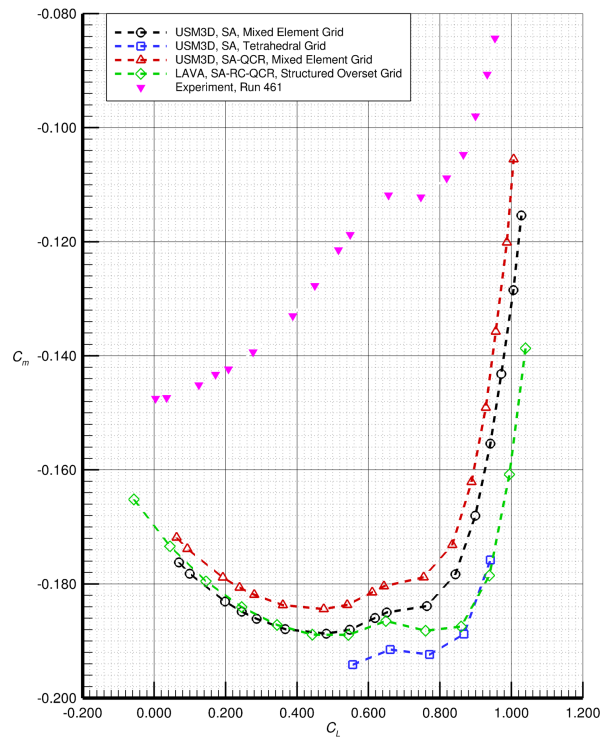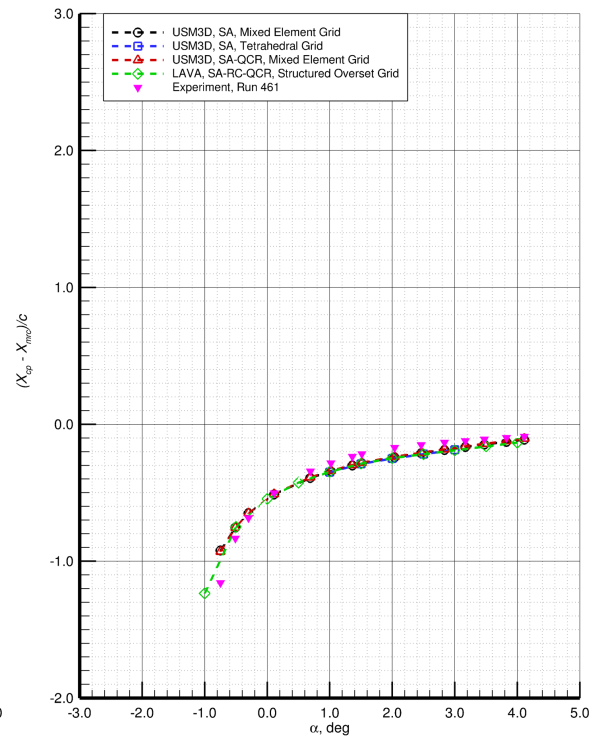
(e) $C_m$ vs $C_L$.  (f) $(X_{cp} - X_{mrc})/c$ vs $\alpha$.

**Figure 17 continued. Comparison of CFD and wind-tunnel data for the WT WBSV configuration at $M_\infty = 0.80$, $Re_c = 3.31 \times 10^6$, and $\beta = 0°$ ( $X_{mrc} = 37.03$ in, model scale).**
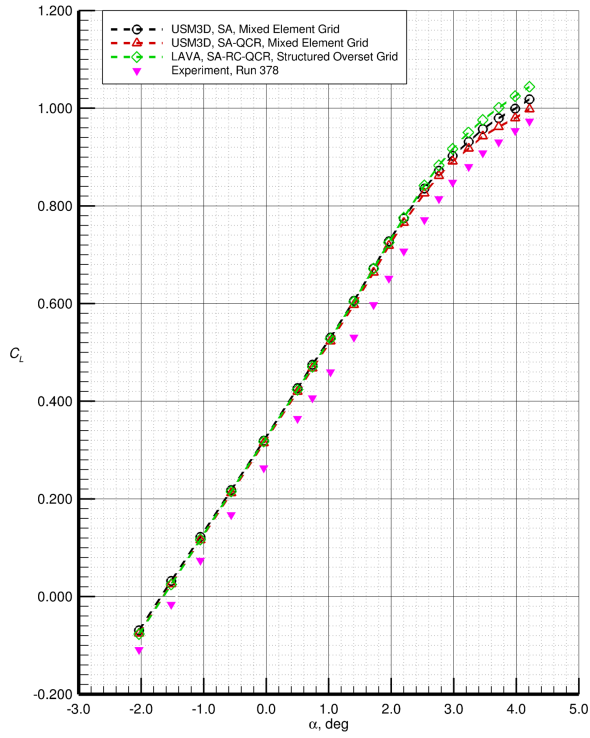
(a) $C_L$ vs $\alpha$.
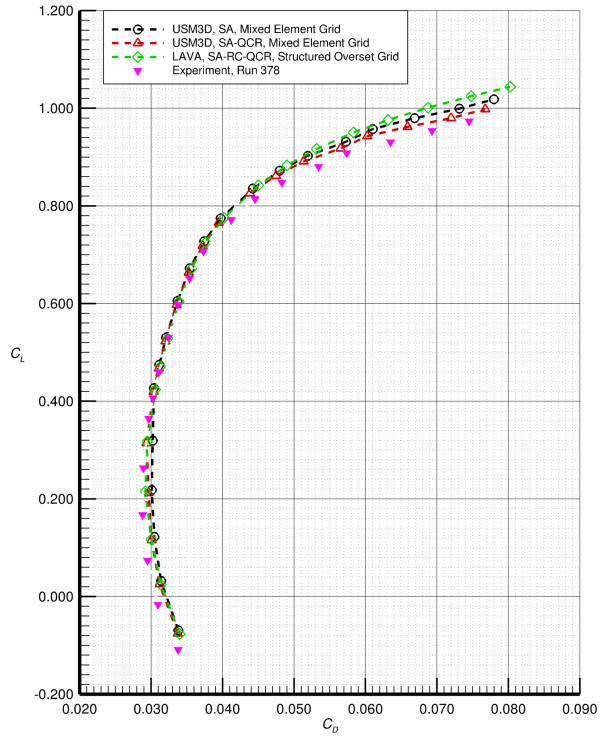
(b) $C_L$ vs $C_D$.
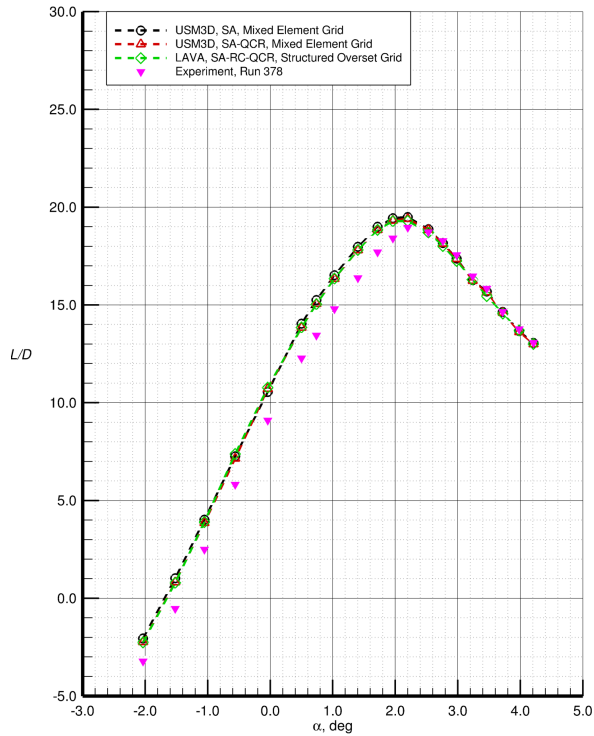
(c) $L/D$ vs $\alpha$.
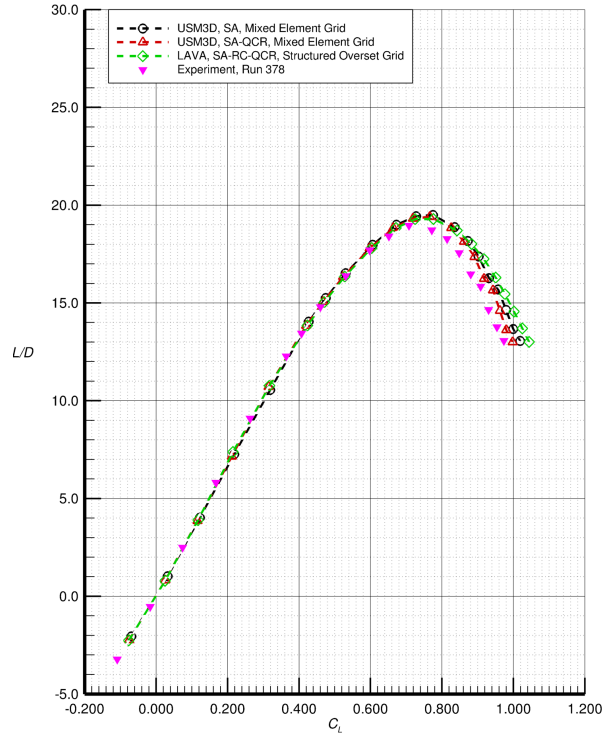
(d) $L/D$ vs $C_L$.

**Figure 18. Comparison of CFD and wind-tunnel data for the WT WBSNFV configuration at $M_\infty = 0.80$, $Re_c = 2.17 \times 10^6$, and $\beta = 0°$ ( $X_{mrc} = 37.03$ in, model scale).**
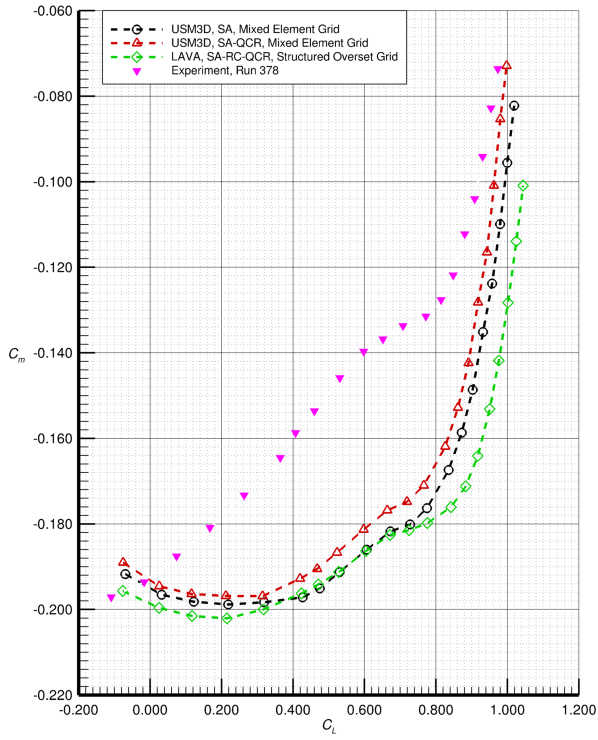
(e)  $C_m$ vs $C_L$.
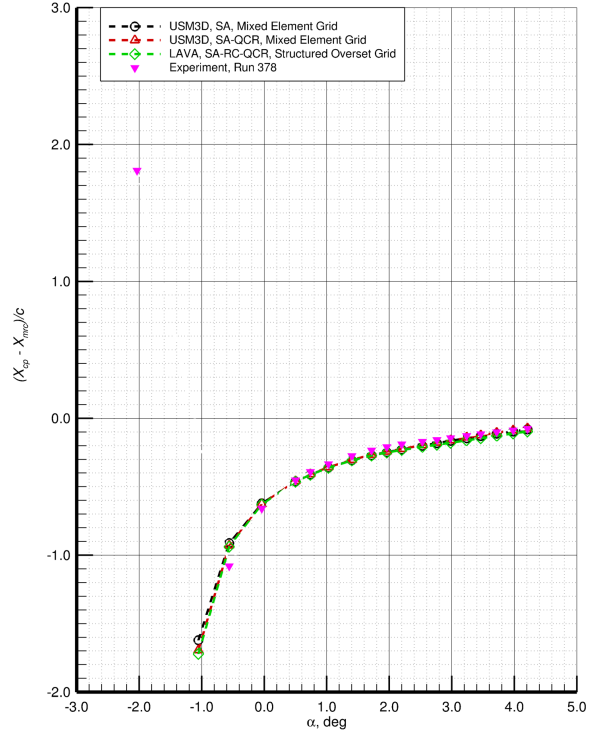


(f)  $(X_{cp} - X_{mrc})/c$ vs $\alpha$.

**Figure 18 continued.  Comparison of CFD and wind-tunnel data for the WT WBSNFV configuration at $M_\infty$ = 0.80, $Re_c$ = 2.17 x 10^6, and $\beta$ = 0° ( $X_{mrc}$ = 37.03 in, model scale).**
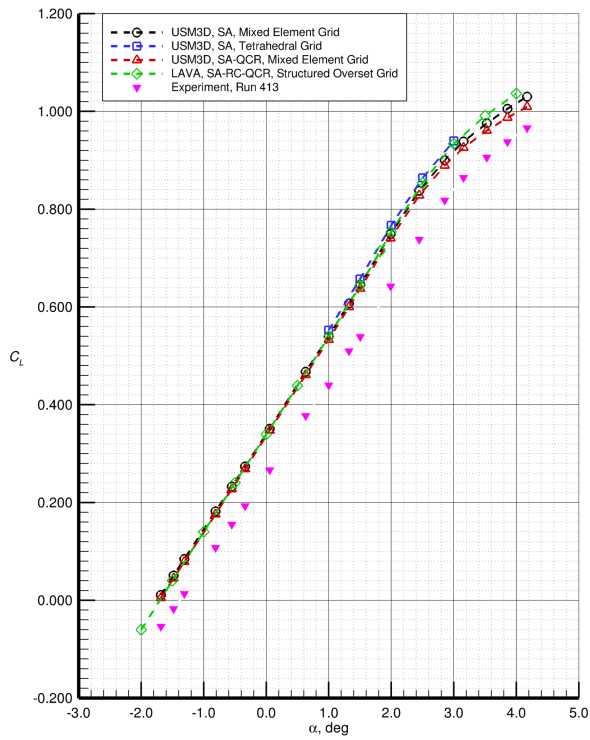
(a) $C_L$ vs $\alpha$.
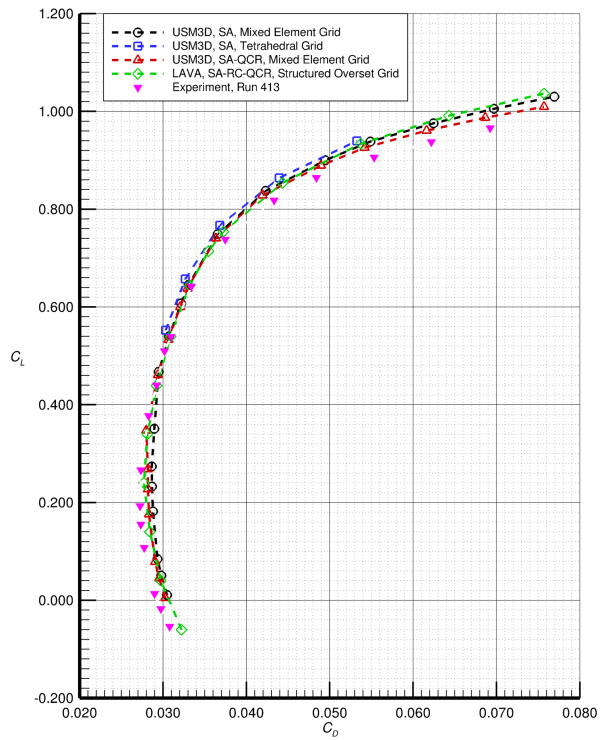
(b) $C_L$ vs $C_D$.
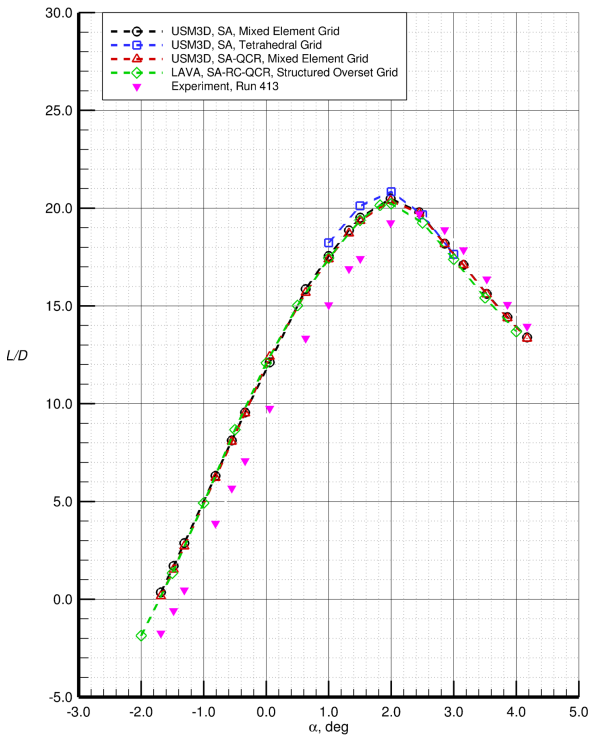
(c) $L/D$ vs $\alpha$.
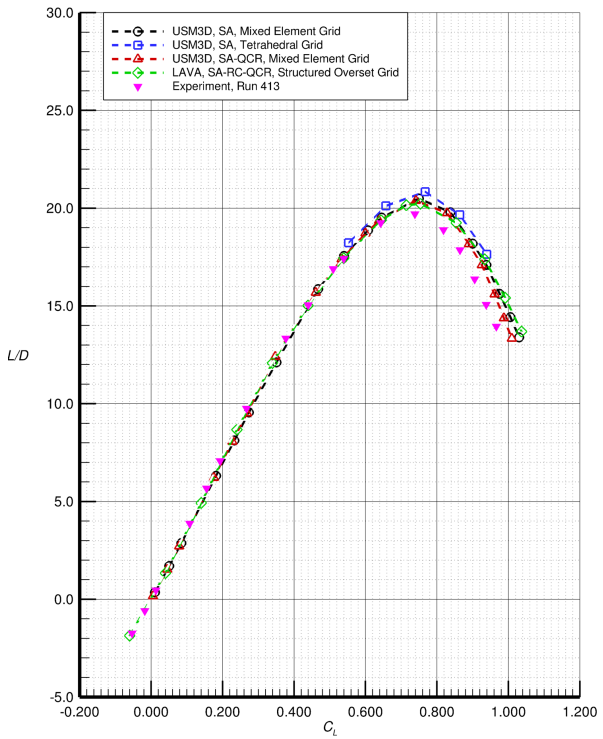
(d) $L/D$ vs $C_L$.

**Figure 19.  Comparison of CFD and wind-tunnel data for the WT WBSNFV configuration at $M_\infty = 0.80$, $Re_c = 3.31 \times 10^6$, and $\beta = 0°$ ( $X_{mrc} = 37.03$ in, model scale).**
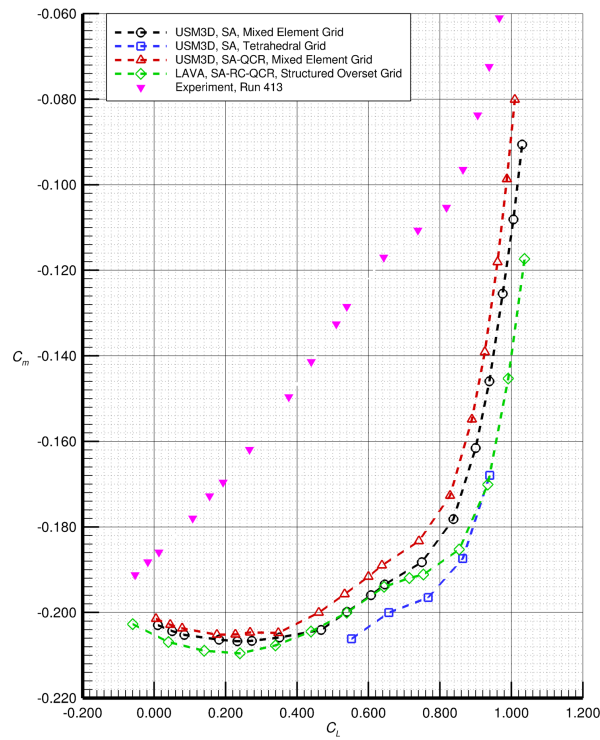
(e)  $C_m$ vs $C_L$.
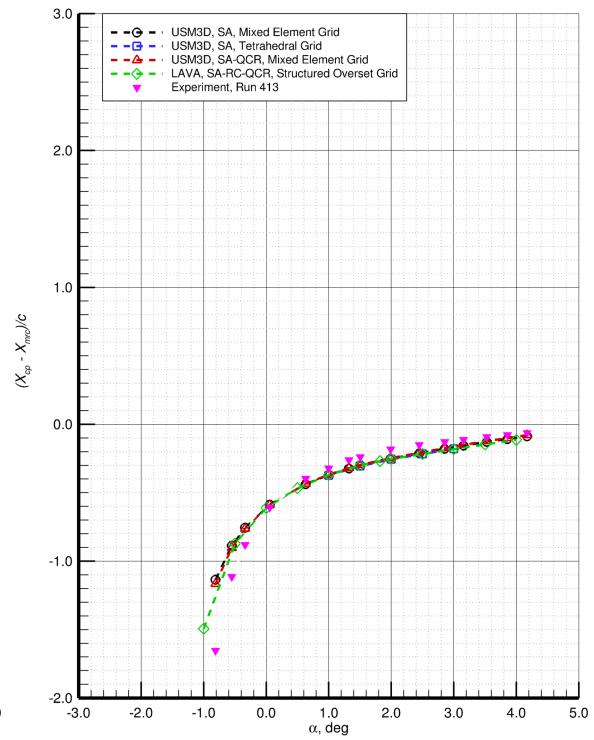
(f)  $(X_{cp} - X_{mrc})/c$ vs $\alpha$.

**Figure 19 continued.  Comparison of CFD and wind-tunnel data for the WT WBSNFV configuration at $M_\infty =$ 0.80, $Re_c$ = 3.31 x 10$^6$, and $\beta = 0°$ ( $X_{mrc}$ = 37.03 in, model scale).**

**Table 11.  Cases investigated for comparison of CFD and wind-tunnel constant spanwise cuts of pressure coefficient data at $M_\infty$ = 0.80 and $Re_c$ = 2.17 x 10$^6$.**

| Configuration | Experimental Run | Test Point $C_L$ Values | | |
|---|---|---|---|---|
| WT WBSV | 433 | 0.176 | 0.719 | 0.849 |
| WT WBSNFV | 378 | 0.168 | 0.707 | 0.848 |

44
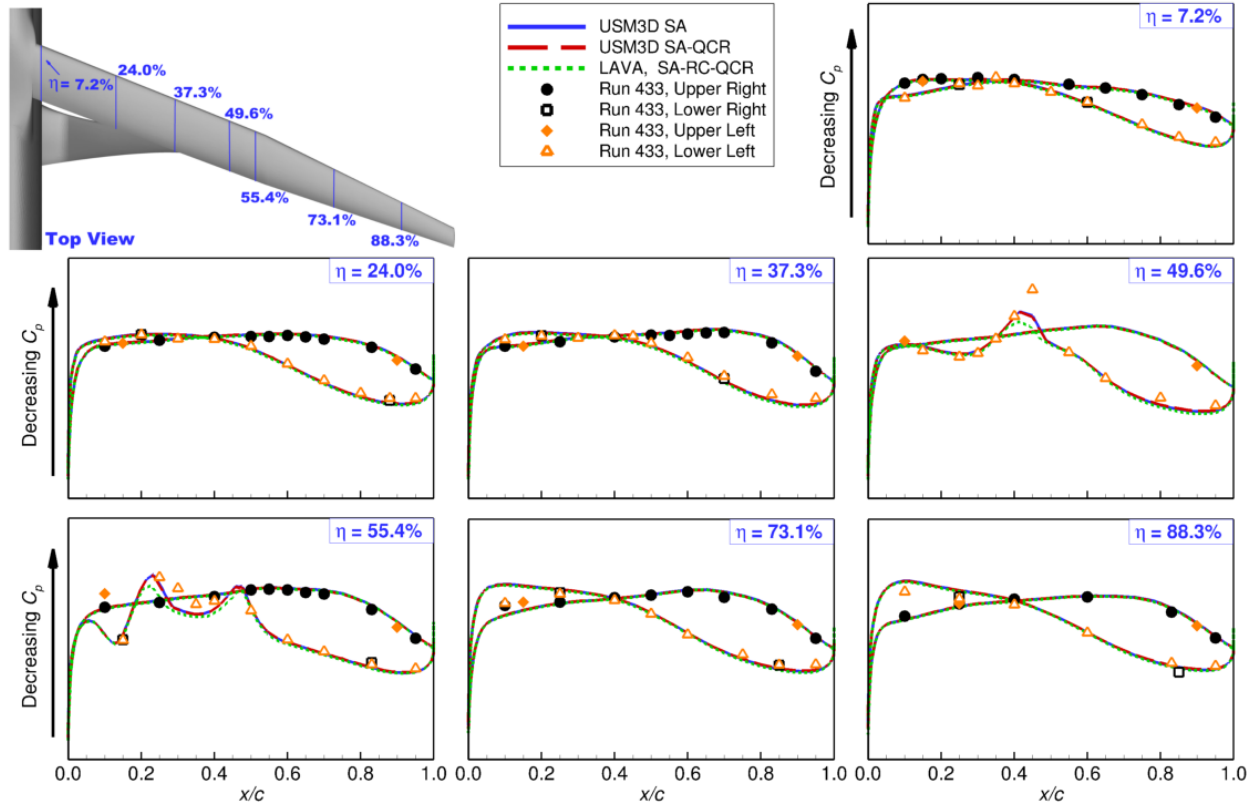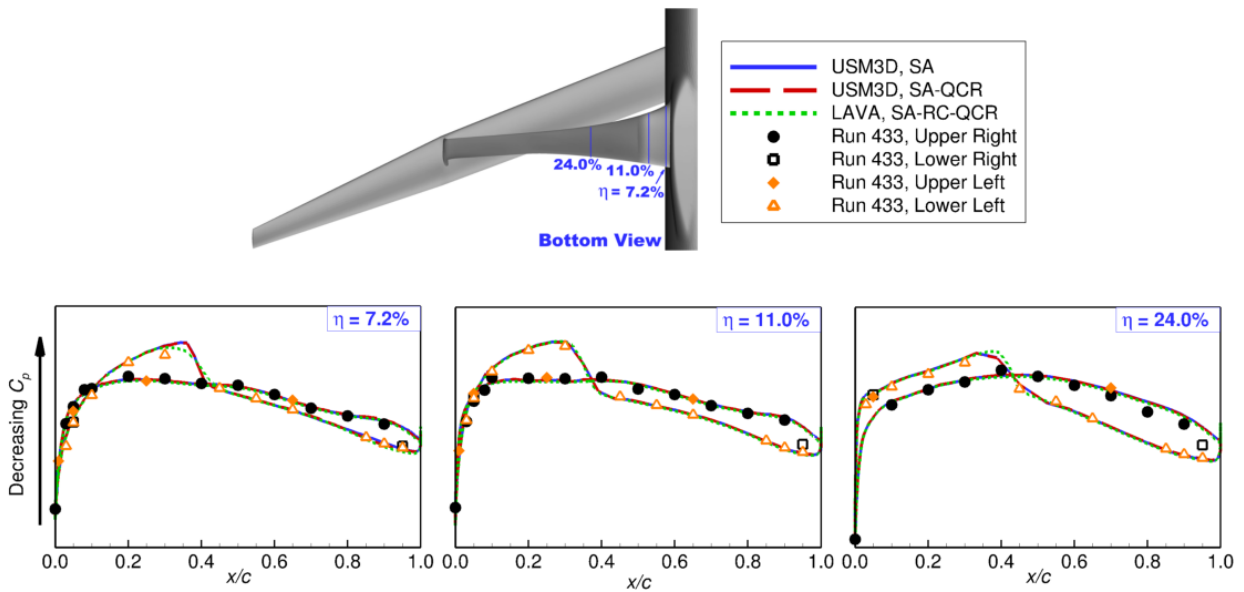
(a) $C_P$ cuts on wing.



(b) $C_P$ cuts on strut.

**Figure 20. Comparison of spanwise $C_P$ cuts for CFD and wind-tunnel data for the WT WBSV configuration at $M_\infty = 0.80$, $Re_c = 2.17 \times 10^6$, $C_L = 0.176$, and $\beta = 0°$ (USM3D mixed-element grid solutions).**
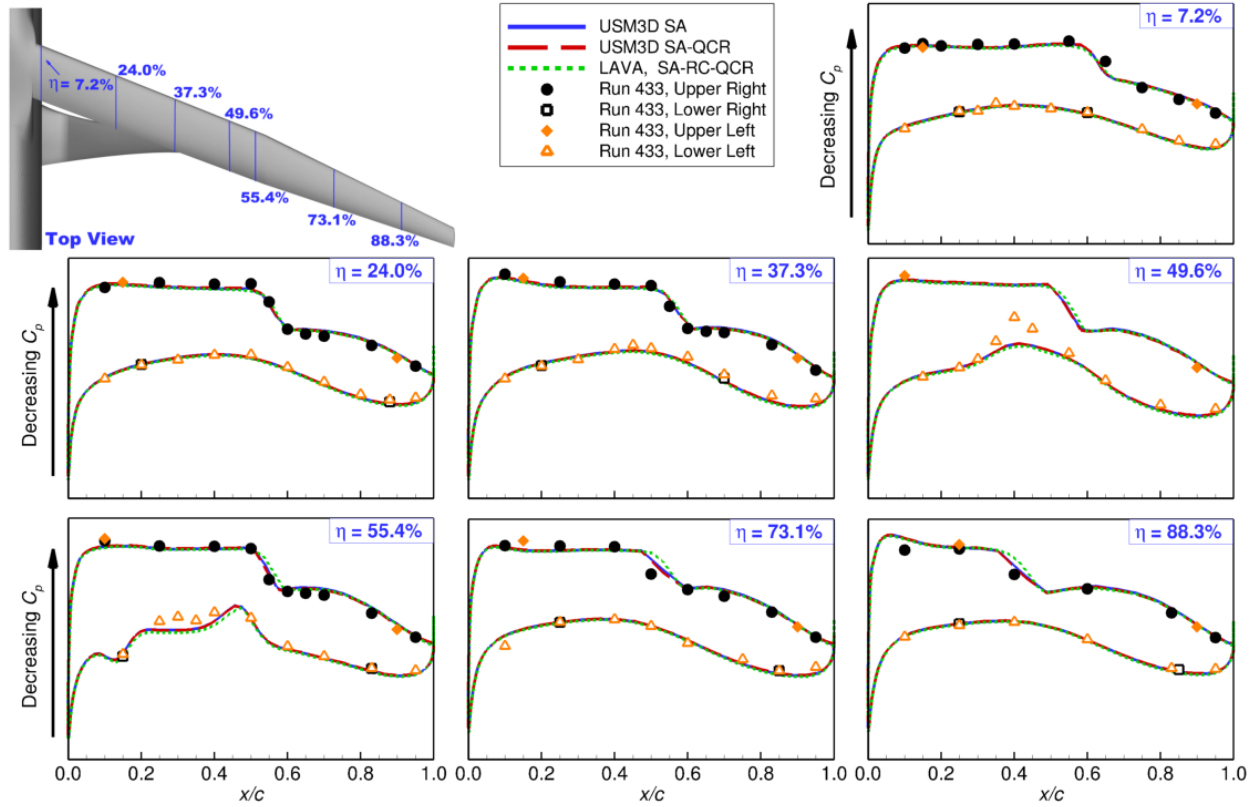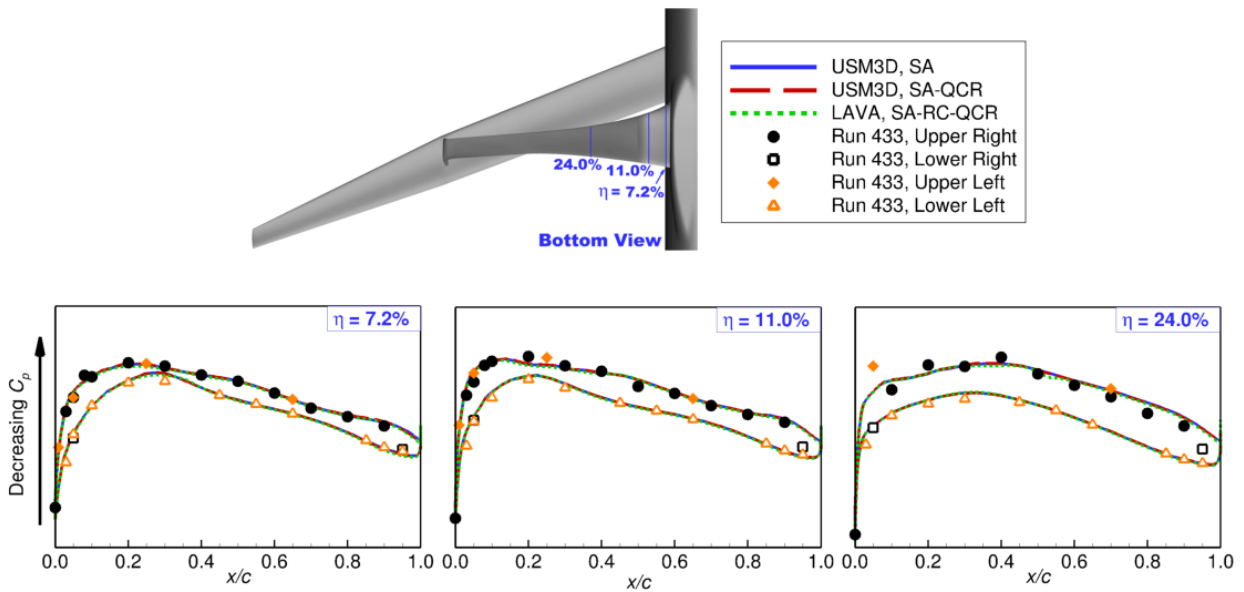
(a) $C_P$ cuts on wing.



(b) $C_P$ cuts on strut.

**Figure 21. Comparison of spanwise $C_P$ cuts for CFD and wind-tunnel data for the WT WBSV configuration at $M_\infty = 0.80$, $Re_c = 2.17$ x $10^6$, $C_L = 0.719$, and $\beta = 0°$ (USM3D mixed-element grid solutions).**

46
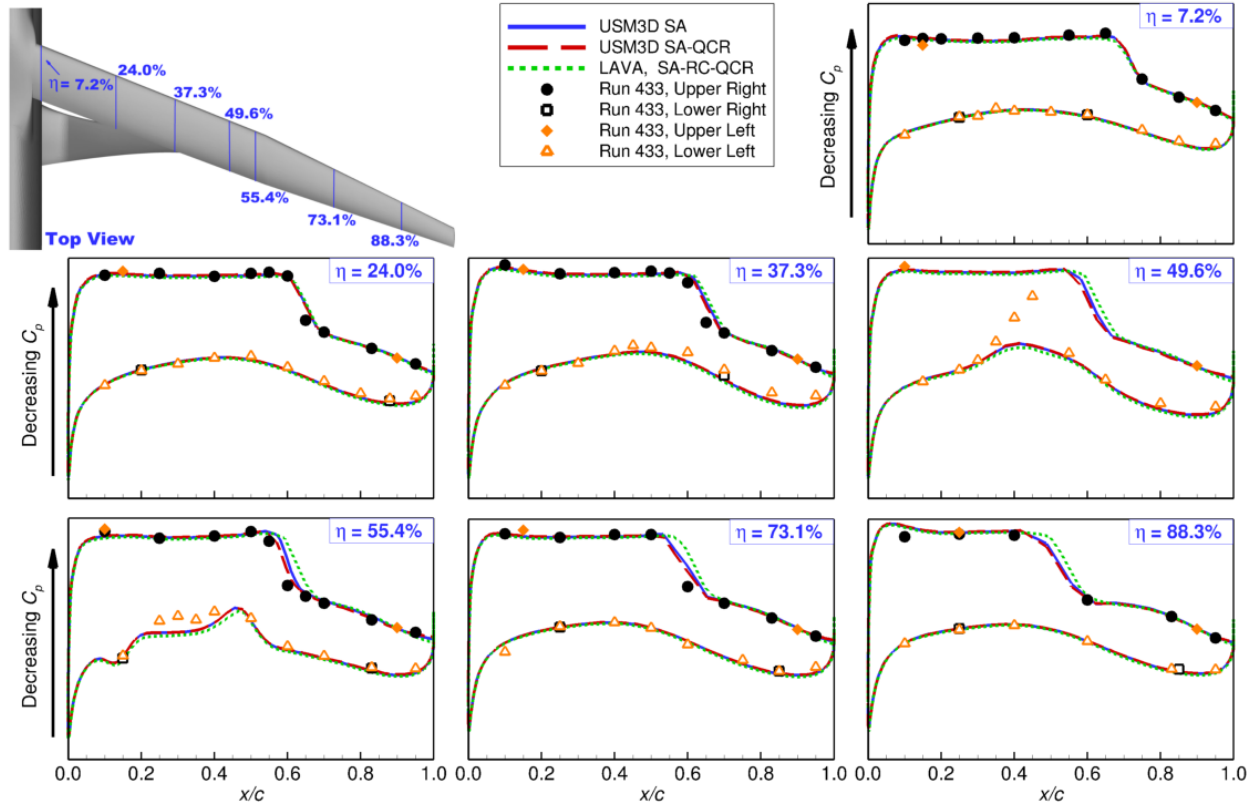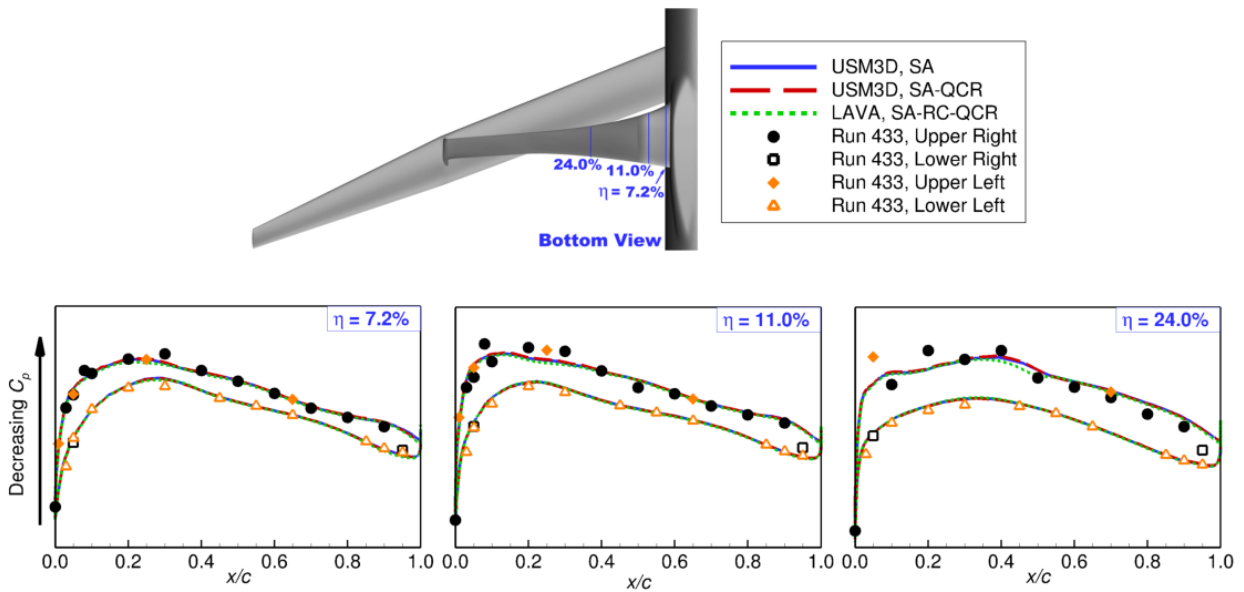
(a) $C_P$ cuts on wing.



(b) $C_P$ cuts on strut.

**Figure 22. Comparison of spanwise $C_P$ cuts for CFD and wind-tunnel data for the WT WBSV configuration at $M_\infty = 0.80$, $Re_c = 2.17 \times 10^6$, $C_L = 0.849$, and $\beta = 0°$ (USM3D mixed-element grid solutions).**
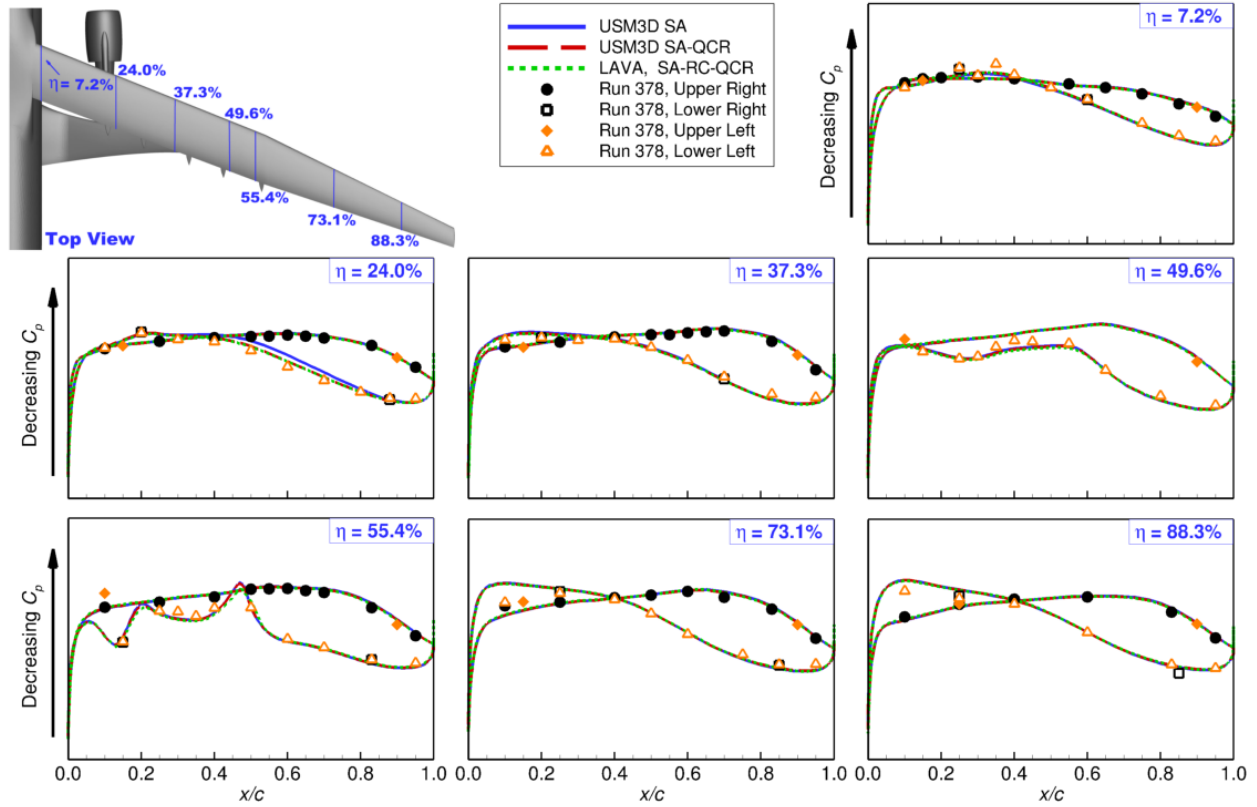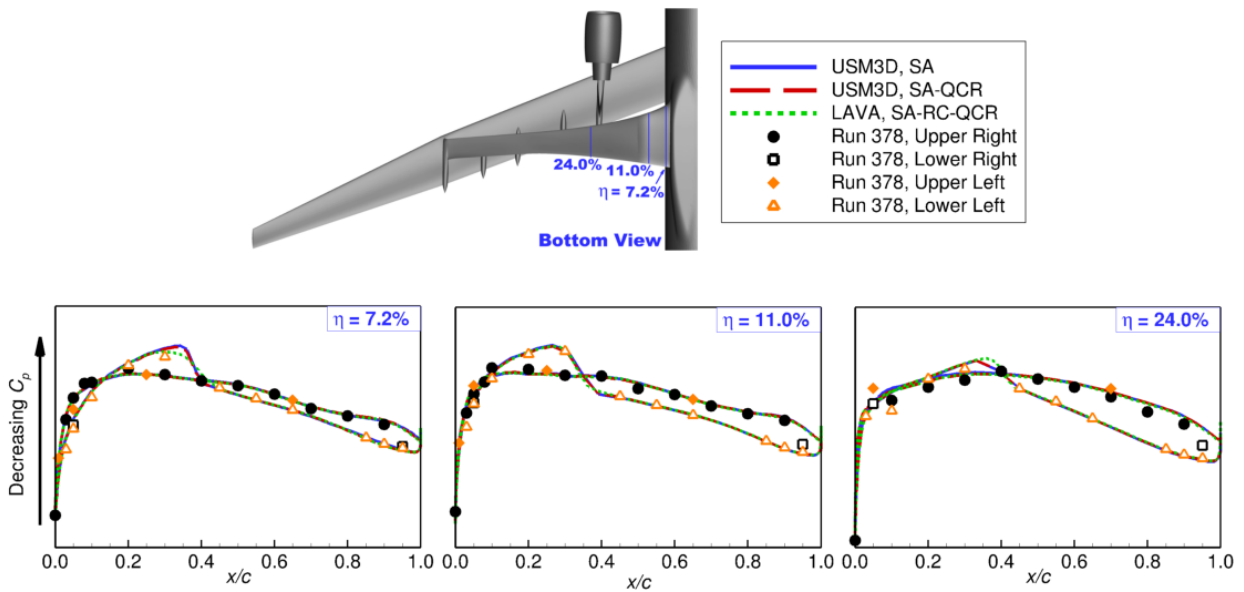
(a)  $C_P$ cuts on wing.



(b)  $C_P$ cuts on strut.

**Figure 23.  Comparison of spanwise $C_P$ cuts for CFD and wind-tunnel data for the WT WBSNFV configuration at $M_\infty = 0.80$, $Re_c = 2.17 \times 10^6$, $C_L = 0.168$, and $\beta = 0°$ (USM3D mixed-element grid solutions).**
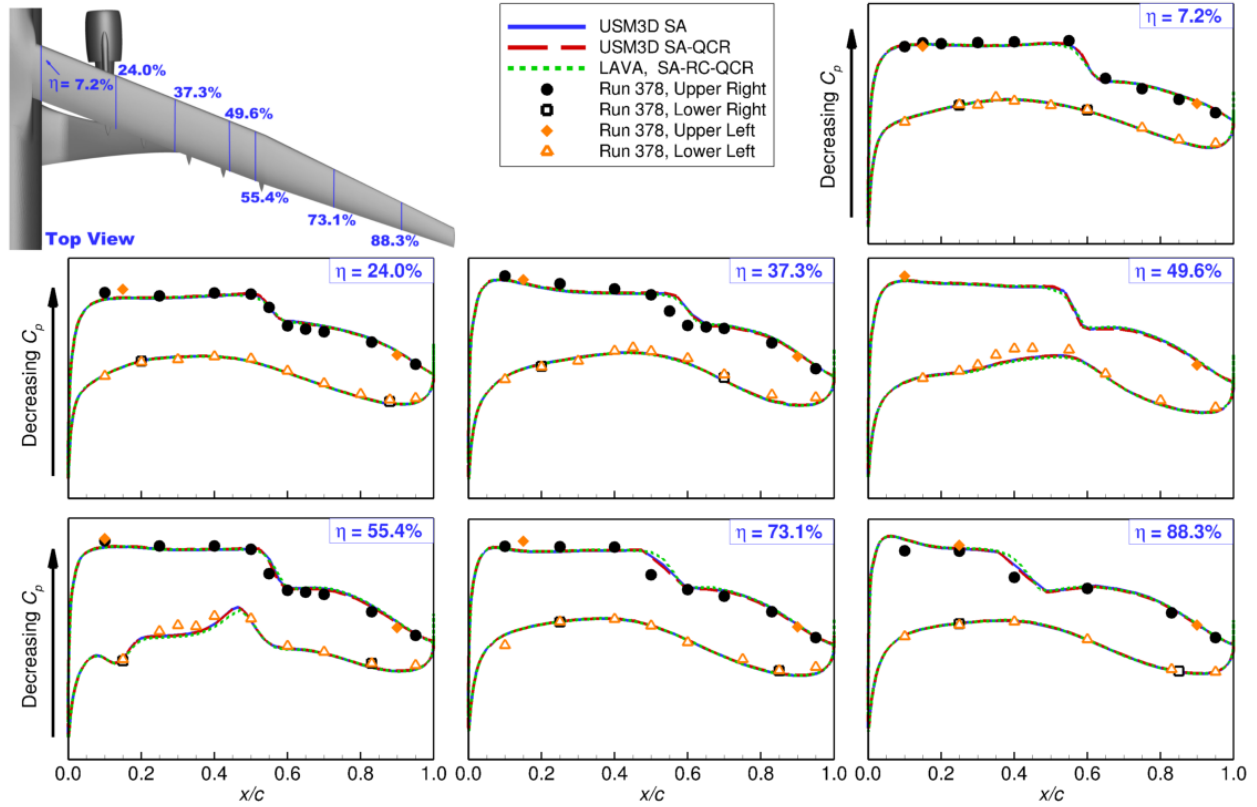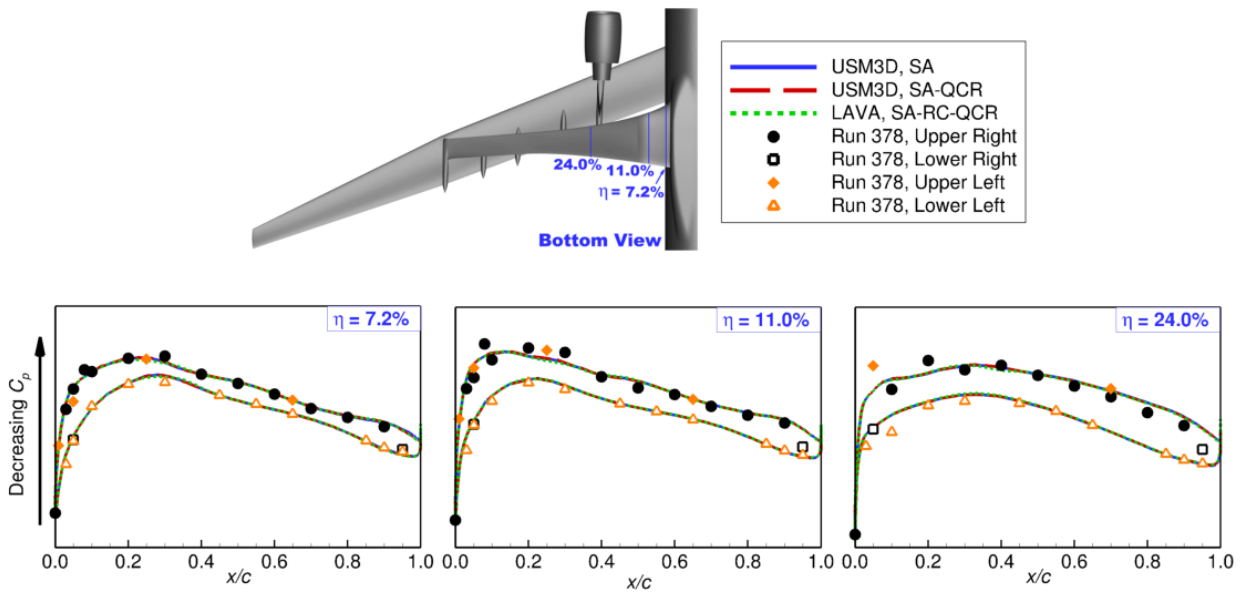
(a)  $C_P$ cuts on wing.



(b)  $C_P$ cuts on strut.

**Figure 24.  Comparison of spanwise $C_P$ cuts for CFD and wind-tunnel data for the WT WBSNFV configuration at $M_\infty = 0.80$, $Re_c = 2.17$ x $10^6$, $C_L = 0.707$, and $\beta = 0°$ (USM3D mixed-element grid solutions).**
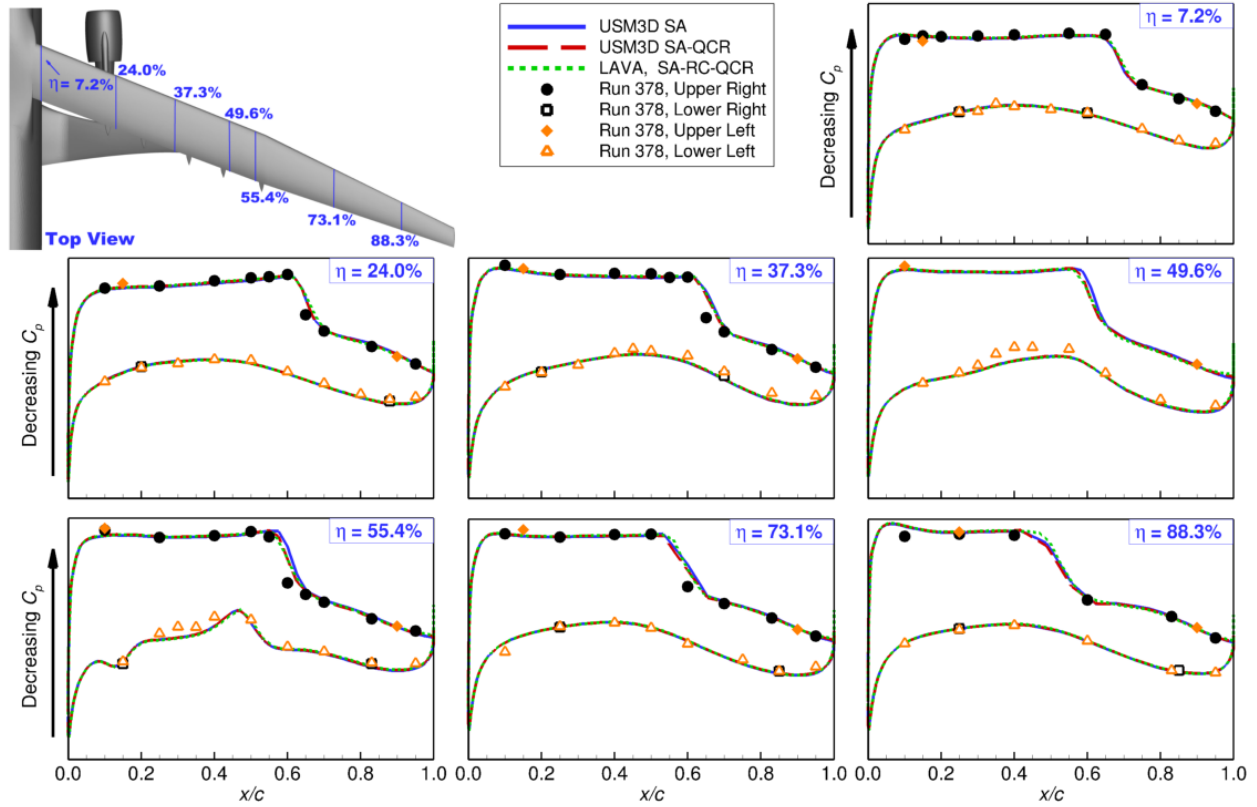
(a)  $C_P$ cuts on wing.
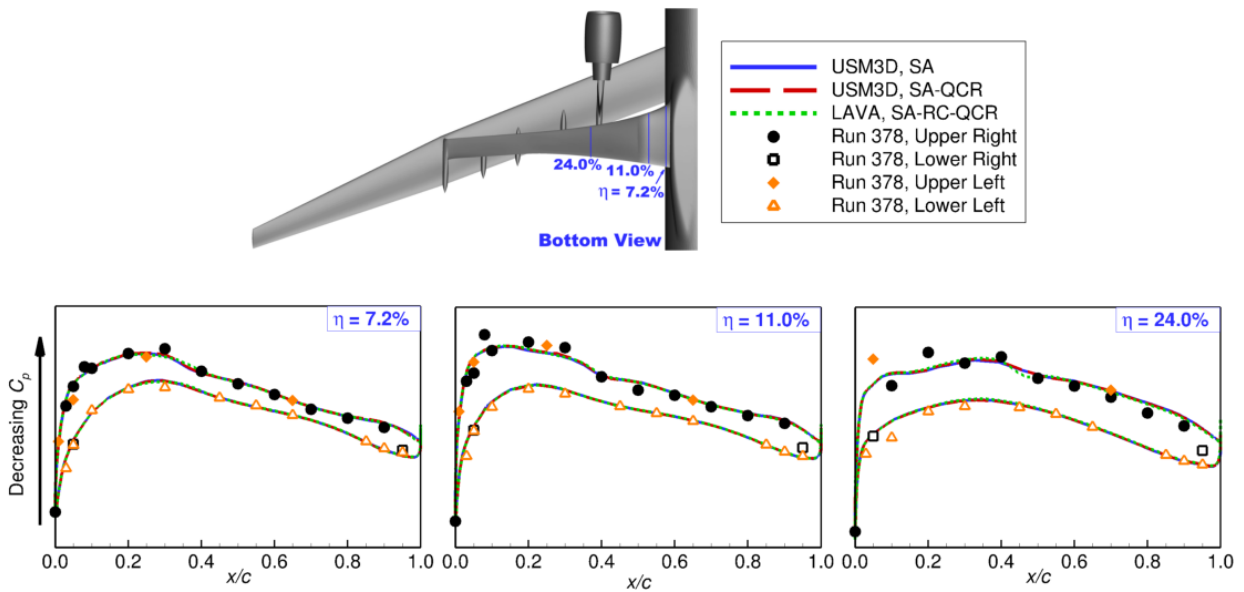


(b)  $C_P$ cuts on strut.

**Figure 25.  Comparison of spanwise $C_P$ cuts for CFD and wind-tunnel data for the WT WBSNFV configuration at $M_\infty = 0.80$, $Re_c = 2.17 \times 10^6$, $C_L = 0.848$, and $\beta = 0°$ (USM3D mixed-element grid solutions).**
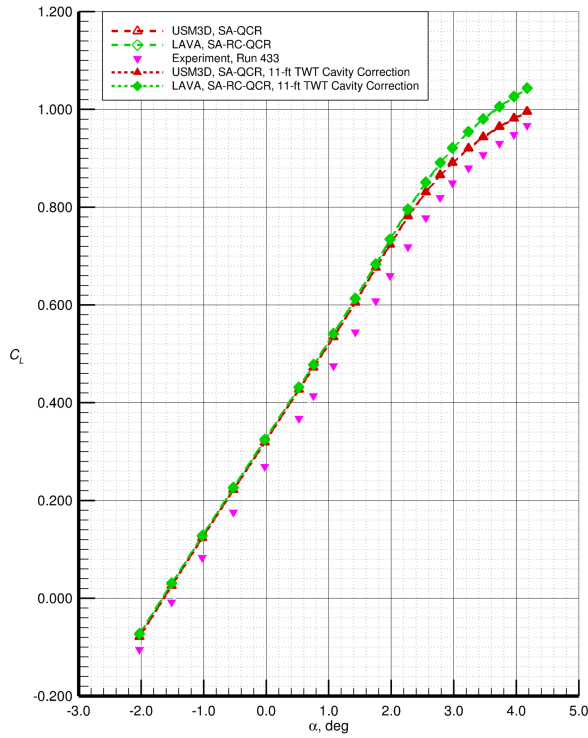
Cavity

Y = 0"
Symmetry
Plane Cut of CFD
Model and Sting
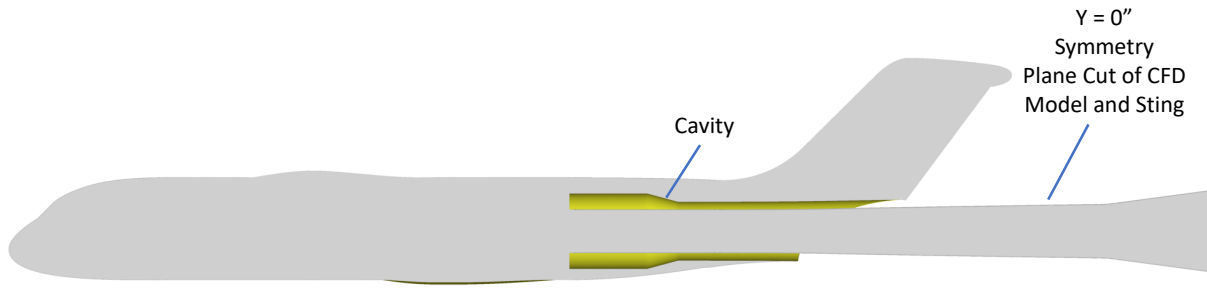
**Figure 26.  Symmetry plane cut through CFD TTBW wind tunnel model and sting with cavity region.**
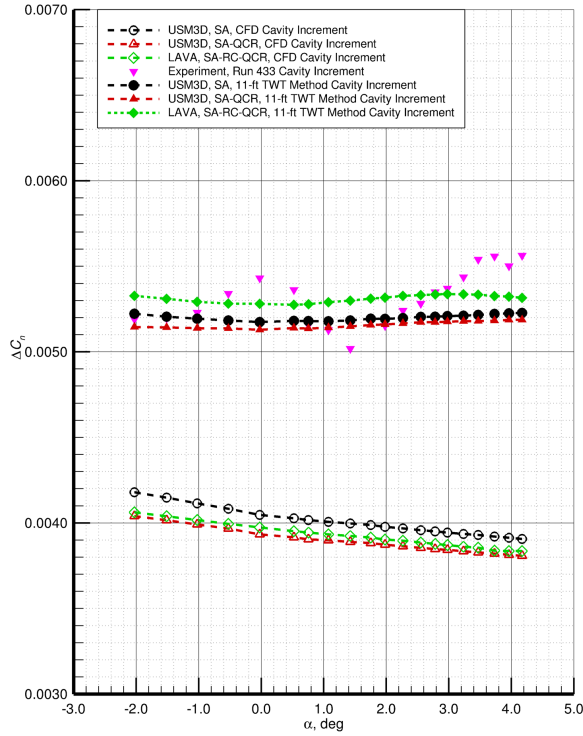
(a) $\Delta C_n$ vs $\alpha$.
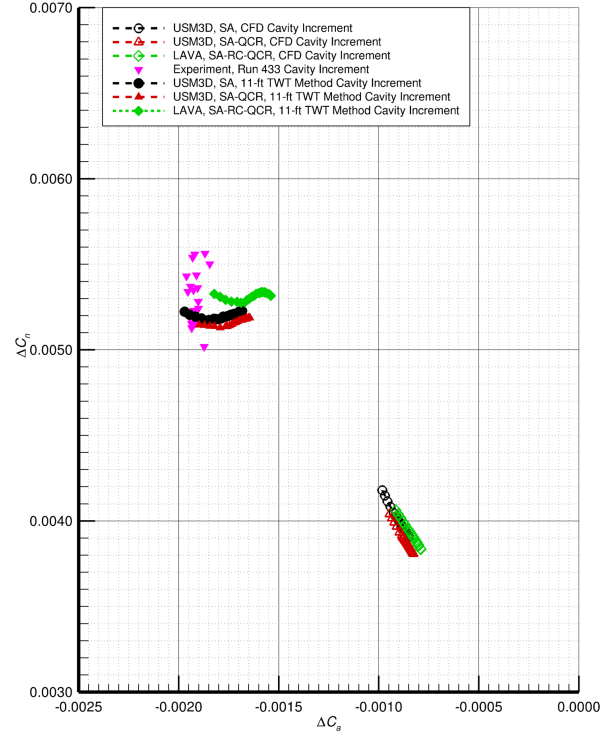
(b) $\Delta C_n$ vs $\Delta C_a$.
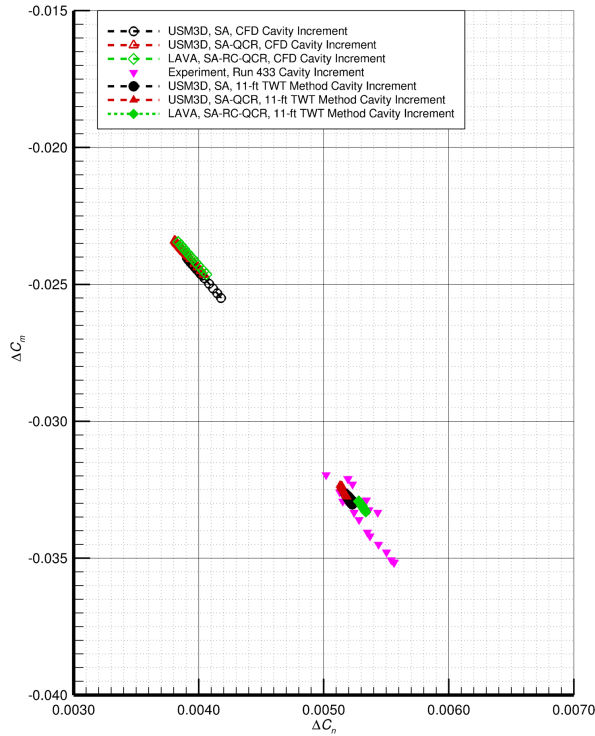
(c) $\Delta C_m$ vs $\Delta C_n$.

**Figure 27.  Comparison of CFD flow solver cavity increments, wind-tunnel data cavity increments, and CFD cavity increments calculated by implementing 11-Ft TWT method for the WT WBSV configuration at $M_\infty$ = 0.80, $Re_c$ = 2.17 x 10$^6$, and $\beta$ = 0° (USM3D mixed-element grid solutions).**
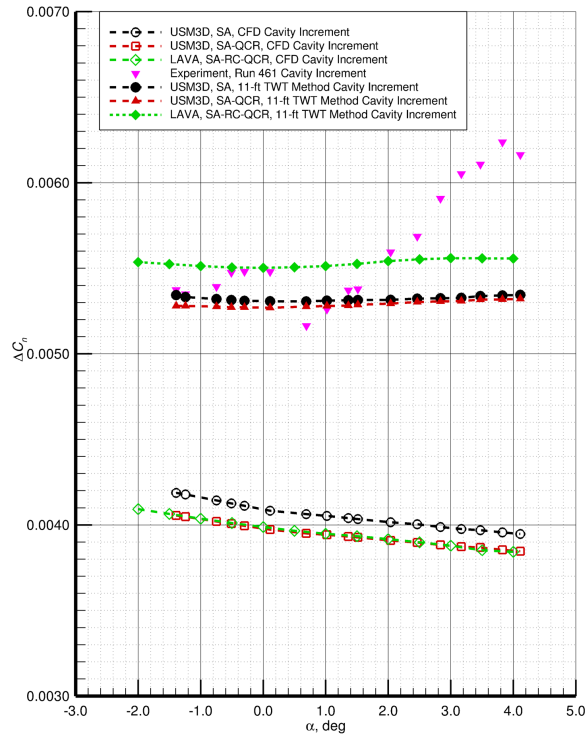
(a) $\Delta C_n$ vs $\alpha$.
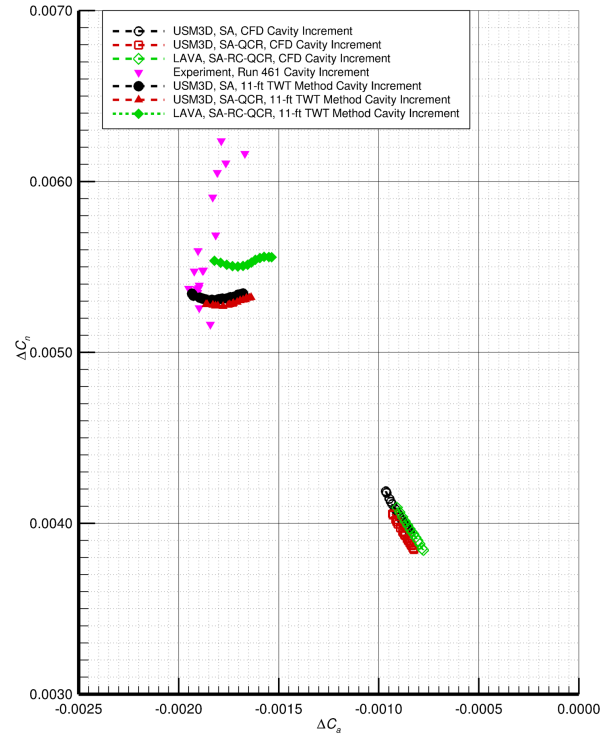
(b) $\Delta C_n$ vs $\Delta C_a$.
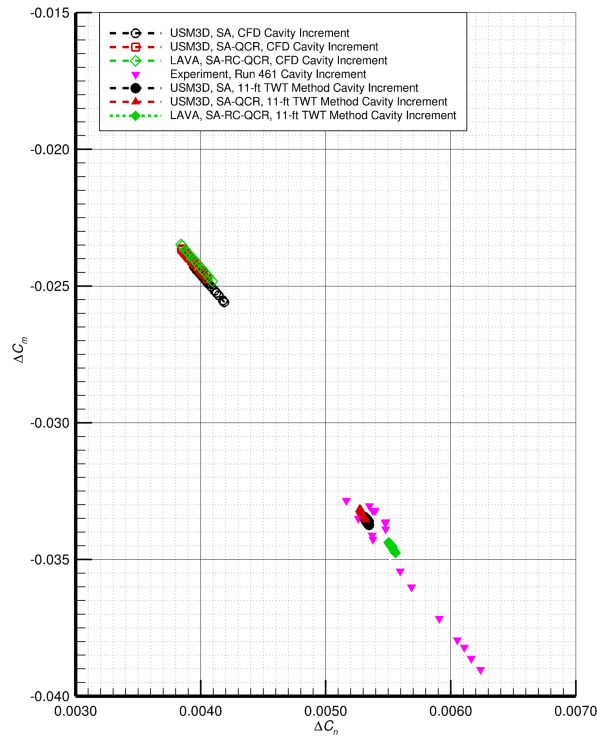
(c) $\Delta C_m$ vs $\Delta C_n$.

**Figure 28.  Comparison of CFD flow solver cavity increments, wind-tunnel data cavity increments, and CFD cavity increments calculated by implementing 11-Ft TWT method for the WT WBSV configuration at $M_\infty$ = 0.80, $Re_c$ = 3.31 x $10^6$, and $\beta$ = $0°$ (USM3D mixed-element grid solutions).**
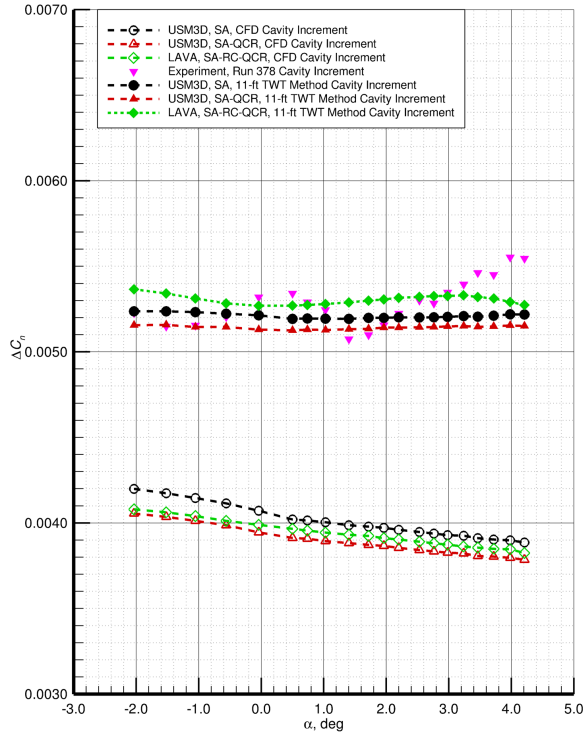
(a) $\Delta C_n$ vs $\alpha$.
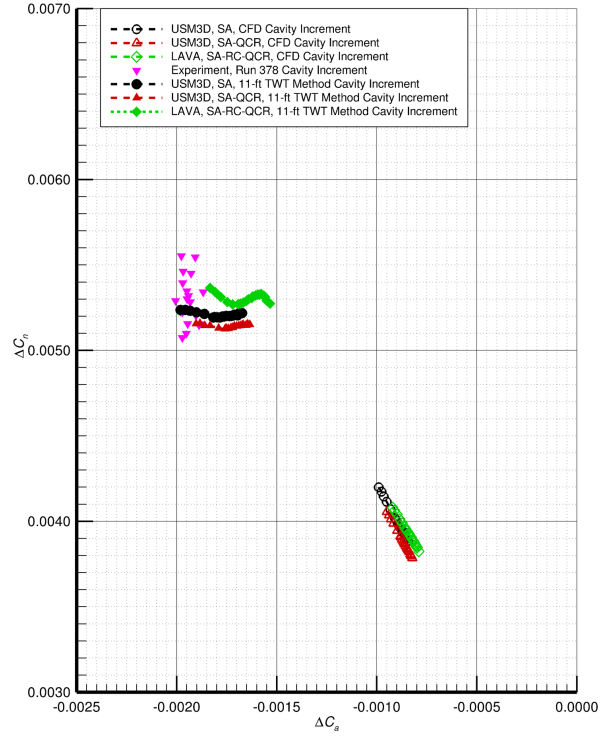
(b) $\Delta C_n$ vs $\Delta C_a$.
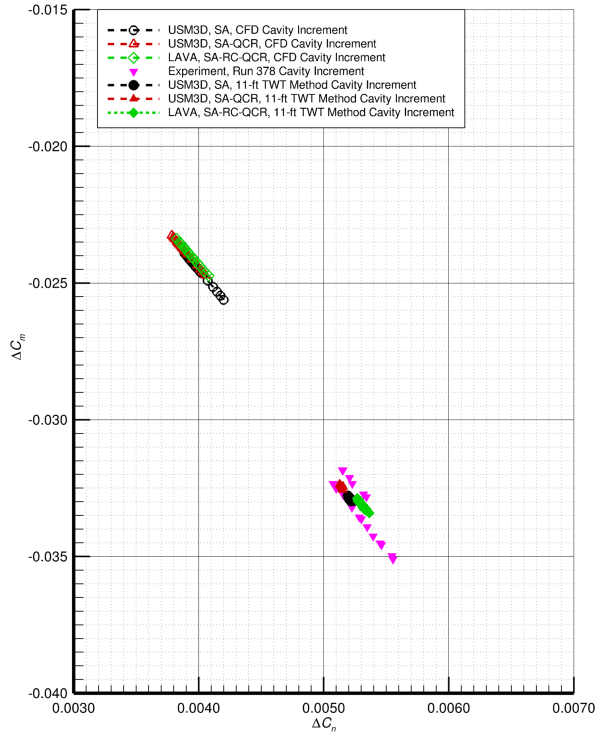
(c) $\Delta C_m$ vs $\Delta C_n$.

**Figure 29.  Comparison of CFD flow solver cavity increments, wind-tunnel data cavity increments, and CFD cavity increments calculated by implementing 11-Ft TWT method for the WT WBSNFV configuration at $M_\infty$ = 0.80, $Re_c$ = 2.17 x 10$^6$, and $\beta$ = 0° (USM3D mixed-element grid solutions).**
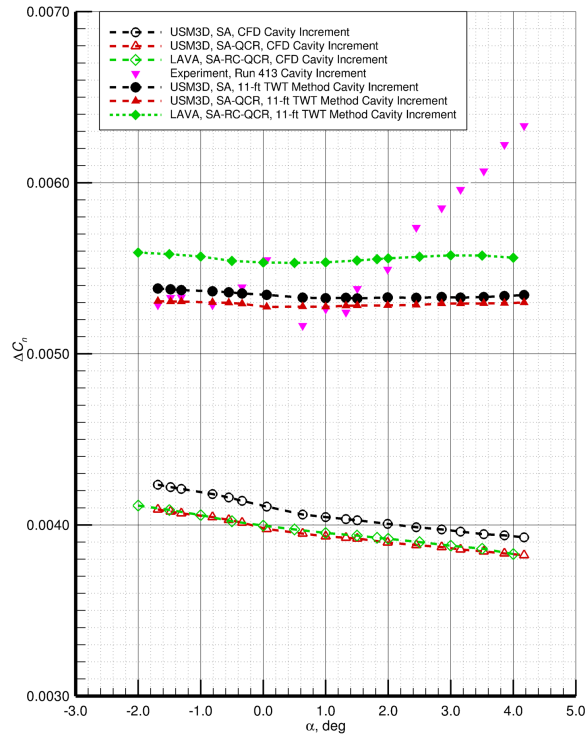
(a) $\Delta C_n$ vs $\alpha$.
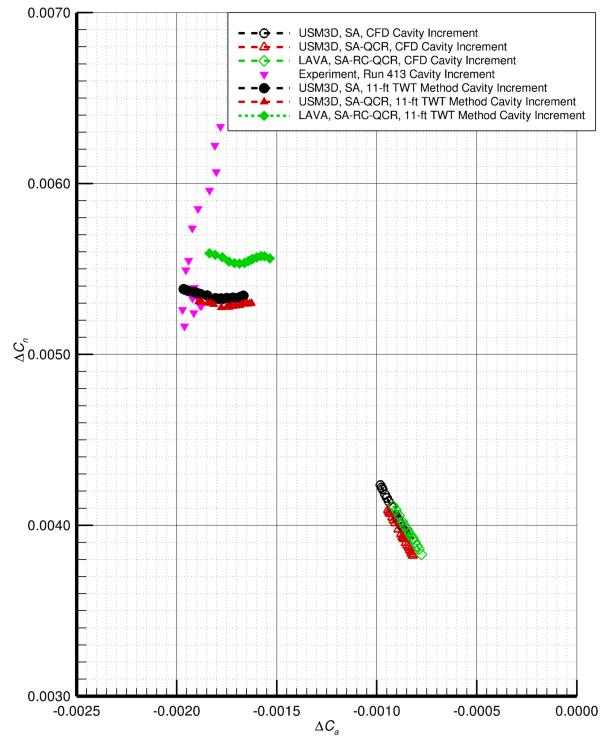
(b) $\Delta C_n$ vs $\Delta C_a$.
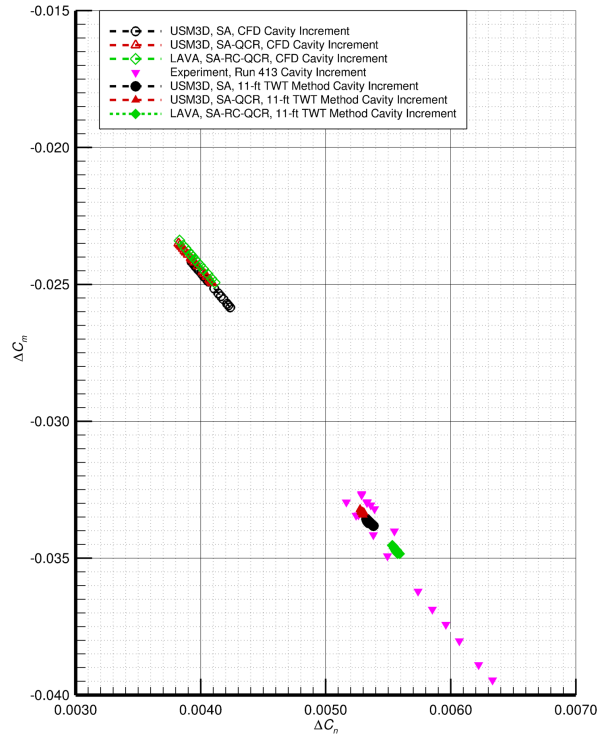
(c) $\Delta C_m$ vs $\Delta C_n$.

**Figure 30. Comparison of CFD flow solver cavity increments, wind-tunnel data cavity increments, and CFD cavity increments calculated by implementing 11-Ft TWT method for the WT WBSNFV configuration at $M_\infty$ = 0.80, $Re_c$ = 3.31 x 10$^6$, and $\beta$ = 0° (USM3D mixed-element grid solutions).**

(a) $C_L$ vs $\alpha$.
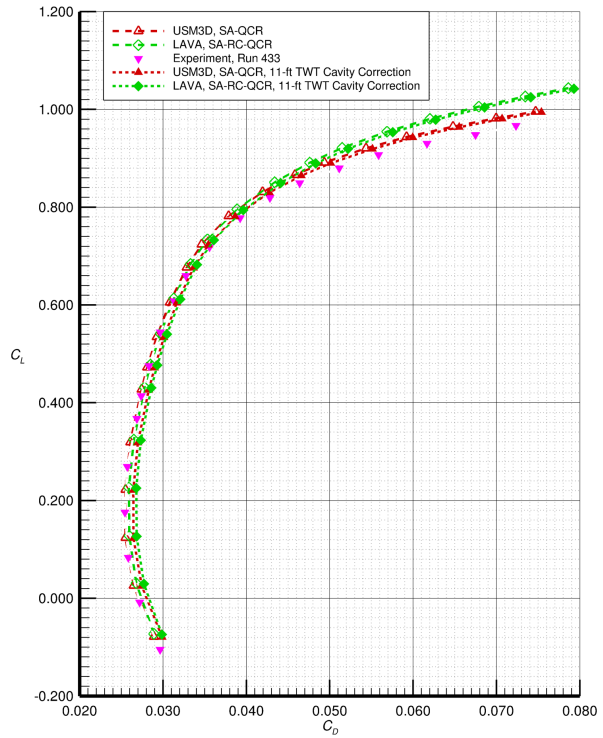
(b) $C_L$ vs $C_D$.
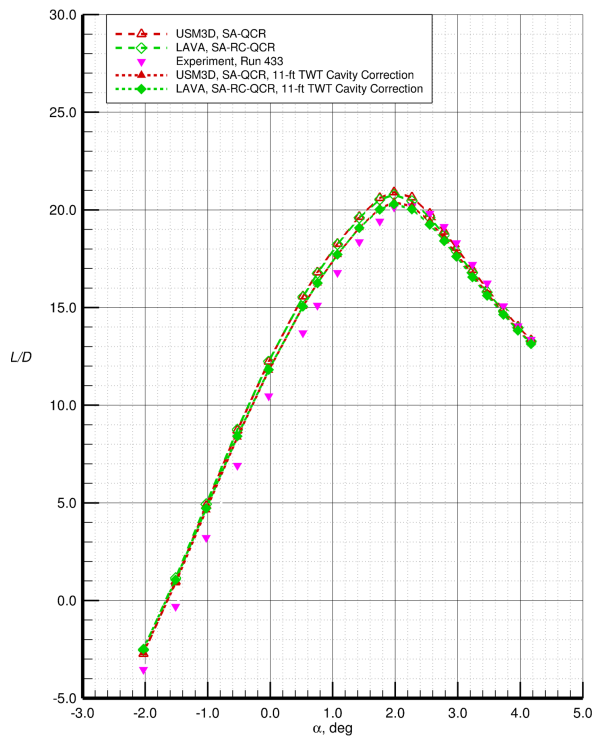
(c) $L/D$ vs $\alpha$.
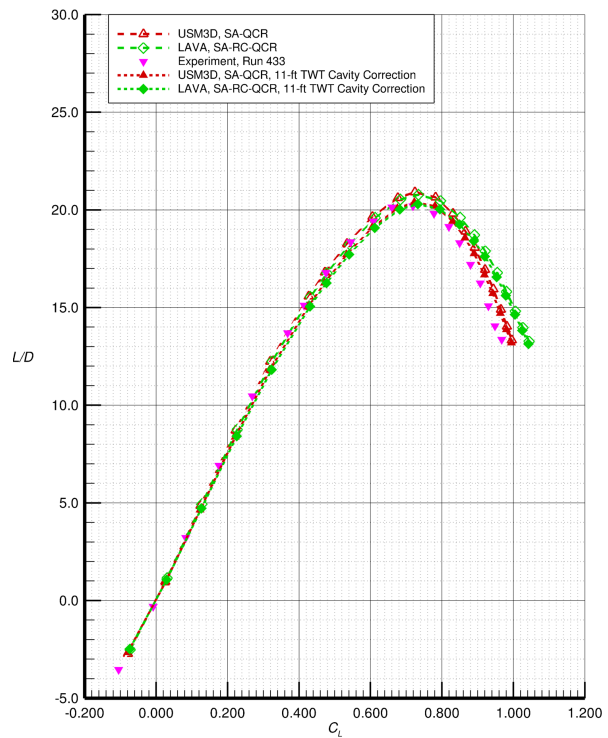
(d) $L/D$ vs $C_L$.

**Figure 31.  Comparison of CFD and wind-tunnel data for the WT WBSV configuration at $M_\infty$ = 0.80, $Re_c$ = 2.17 x $10^6$, and $\beta$ = 0° (USM3D mixed-element grid solutions).  CFD open symbols, no internal cavity surfaces in integration; CFD solid symbols, include internal cavity surfaces with 11-Ft TWT cavity correction method applied.**
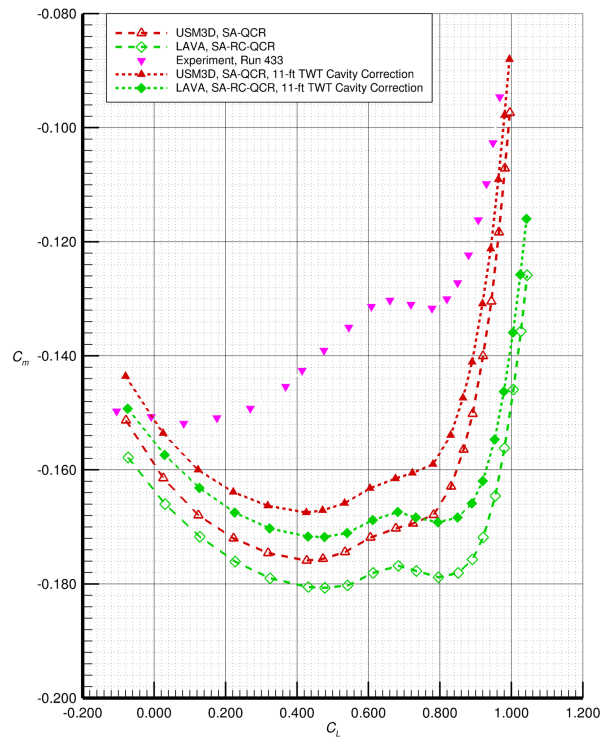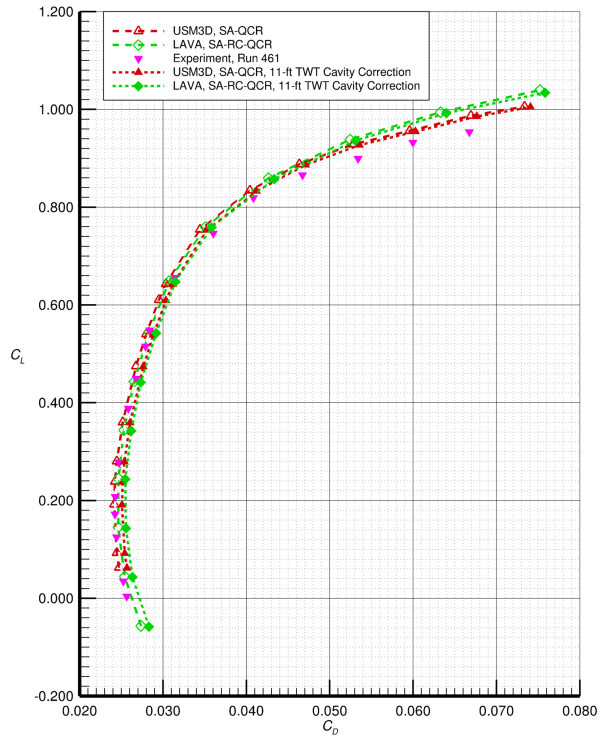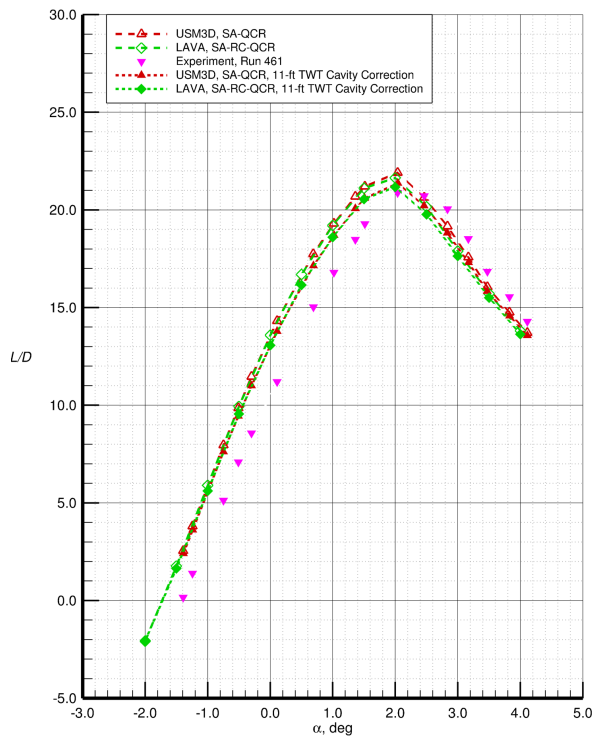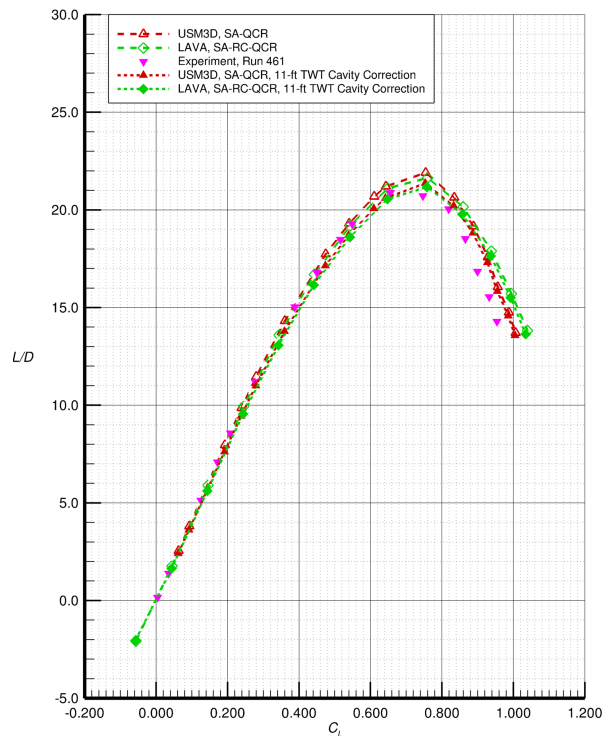
(e) $C_m$ vs $C_L$.

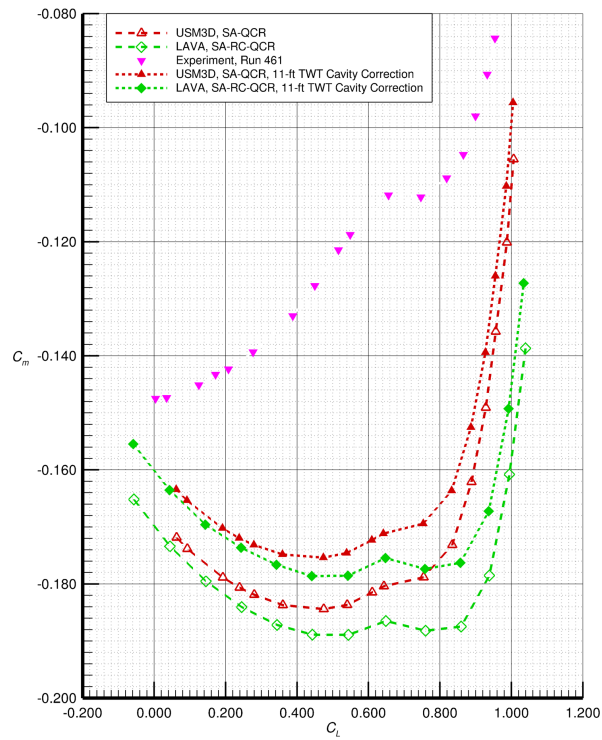**Figure 31 continued.  Comparison of CFD and wind-tunnel data for the WT WBSV configuration at $M_\infty = 0.80$, $Re_c = 2.17 \times 10^6$, and $\beta = 0°$ (USM3D mixed-element grid solutions).  CFD open symbols, no internal cavity surfaces in integration; CFD solid symbols, include internal cavity surfaces with 11-Ft TWT cavity correction method applied.**
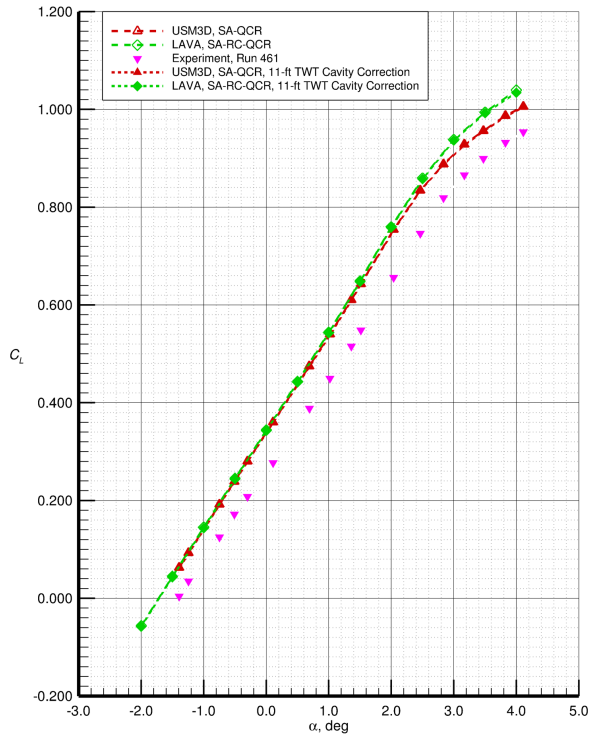
(a) $C_L$ vs $\alpha$.

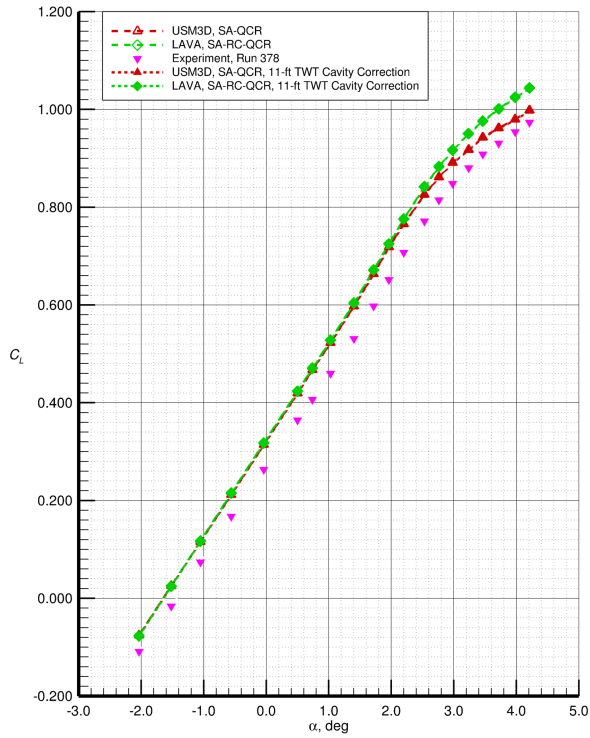(b) $C_L$ vs $C_D$.

(c) $L/D$ vs $\alpha$.

(d) $L/D$ vs $C_L$.

**Figure 32. Comparison of CFD and wind-tunnel data for the WT WBSV configuration at $M_\infty = 0.80$, $Re_c = 3.31$ x $10^6$, and $\beta = 0°$ (USM3D mixed-element grid solutions). CFD open symbols, no internal cavity surfaces in integration; CFD solid symbols, include internal cavity surfaces with 11-Ft TWT cavity correction method applied.**
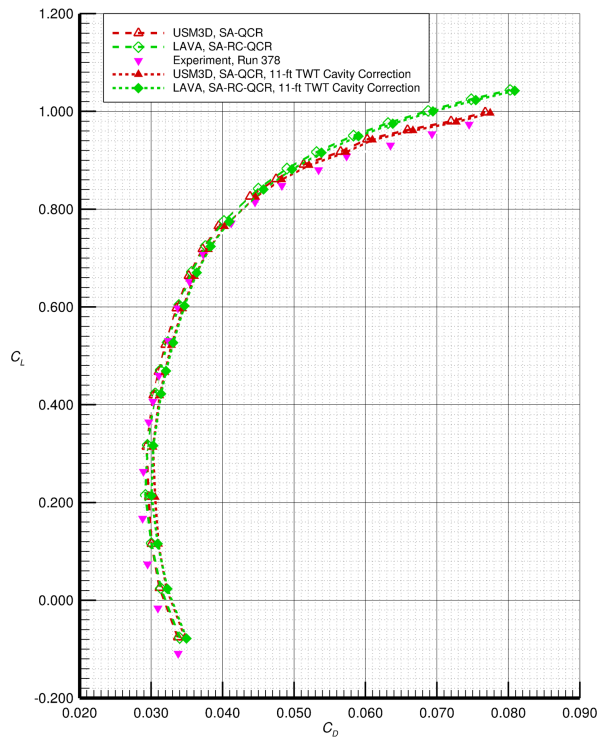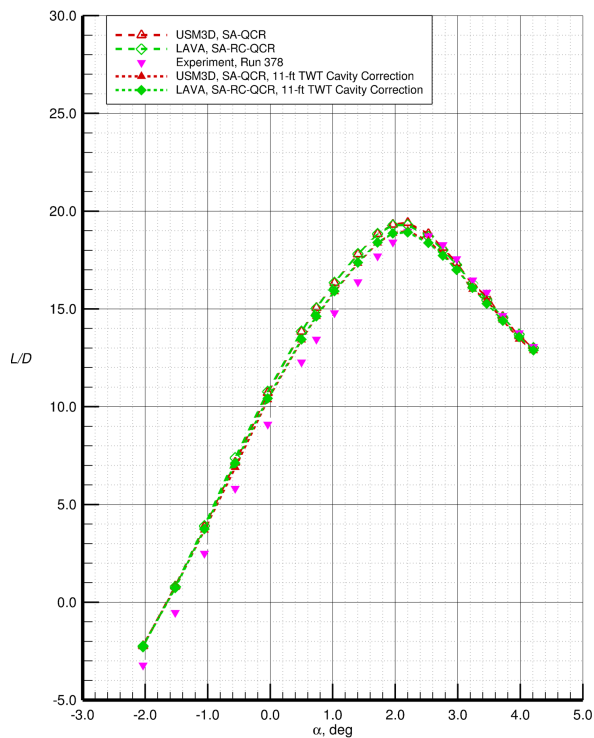
(e) $C_m$ vs $C_L$.

**Figure 32 continued.  Comparison of CFD and wind-tunnel data for the WT WBSV configuration at $M_\infty = 0.80$, $Re_c = 3.31 \times 10^6$, and $\beta = 0°$ (USM3D mixed-element grid solutions).  CFD open symbols, no internal cavity surfaces in integration; CFD solid symbols, include internal cavity surfaces with 11-Ft TWT cavity correction method applied.**
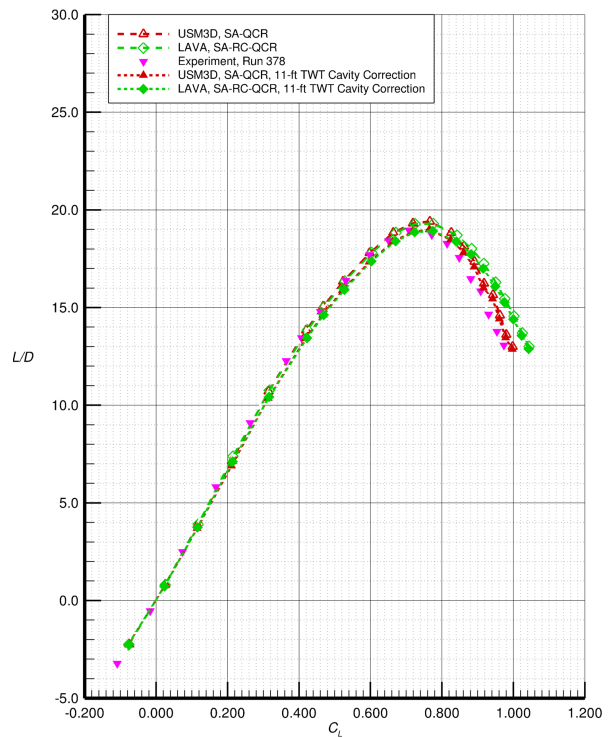
(a) $C_L$ vs $\alpha$.

(b) $C_L$ vs $C_D$.

(c) $L/D$ vs $\alpha$.

(d) $L/D$ vs $C_L$.

**Figure 33.  Comparison of CFD and wind-tunnel data for the WT WBSNFV configuration at $M_\infty = 0.80$, $Re_c = 2.17 \times 10^6$, and $\beta = 0°$ (USM3D mixed-element grid solutions).  CFD open symbols, no internal cavity surfaces in integration; CFD solid symbols, include internal cavity surfaces with 11-Ft TWT cavity correction method applied.**
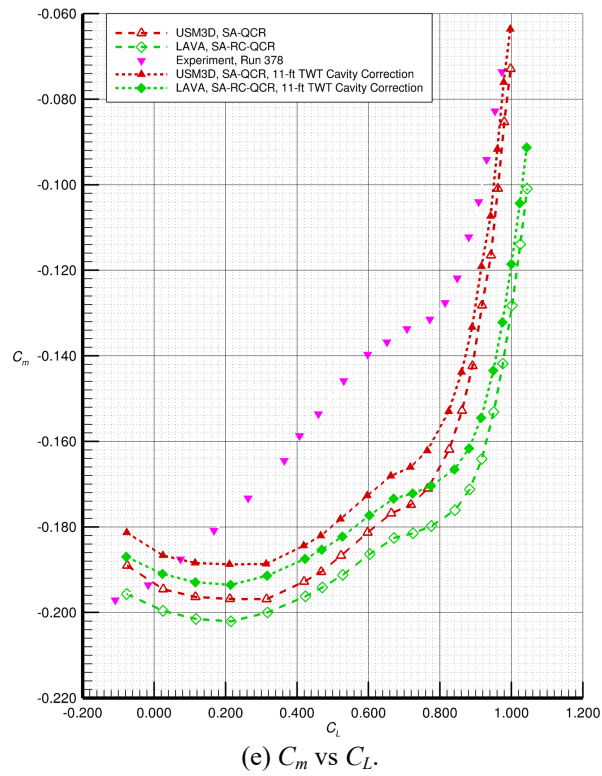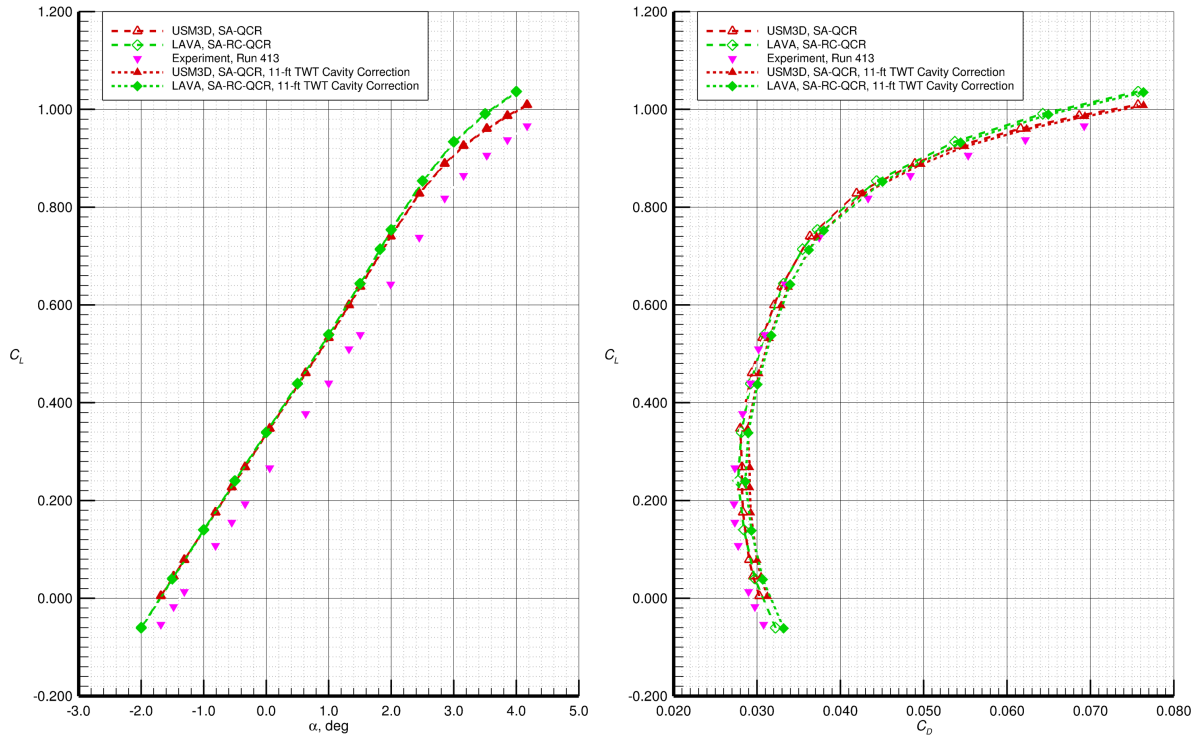
(e) $C_m$ vs $C_L$.

**Figure 33 continued. Comparison of CFD and wind-tunnel data for the WT WBSNFV configuration at $M_\infty =$ 0.80, $Re_c$ = 2.17 x 10$^6$, and $\beta$ = 0° (USM3D mixed-element grid solutions). CFD open symbols, no internal cavity surfaces in integration; CFD solid symbols, include internal cavity surfaces with 11-Ft TWT cavity correction method applied.**
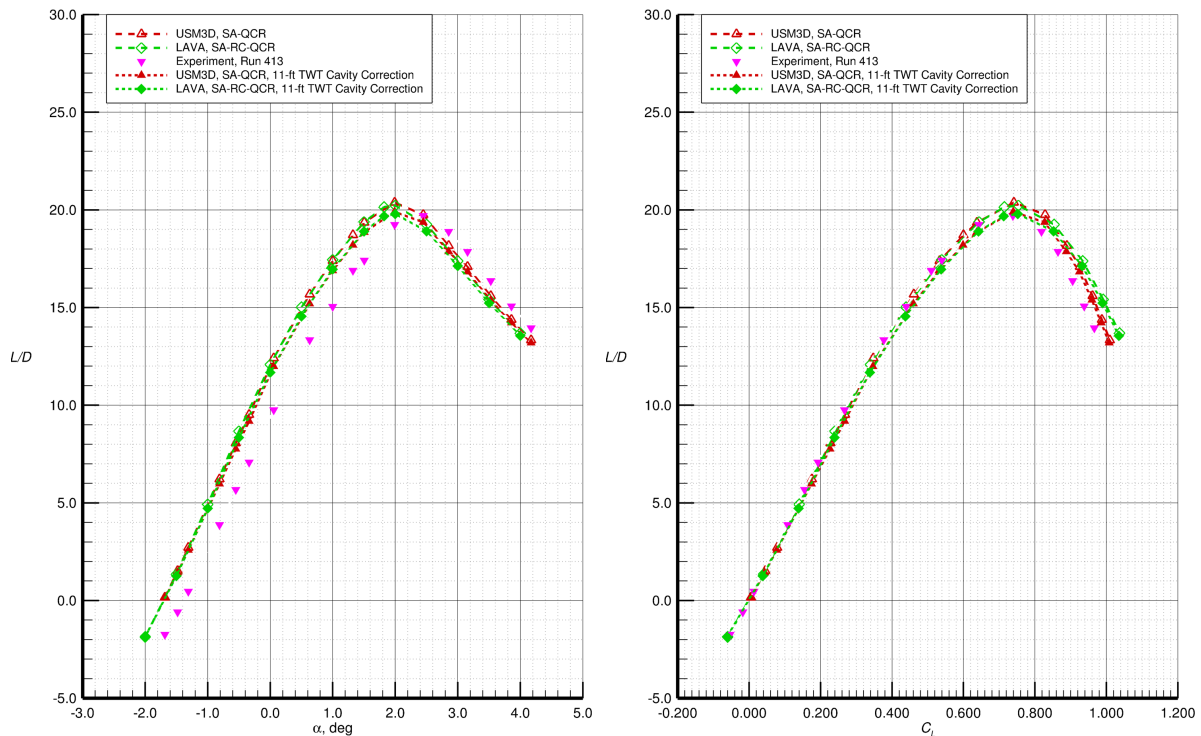
(a) $C_L$ vs $\alpha$.

(b) $C_L$ vs $C_D$.

(c) $L/D$ vs $\alpha$.

(d) $L/D$ vs $C_L$.

**Figure 34. Comparison of CFD and wind-tunnel data for the WT WBSNFV configuration at $M_\infty = 0.80$, $Re_c = 3.31 \times 10^6$, and $\beta = 0°$ (USM3D mixed-element grid solutions). CFD open symbols, no internal cavity surfaces in integration; CFD solid symbols, include internal cavity surfaces with 11-Ft TWT cavity correction method applied.**
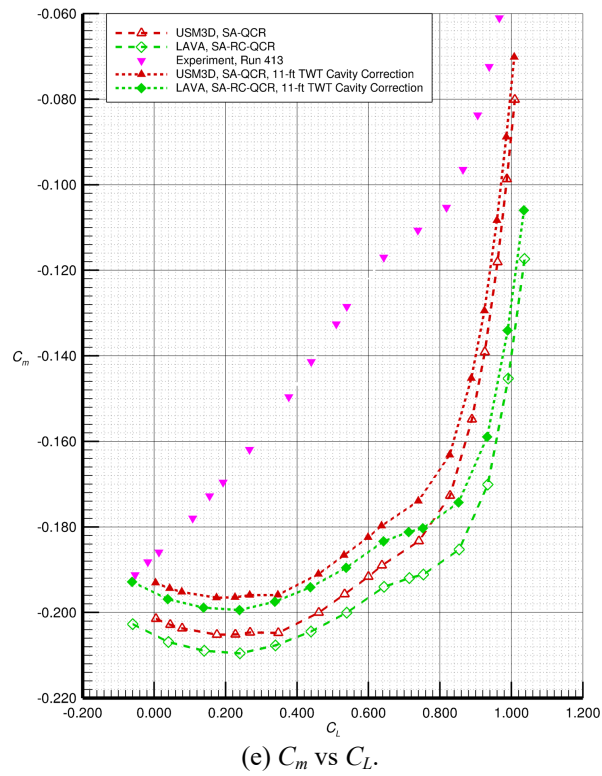
(e) $C_m$ vs $C_L$.

**Figure 34 continued.  Comparison of CFD and wind-tunnel data for the WT WBSNFV configuration at $M_\infty$ = 0.80, $Re_c$ = 3.31 x 10$^6$, and $\beta$ = 0° (USM3D mixed-element grid solutions).  CFD open symbols, no internal cavity surfaces in integration; CFD solid symbols, include internal cavity surfaces with 11-Ft TWT cavity correction method applied.**